CHARACTERIZATION AND DIAGNOSTIC METHODS FOR GEOMAGNETIC AURORAL INFRASOUND WAVES

By

Justin J Oldham

RECOMMENDED: Charles R. Wilson

John Olson

Dr. Curt A. L. Szuberla
Advisory Committee Chair

Dr. Renate Wackerbauer, Chair
Department of Physics

APPROVED:

Dr. Paul Layer, Dean
College of Natural Science and Mathematics

John C Eichelberger

Dr. John C. Eichelberger
Dean of the Graduate School

7 December 2015

Date

CHARACTERIZATION AND DIAGNOSTIC METHODS FOR GEOMAGNETIC AURORAL INFRASOUND WAVES

A
DISSERTATION

Presented to the Faculty
of the University of Alaska Fairbanks

in Partial Fulfillment of the Requirements
for the Degree of

DOCTOR OF PHILOSOPHY

By

Justin J Oldham, B.S.

Fairbanks, AK

December 2015

Abstract

Infrasonic perturbations resulting from auroral activity have been observed since the 1950's. In the last decade advances in infrasonic microphone sensitivity, high latitude sensor coverage, time series analysis methods and computational efficiency have elucidated new types of auroral infrasound. Persistent periods of infrasonic activity associated with geomagnetic sub-storms have been termed geomagnetic auroral infrasound waves [GAIW]. We consider 63 GAIW events recorded by the Fairbanks, AK infrasonic array I53US ranging from 2003 to 2014 and encompassing a complete solar cycle. We make observations of the acoustic features of these events alongside magnetometer, riometer, and all-sky camera data in an effort to quantify the ionospheric conditions suitable for infrasound generation. We find that, on average, the generation mechanism for GAIW is confined to a region centered about ~60^0 longitude east of the anti-Sun-Earth line and at ~77^0 North latitude. We note furthermore that in all cases considered wherein imaging riometer data are available, that dynamic regions of heightened ionospheric conductivity periodically cross the overhead zenith. Consistent features in concurrent magnetometer conditions are also noted, with irregular oscillations in the horizontal component of the field ubiquitous in all cases. In an effort to produce ionosphere based infrasound free from the clutter and unknowns typical of geophysical observations, an experiment was undertaken at the High Frequency Active Auroral Research Program [HAARP] facility in 2012. Infrasonic signals appearing to originate from a source region overhead were observed briefly on 9 August 2012. The signals were observed during a period when an electrojet current was presumed to have passed overhead and while the facilities radio transmitter was periodically heating the lower ionosphere. Our results suggest dynamic auroral electrojet currents as primary sources of much of the observed infrasound, with modulation of the electrojets due to energetic particle precipitation, dispersion due to coupling with gravity waves, and reflection and refraction effects in the intervening atmosphere all potential factors in the shaping of the waveforms observed.

Table of Contents

List of Figures

Acknowledgements

It is my belief that no substantive accomplishment can ever be attributed entirely and solely to one individual. In the case of this dissertation, I would like to thank each and every person who mentored me, supported me, and inspired me throughout the research and writing process, but this would be an impractical and bottomless task. Instead I here acknowledge a short list of major contributors and trust that those not mentioned will accept my gratitude in a blanket statement. I must thank my first physics instructor Matt Heavner, whose enthusiasm for physics and education inspired me to pursue further study in the field. I also send my thanks to my undergraduate adviser Renate Wackerbauer, who's clear and elegant lectures I seek to emulate. Acknowledgement is due to all of my graduate committee members: John Olson for his mentorship, Charles Wilson for his tireless research, and Hans Nielsen for his practical advice. I send my deepest thanks to my graduate adviser Curt Szuberla for his perpetual support. Finally, my sincere gratitude goes out to my family and friends who steadfastly stood by me throughout the long process of my education. Thank you.

"Taking Three as the subject to reason about-
A convenient number to state-
We add Seven, and Ten, and then multiply out
By One Thousand diminished by Eight.

The result we proceed to divide, as you see,
By Nine Hundred and Ninety and Two:
Then subtract Seventeen, and the answer must be
Exactly and perfectly true."

- Lewis Carrol

Chapter 1

Introduction

1.1 Historical Perspective and Research Motivation for Auroral Infrasound

The goal of this thesis is to address some of the many open questions regarding infrasonic waves generated by the aurora and related phenomenon. The kinds of brilliant displays of aurora borealis (or Australis) that are often associated with auroral infrasound have delighted and confounded observers for centuries. Yet remarkably even the crudest physical description of the aurora is a relatively recent twentieth century development. By and large, technical observation of Earth's low-space/high-orbit region where the aurora occurs, principally the thermosphere, has grown up alongside theoretical handling of plasma physics with the most significant advances coming from the late 20th century to present. Even now, the great many scales over which the physics must be understood, the technical challenges in obtaining experimental measurements, and the complexity of the physical theories involved ensure that aurora related physics remains an area of lively and widespread research.

The earliest publications of which I am aware regarding infrasonic radiation from auroral events date back to the early 1960s [1]. This area of research became far more widely studied and accepted following two seminal publications under primary author C.R. Wilson in the journal *Nature* [2,3]. By the end of that year Dr. Wilson and his colleagues had demonstrated many examples of what appeared to be infrasonic bow waves resulting from supersonic motions of the auroral arc. They posited that auroral electrojet currents coupled with atmospheric neutrals in the lower ionosphere through **J x B** forces and Ohmic heating to produce infrasonic radiation. These bow waves were termed Auroral Infrasound Waves [AIW], and the ensuing decade brought many spirited debates and research lines as the details of the physical mechanisms and data analysis methods regarding AIW were fleshed out by Wilson, Chimonas, Swift, and many others [4-9]. The 1970's and 80's brought expanded theoretical background to the AIW concepts. Dan Swift's modeling of AIW using one-fluid plasma approximations and coupling to the neutral atmosphere gave excellent agreement with observations, and is discussed in more detail below [4].

Beginning in the 1990's the Preparatory Commission for the Comprehensive Test Ban Treaty Organization [CTBTO] began monitoring for nuclear weapons tests as part of the Comprehensive Test Ban Treaty [CTBT]. Along with seismic, hydro-acoustic, and radionuclide stations, infrasonic microphone arrays were chosen to be part of the International Monitoring System [IMS]. These infrasound stations are designed to be part of a global network that can detect and locate atmospheric nuclear tests; some 60 stations are eventually expected to be active worldwide. The infrasound group within the Geophysical Institute at the University of Alaska Fairbanks, was selected to establish two CTBT stations. One on campus in College, AK and another at Windless Bight, Antarctica, on the Ross Ice Shelf. The stations were installed with state-of-the-art eight element infrasound sensor arrays (see Chapter 2 for details). They provided a significant increase in sensitivity and a near-continuous data set for analysis. Furthermore, leaps in computational power over the last decades increased the efficiency and resolution of data analysis methods. As a result, soon after the installation of the station at College, Alaska, in 2002, high-trace velocity signals [HTV's] were observed that did not appear to be consistent with traditional AIW models, but showed a clear association to specific geomagnetic conditions. These new infrasound signals were presumed to be geomagnetic in origin and were frequently noted to occur during the break-up period of geomagnetic substorms. Scientists in the field eventually settled on the name Geomagnetic Auroral Infrasound Waves [GAIW]; they differed clearly from previously described AIW.

Over the ensuing decade, GAIW proved to be another rich line of research, (particularly for Dr.'s C.R. Wilson and J.V. Olson, who published several papers in that time) [10,11,12]. It was observed that GAIW tend to occur during the end of the geomagnetic substorm, often during periods of pulsating aurora, and that the period of oscillations of the GAIW time series and the auroral luminosity are roughly equivalent [10]. However, whatever the physical mechanisms that generate the GAIW may be, they remain poorly understood. Research by graduate student Lee and others showed that GAIW could be systematically isolated from other HTV signals by its characteristic frequency-domain power spectral density, its unusually high trace velocity, and other factors related to wave-form coherence across a microphone array; they also demonstrated that GAIW occurred quite frequently in the absence of pulsating auroras[13,14]. Energy budget considerations proposed by Nielsen and Olson further obfuscated a causal relationship between the pulsating aurora and the GAIW, and more detailed modeling efforts made by Larqiuer et al estimated pressure perturbations on the ground an order of magnitude below the observed signals [10,12].

1.2 Dissertation Organization

The research pursued in this thesis may be summed up by two straightforward questions. *Can we quantify conditions that are necessary and/or sufficient for the generation of GAIW? From these conditions, what are the ramifications on the mechanisms of GAIW generation?* To this end, the thesis presents an effort to consolidate the considerable body of literature that has appeared regarding auroral infrasound, as well as detail research progress made by the author and colleagues during his tenure in the group. The manuscript is broken up into six chapters. The first two chapters outline the state of auroral infrasonic research at the time my contributions began; Chapter 1 provides a summary literature review and outlines the physical models used throughout the text, while Chapter 2 details the sensors and time series analysis methods adopted for the research. Chapter 3 is devoted to the physical sensors and data processing methods associated with other diagnostic equipment, including the Imaging Riometer and All Sky Cameras at Poker Flat, AK and the Geophysical Institute Magnetometer Array. Chapters 4 and 5 discuss statistical findings and experimental results respectively; Chapter 6 provides conclusions and recommendations for future work.

1.3 Earth's Atmosphere

It would be impossible to discuss GAIW at any length without running into issues of atmosphere composition, plasma dynamics in low Earth space, and various other details couched in the fields of atmospheric sciences and aeronomy. Here we present some qualitative background on the planetary scale structure of the atmosphere.

Near sea level, Earth's atmosphere is composed predominantly of nitrogen (~78% N_2), oxygen (~21% 0_2), and argon (~1% Ar), with CO_2 and other trace gasses accounting for less than half a percent of the total mass. Throughout the troposphere the relative abundance of these gasses remains roughly constant with respect to altitude due to turbulent mixing, convective transport, etc. In the mesosphere above altitudes of 70 km the atmospheric chemical composition changes abruptly, with monatomic oxygen and, to a lesser extent, helium, hydrogen, and monatomic nitrogen playing an increasingly important role. A useful model of the relative abundance of various gasses and a variety of other atmospheric parameters is NASA's MSIS-E-90 [15]. This model has been used to plot the density of the principal neutral molecules in Fig. 1.1 and the temperature profile in Fig. 1.2.

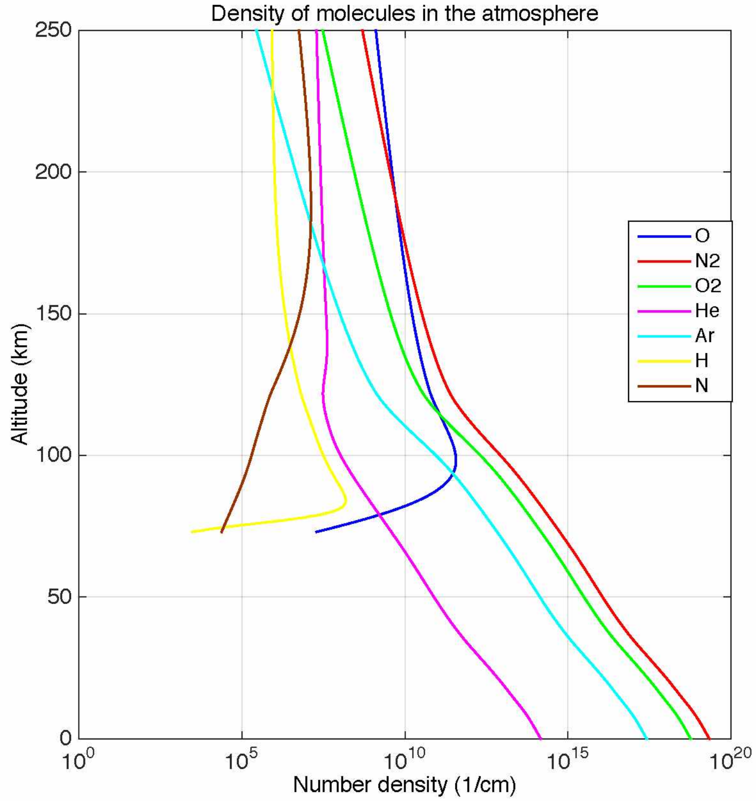

Figure 1.1 Number density (cm^-3) of principal molecules comprising Earth's atmosphere. The relative abundance of various components changes abruptly as the thermosphere is approached.

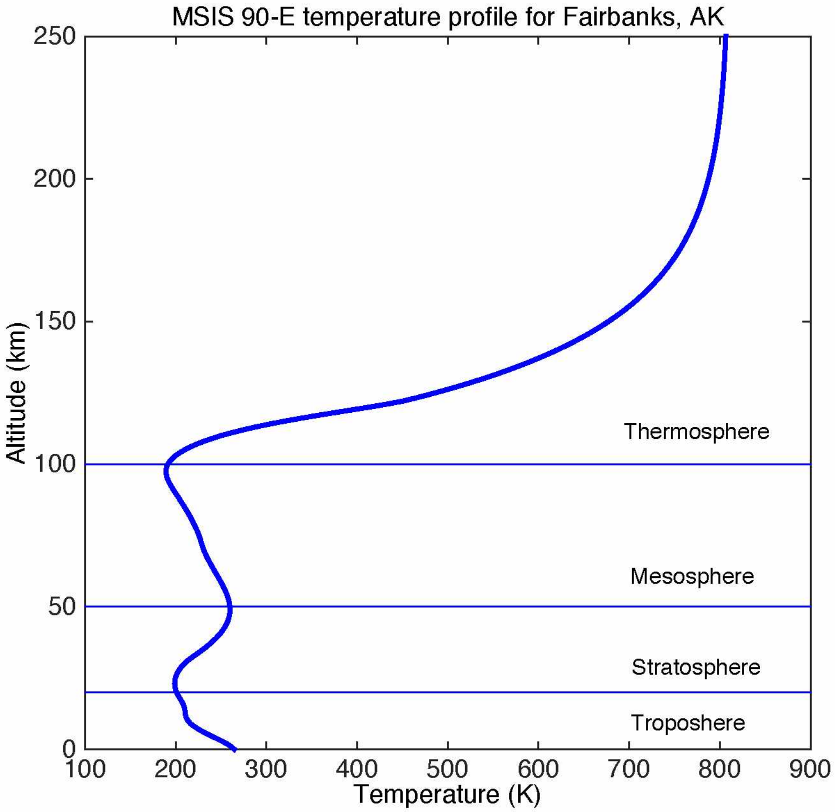

Figure 1.2. Temperature profile above Fairbanks, AK generated by MSIS-90-E model. The various temperature regimes are also shown [13].

As the density of the various gasses reduces, the pressure drops according to the familiar equations of state such as the ideal gas law. The situation is complicated by the non-linear temperature behavior with respect to altitude. Energy arriving directly from the sun, or reflected off of Earth's surface, is absorbed differently by the various aerosols present. As a result, the temperature profile for the atmosphere is highly non-linear. The MSIS model has also been used to generate a typical temperature profile. There are several distinct temperature regimes, generally termed: the troposphere (up to ~20 km), the stratosphere (up to ~50 km), the mesosphere (up to ~100 km), and the thermosphere (over 100 km). This structure has profound influences on the propagation of acoustic waves, as will be discussed in detail in the next chapter.

At altitudes above 90 km the atmosphere gradually transitions to a weakly-ionized plasma with an ion-to-neutral particle ratio usually below 1:1000 [16]. The region from ~ 85 – 600 km is termed the ionosphere, and a variety of different ion species are found there (see, for instance, the International Quiet Solar Year atmospheric composition) [17]. The region where auroral infrasound is presumed to be generated lies in the lower ionosphere where acoustic attenuation is sufficiently low for high amplitude signals to traverse the distance to Earth (more on this in Chapter 2). NASA's International Reference Ionosphere offers a model of quiet day ionospheric ion species and electron densities; examples of the common ion species' relative abundance during day and night time has been generated using this system as is seen in Fig 1.3 [18].

The principal source of ionization is photoionization from the UV spectrum of the sun, which causes a much higher ambient plasma density on the dayside of the Earth. The exponentially increasing neutral density with decreasing altitude, in combination with the decreasing solar radiative energy delivered, accounts for the sharp decline in plasma density below the ionosphere. The other major factor controlling ion composition is the recombination rate (the rate at which ions and electrons combine to form neutral molecules). The diatomic ions recombine in a dissociative process that results in two neutral atoms. This recombination rate is some 1000 times faster than that of the monatomic atoms, which recombine via radiation of a photon. This causes a substantial diurnal asymmetry in the relative abundance of ion species, with monatomic ions frequently persisting well into the night while most of the diatomic ions have long since recombined.

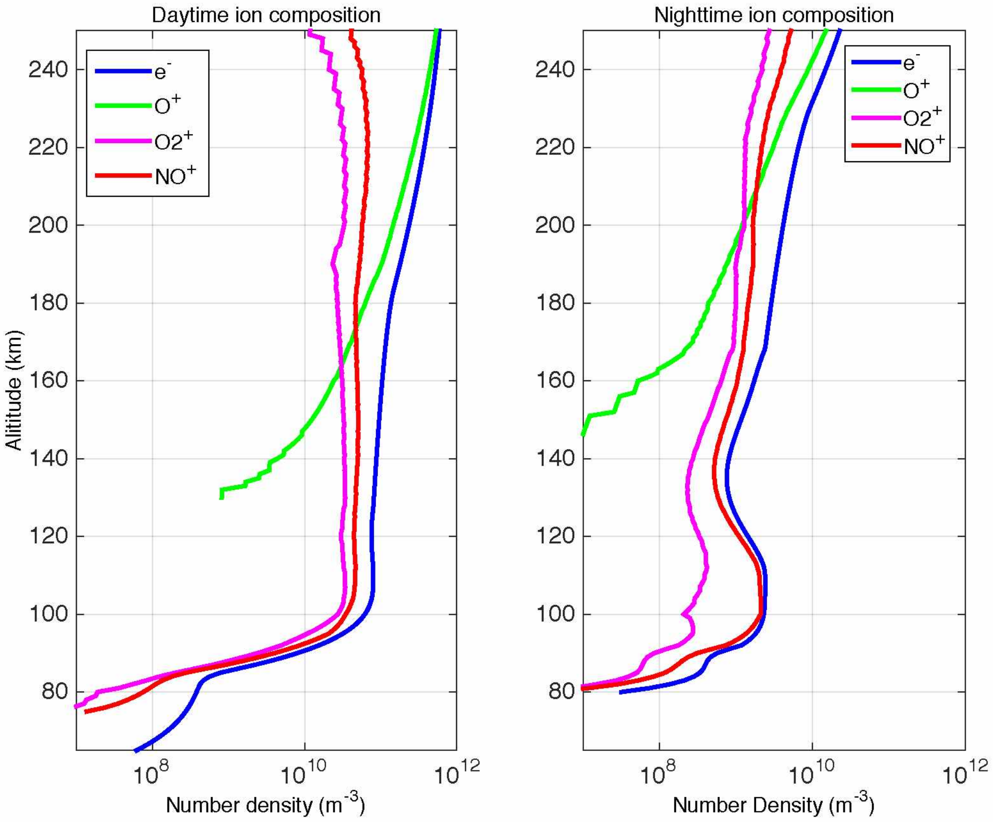

Figure 1.3 Quiet day and night ion densities of idealized ionosphere generated by NASA's International Reference Ionosphere [18]. The left panel represents the sky above Fairbanks, Alaska, for local noon, the right panel for local midnight.

1.4 The High-Latitude Ionosphere and the Aurora

At high latitudes, energetic ion/electron collision with neutral particles is another important source of ionization. Energetic electrons with energies in the range of 3-10 keV are the primary source of this ionization as they impact on the neutrals. Photon radiation from neutrals and ions excited by energetic electron collisions result in the visual aurora displays. In the auroral zone the energy deposited by energetic particles is considerable; in the E region of the ionosphere (~ 100 km) such events can produce plasma densities far greater than photoionization ever creates.

The solar wind powers the energization of the electrons responsible for the aurora through a series of complex interactions and currents set up in the magnetosphere. The surface of the sun generates sufficient heat for hydrogen and helium to be dislodged from their gravitational wells and escape into space. Particles subject to such intense heat are fully ionized plasmas; upon escaping from the compression caused by the sun's gravitational field they become supersonic. The Earth is immersed in this supersonic plasma wind emanating from the sun. Many details of the interaction between this solar wind, Earth's magnetic field, and the ambient interplanetary magnetic field remain areas of active research; furthermore, any text attempting to fully encompass this interaction would be necessarily voluminous. Here I offer only a brief and qualitative treatment.

To first order Earth's magnetic field is a dipole with axes tilted ~ 10^0 from the rotational axis. When the electrons and ions travelling in the solar wind encounter Earth's magnetic field **B**, they experience a force **F** = q**V x B** for a particle of charge *q* moving at velocity **V**. This force deflects the impinging ions dawn-ward and electrons dusk-ward, which sets up a net dusk-ward current. The magnetic field driven by this current sheet interacts with Earth's field and a force balance between the two is arrived at in a narrow region referred to as the magnetopause, approximately 10 Earth radii distant on the sunward side. Since the arriving plasma is travelling supersonically, a bow shock is created outside of the magnetopause. The solar wind is slowed to sub-sonic velocities as it makes its way around the Earth and its temperature and density rise very rapidly across the bow shock according to the Rankine-Hugoniot conditions (see, for instance, Kelly 96) [17].

As the solar wind moves around the magnetopause there is limited viscous coupling to the interior of the magnetosphere that causes some sunward drift of ions. However, the process of magnetic reconnection, involving the interplanetary magnetic field (IMF) and its coupling with Earth's field, accounts for most of the energy influx into the ionosphere that powers the aurora. At high latitudes, magnetic field lines may not be closed loops attached to Earth's poles, but rather have one end near Earth's polar region and the other connected to the IMF, forming an open field line. Far out in the magnetotail these open field lines may reconnect to form a closed loop, which appears to cause a characteristic anti-sunward surge of plasma flowing along the high latitude connected field lines, eventually resulting in significant particle precipitation in the auroral zone ionosphere. As this influx of hot plasma penetrates the ionosphere it is again subject to **V x B** forces due to Earth's increasingly strong magnetic field. The opposing motions of the electrons and ions set up the ring-current type of flow observed in the auroral arc. For a more detailed description of magnetospheric physics see, for instance, William Liu 2011 [16].

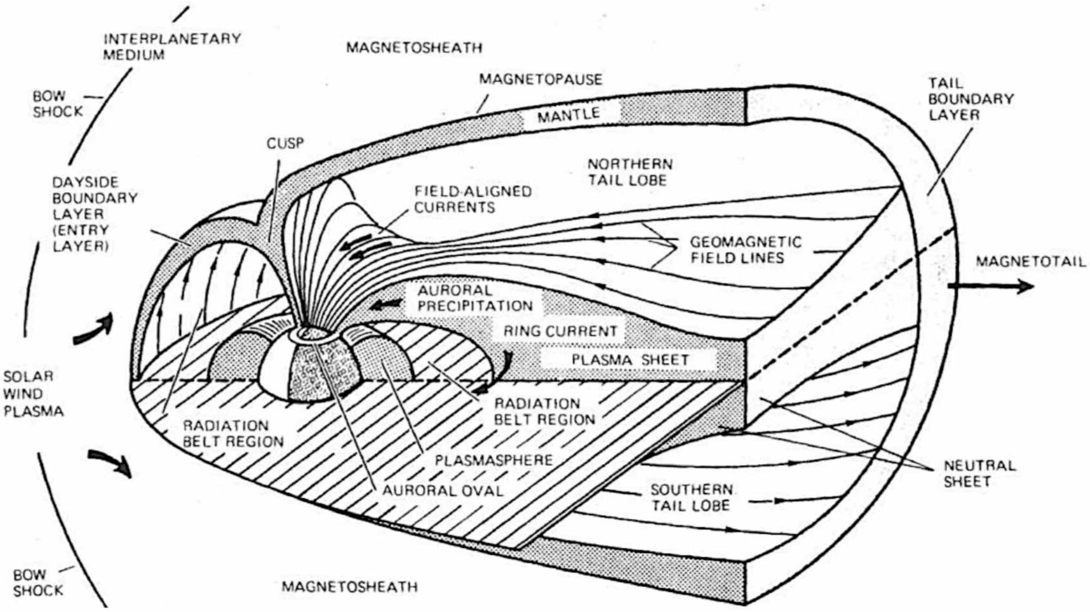

Figure 1.4. Schematic cross-section of the magnetosphere demonstrating the various regions and processes present. This image is from M.C. Kelley [19].

The auroral zone represents a narrow band around Earth's polar regions extending roughly from 65 to 80 degrees latitude. It is roughly centered about the geomagnetic poles and is both stretched equator-ward and considerably broader on the night side of the Earth. The auroral oval, where the luminous auroral bands are seen, is offset from the auroral zone by around 15^0. Within this region the visible aurora is generated at altitudes ranging from 90 to 250 km. Observational evidence alongside acoustic wave propagation considerations suggest that the ground detected auroral infrasound is most significantly produced in the lower range at about 100 km.

The aurora is most active following surges of solar activity associated with sun-spots and solar flares. Such conditions give rise to geomagnetic storms that may persist for days, over the course of which the aurora and associated geomagnetic conditions remain considerably enhanced compared to their quiet day states. On the night side of the Earth the presence of the auroral arc centered about the geomagnetic pole may become clearly visible. Over the course of several hours, it is common for this arc of aurora to expand equator-ward, form into multiple bands, and eventually break up into patchy, pulsating regions of diffuse aurora. This characteristic evolution is referred to as the auroral substorm and is closely related to the geomagnetic substorm apparent on instruments such as magnetometers. In the vicinity of the auroral arc, the lower ionosphere experiences a sudden increase in electron density due to particle precipitation from the magnetosphere, and an associated surge in conductivity. The electron rich, high conductivity region shares many characteristics with an electromagnetic current and is frequently referred to as an auroral electrojet current.

Auroral electrojet currents and energetic particle precipitation are presumed to be primary generation mechanisms for AIW. In the weakly ionized plasma environment of the lower ionosphere, even during active auroral displays, at the altitudes where the GAIW is generated the neutral molecules outnumber the ionized particles by orders of magnitude. However, the ions have profound effects on the neutral atmosphere dynamics as they drag the neutrals along with them. The coupling is primarily accomplished through Lorentz force and Joule heating interactions (although direct electron bombardment may also be a factor). In the case of AIW, travelling electrojet currents crossing the overhead zenith couple to the neutral atmosphere to setup bow shocks that traverse the long distance to the ground based sensors [2,4,20]. In the case of GAIW, the acoustic perturbations are sometimes present when no consolidated electrojet current is observed, suggesting that Joule heating and electron bombardment may play a greater role.

The lower ionosphere represents a natural laboratory for the study of partially ionized plasma dynamics. Since delivering instrumentation directly to this region usually involves a rocket, it is prohibitively expensive and data can usually only be collected for a period of seconds. This makes ground based infrasonic equipment appealing as a means of researching the ionosphere and probing the upper atmosphere/low space region. In conjunction with ionosondes, riometers, magnetometers, and other ground based sensors, studying GAIW via low-frequency response microphone arrays provides clues about the dynamics of this difficult to access part of the atmosphere.

Chapter 2

Infrasound Acoustics

2.1 The Equations of Fluid Dynamics in the Acoustic Regime

For processes associated with classical physics scales, the appropriate equations approximating fluid behavior are the continuity equation and the Navier-Stokes equations:

$$\frac{\partial \rho}{\partial t} + \nabla \cdot (\rho \vec{v}) = 0 \tag{2.1}$$

$$\rho \frac{D\vec{v}}{Dt} = -\nabla p + \nabla \cdot \overleftrightarrow{T} + \vec{f}\,, \tag{2.2}$$

where ρ is the fluid density, p the pressure, $\vec{v}$ is the vector fluid velocity, $\vec{f}$ is a general term relating the body forces acting on a fluid parcel, and $\overleftrightarrow{T}$ is a rank two tensor, referred to here as the viscous stress tensor, that describes deformation and stress due to viscous interactions. The following notation for the advective derivative operator is adopted

$$\frac{D}{Dt} \equiv \left(\frac{\partial}{\partial t} + \vec{v} \cdot \nabla \right). \tag{2.3}$$

The second equation can often be simplified by considering the relative magnitudes of the associated terms. For instance, if we consider some representative velocity scale U and length scale L, then the relative contribution due to the viscous stress tensor is of order

$$R_e = \frac{UL}{\nu_e} \approx \frac{300\frac{m}{s} \times 100m}{10^{-2}\frac{m^2}{s}} = 3\times 10^6$$

with ν_e the eddy viscosity. The values quoted are for typical atmospheric conditions [21]. Very high values for the dimensionless number R_e (for instance values greater than ~10^5), suggest that contributions due to viscosity will be negligible. The values for U and L are order of magnitude estimates of infrasound propagation velocity and wavelength. This suggests that an inviscid approximation is justified and is adopted throughout this text. Simplification of the force term is accomplished through the assumption of a stationary, non-rotating fluid. This is chosen for mathematical convenience; the effects of wind on acoustic propagation will be considered in a later section, while the rotational effects such as the Coriolis force are of much smaller magnitude and are not discussed. This leaves only the force of gravity acting on a given fluid element: $\vec{f} = -g\hat{z}$, where $\hat{z}$ is the altitudinal unit vector perpendicular to Earth's surface.

Along with the continuity and Navier-Stokes equations, an equation of state relating the pressure, density, and temperature is needed to close the system of equations. For acoustic perturbations the adiabatic (constant temperature) approximation is justified by consideration of the rate of heat conduction in the atmosphere. Heat is conducted through materials according to the heat equation

$$\frac{\partial T}{\partial t} = \frac{\alpha}{\rho c_v}\nabla^2 T\,, \tag{2.4}$$

where T is the local fluid temperature. The constant of heat conductivity, α, is dependent upon the composition and number density of the fluid and representative values may be looked up. Similarly, the specific heat at constant volume c_v has been experimentally verified for atmospheric values. The rate of heat conduction during an acoustic event is approximated by the scale height of the atmosphere divided by the period of the oscillations: H/τ. Consideration of Eq. (2.4) in the one-dimensional case yields:

$$\frac{\partial T}{\partial t} \approx \frac{T}{\tau}; \frac{\alpha}{\rho c_v} \frac{\partial^2 T}{\partial z^2} \approx \frac{\alpha T}{\rho c_v H^2}$$

$$\Rightarrow \frac{H}{\tau} \approx \frac{\alpha T}{H \rho c_v}. \tag{2.5}$$

Yeh and Lui's quotes of representative values for the pertinent constants yield heat conduction rates of order ~10^{-9} m/s near Earth's surface and ~10 m/s at 200 km altitude, which are far below the ~300 m/s rate of acoustic propagation [16]. With these considerations the equations of motion for the fluid become:

$$\frac{\partial \rho}{\partial t} + \nabla \cdot (\rho \vec{v}) = 0 \tag{2.1}$$

$$\rho \frac{D\vec{v}}{Dt} = -\nabla p - \rho g \hat{z} \tag{2.6}$$

$$\frac{Dp}{Dt} = c^2 \frac{D\rho}{Dt}, \tag{2.7}$$

where Eq. (2.6) is a statement of the adiabatic condition with c the temperature, (and thus altitude), dependent velocity of acoustic propagation.

2.2 The Linearized Equations and Dispersion Relations

For the case of a locally isothermal atmosphere, force balance equations specify that pressure and density drop off exponentially according to the equations $p = p_0 e^{-z/H}$ and $\rho = \rho_0 e^{-z/H}$ where the subscript 0 refers to the pressure and density values at sea level ($z = 0$). All of the infrasound signals we discuss in this work consist of pressure fluctuations on the order of, at most, a few Pascal. Since the ambient atmospheric pressure at sea level is of the order 10^5 Pa, the magnitude of the fluctuations about the ambient state is comparatively very small. A similar argument holds for both density and velocity. It is often informative to linearize about the background state and neglect products of the perturbed values as higher order effects that have little influence on the dynamics of the system as a whole. Specifically, taking $\rho = \rho_0 + \rho_1; p = p_0 + p_1;$ and $\vec{v} = \vec{v}_1$ (setting our background wind to zero – an effectively arbitrary choice), inserting these in equations (2.1), (2.6), and (2.7) and dropping products of perturbed values (subscript 1) we arrive at the linearized set of equations:

$$\frac{\partial p}{\partial t} + \rho_0 \left[\nabla \cdot \vec{v} - \frac{1}{H} v_z \right] = 0 \tag{2.8}$$

$$\rho_0 \frac{\partial \vec{v}}{\partial t} = -\nabla p - \rho g \hat{z} \tag{2.9}$$

$$\frac{\partial p}{\partial t} - \frac{p_0}{H} v_z = c^2 \left[\frac{\partial \rho}{\partial t} - \frac{\rho_0}{H} v_z \right] , \tag{2.10}$$

where the subscript 1 on the perturbed quantities has been dropped for convenience. It has been shown that closed-form solutions do not exist for the full, linearized system of equations [16, 22]. For the purposes of this text it is sufficient to consider the dispersion relation of harmonic waveforms in the medium. The results can then be generalized for arbitrary, well-behaved functional forms. The dispersion relation is obtained by assuming harmonically oscillating solutions for p, ρ, and $\vec{v}$; for instance $p = Ae^{i(\omega t - \vec{k} \cdot \vec{x})}$, with A an arbitrary constant. Substituting these solutions into equations (2.8)-(2.10) and performing the differentiations we arrive at:

$$i\omega p - \rho_0 \left[i\left(\vec{k} \cdot \vec{v}\right) + \frac{1}{H} v_z \right] = 0 , \tag{2.11}$$

$$i\omega \rho_0 \vec{v} = ip\vec{k} - \rho g \hat{z} , \tag{2.12}$$

$$i\omega p - \frac{p_0}{H} v_z = c^2 \left(\frac{\partial \rho}{\partial t} - \frac{\rho_0}{H} v_z \right) . \tag{2.13}$$

A variety of algebraic methods can be applied to eliminate p, ρ, and $\vec{v}$ from the above equations. The resulting relationship between the frequency and wave number is given by

$$\frac{\omega^2}{c^2}\left(1-\frac{\omega_a^2}{\omega^2}\right)=k_h^2\left(1-\frac{\omega_g^2}{\omega^2}\right)+k_z^2 \tag{2.14}$$

where $k_h^2 = k_x^2 + k_y^2$ defines the horizontal wave number, $\omega_a = c/2H$ is the acoustic cutoff frequency, and $\omega_g = (\gamma-1)^{1/2} g/c$ is the Brunt-Väisälä frequency defining the high frequency cut-off for gravity waves. For the travelling acoustic-type waves that we're interested in we seek solutions such that $k_h \neq 0$ and k_z has a real component. This defines three branches of the dispersion function: acoustic type disturbances where $\omega > \omega_a$, gravity wave type disturbances where $\omega < \omega_g$, and the null-propagation case where the frequency lies between the acoustic and gravity wave cut-off frequencies. The case $\omega = \omega_g$ is referred to as the Lamb wave. It's worth mention that the gravity-wave branch disturbances do not propagate, but remain localized to their source regions.

It is immediately apparent that for frequencies that satisfy $\omega >> \omega_a$ the waves become non-dispersive and we recover the familiar relationship for acoustic waves: $c = \omega/k$. Auroral infrasound is frequently observed with significant amplitudes propagating at higher frequencies that satisfy non-dispersive conditions. However AIW and in particular GAIW usually propagate with significant contributions at frequencies very near the Brunt-Väisälä frequency in the lower troposphere. Here we treat the dispersion effects briefly and qualitatively; detailed discussions are a matter of continued research and can be found in the references [23-28]. Examination of Eq. (2.14) shows that the propagation speed c is decreasing for frequencies near the acoustic cutoff. A cartoon has been generated below to observe the effects of retarding the low frequency content of a waveform. In figure *2.1a* a waveform has been generated by summation of sinusoids. Figure *2.1b* depicts the same summation of sinusoids but with the sinusoids shifted to the right (retarded in time) proportionally to the inverse square of their frequencies.

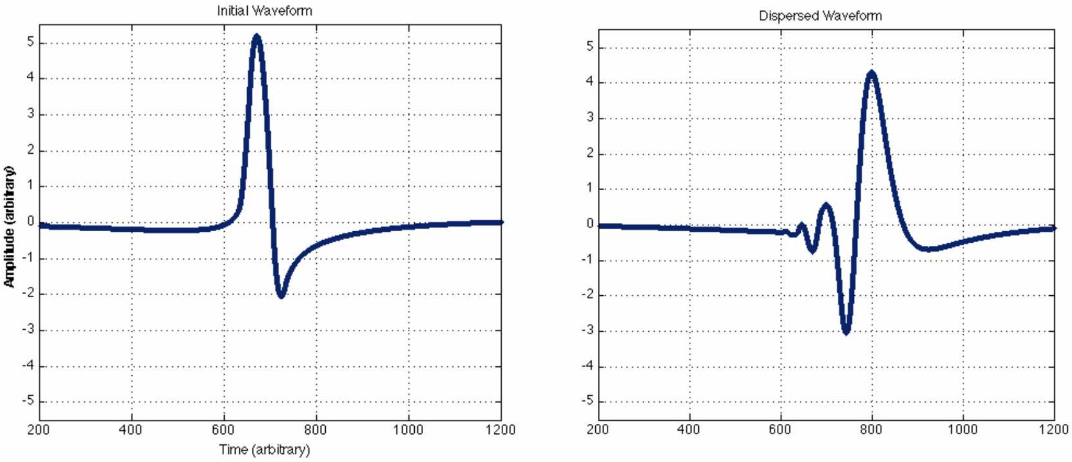

Figure 2.1. A cartoon of the effects of dispersion on an impulsive waveform is illustrated. The initial waveform is generated as a summation of sinusoids. Retarding the lowest frequency components results in the dispersed waveform that is broadened in time and exhibits oscillations of increasing period.

The effect of this dispersion on a pulse or N-wave type pressure waveform will be to broaden the signal in time and give a low-frequency ringing of increasing period [5]. While this signal distortion creates additional concerns when relating a specific, distant event to a received pressure signal, we will see that for auroral infrasound enough high-frequency content is usually present in the signal to allow association of acoustic events with causal geomagnetic disturbances. The substantial uncertainty in the intervening atmospheric conditions, wind components, and general fluid dynamics within the auroral arc present additional complications in modeling specific waveforms that, combined with low-frequency dispersion, make some distortion in waveforms expected and leave sufficient information for inverse modeling questionable. However, all of these effects require length scales far greater that the aperture of the receiving array such that well correlated signals are received at the various sensor elements and beam forming remains valid.

2.3 Infrasonic Propagation in the Atmosphere

While dispersion effects have some impact on the lowest frequency components of infrasonic wave propagation, these dispersion effects take place over length scales of hundreds of kilometers. Much of the energy within propagating infrasonic disturbances is in higher frequency content that suffers very little dispersion. For purposes of first-order propagation estimations it is usually valid to consider the properties of the pure acoustic branch. The methods described below may be generalized to include acoustic gravity dispersion effects, although the required mathematical development is quite lengthy and is omitted from this text for brevity.

For frequencies above ~ 0.05 Hz the gravity term in equation 8 becomes negligible. The exponential dependence of pressure and density allow us to approximate $p = c^2\rho$. Then combining equations 2.8 and 2.9 with the appropriate differentiations yields the familiar wave equation (here I've chosen to solve for the pressure, although similar conditions hold for both density and velocity)

$$\frac{\partial^2 p}{\partial t^2} = c^2 \nabla^2 p \,. \tag{2.15}$$

The specific generation mechanisms, boundary conditions, and atmospheric profile are necessary to produce unique solutions to Eq. (2.15). Here we consider plane wave propagation since the high trace velocity infrasonic signals considered in this text are shown to be planar to high precision. The results can easily be generalized for spherical wave fronts and other geometries.

For waves of frequency ω, a basic wave field that satisfies Eq. (2.15) is

$$p(\vec{r},t) = Ae^{i(\vec{k}\cdot\vec{r}-\omega t)} \,, \tag{2.16}$$

where A is the wave amplitude. For such a wave field in a homogeneous medium, a line normal to the wave front for all time t will be a straight line. However, the stratification of the atmosphere results in anisotropy in the propagation speed with resultant refraction. The dependence of sound speed on altitude can be established based on thermodynamic formulas. It has been empirically shown that for acoustic waves in the atmosphere, as the expansion and rarefaction of the gasses happens at much shorter time scales than the local heat conduction rate the process is adiabatic to good approximation [27]. This gives

$$\frac{p}{p_0} = \left(\frac{\rho}{\rho_0}\right)^{\gamma}, \tag{2.17}$$

where $\gamma = c_p/c_v$ and c_p and c_v are the specific heats of the medium at constant pressure and volume respectively. Noting that $p = c^2\rho$ implies $dp/d\rho = c^2$ we can differentiate Eq. (2.17) with respect to ρ and note that

$$c^2 = \frac{d}{d\rho}\left[\frac{p_0}{\rho_0^{\gamma}}\rho^{\gamma}\right] = \frac{\gamma p}{\rho}. \tag{2.18}$$

Finally, if we make the usual approximation that the ideal gas law holds in the atmosphere we have $p = \rho RT$ and substituting into Eq. (2.18) yields

$$c = \sqrt{\gamma RT} \tag{2.19}$$

where $\gamma \cong 1.4$ for dry air, $R = 287$ J/kg/K, and T is the air temperature in Kelvin. Figure 2.2 displays a typical sound speed profile in the atmosphere. A temperature profile was generated using NASA's MSIS 90-E model atmosphere, then Eq. (2.19) was used to compute the sound speed.

For a point source emitting sound at a constant, monotone frequency a first order solution for the wave-front normal may be developed according to the usual ray-tracing methods (see, for instance, Computational Ocean Acoustics) [29]. For infrasonic signals that occupy a broad frequency band such ray tracing algorithms are generally thought of as zeroeth order approximations that nonetheless give insight into the general trend of refraction effects on the direction of propagation. Such ray tracing diagrams are often used in the infrasound community to illustrate broad points relating to infrasonic refraction where highly detailed quantitative analysis is not required. Ray tracings generated in this way are provided below for a point source emitting at 1 HZ and are displayed in figure 2.3. Panel a) displays ray paths for a point source on the ground with takeoff angles ranging from 10^0 – 70^0 measured counter-clockwise from horizontal. Panel b) displays ray paths with takeoff angles ranging from 10^0 – 70^0 measured counterclockwise from horizontal. It should be noted that these ray tracing algorithms do not account for attenuation. The altitude dependent attenuation squelches waves propagating above about ~120 km and this, alongside high wind shears and other factors, make detection of a refracted wave that has passed through such high altitudes doubtful.

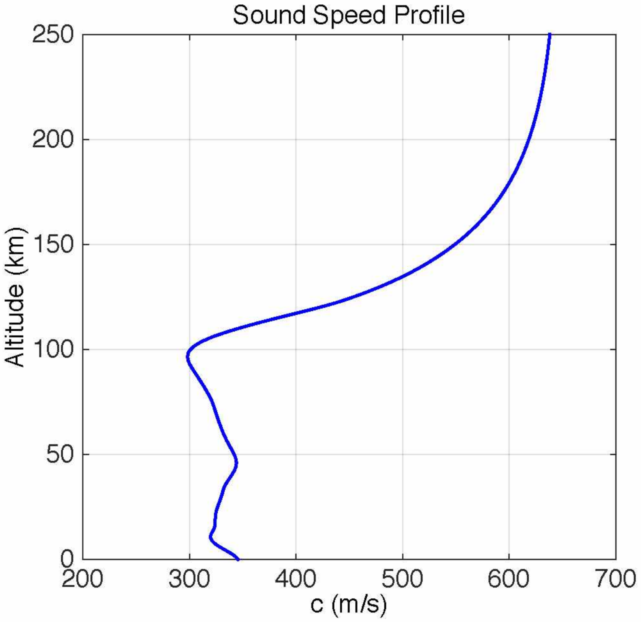

Fig 2.2. Model atmosphere sound speed profile. The sound speed profile has been generated utilizing equation 2.19 with the temperature profile provided by the MSIS 90-E model.

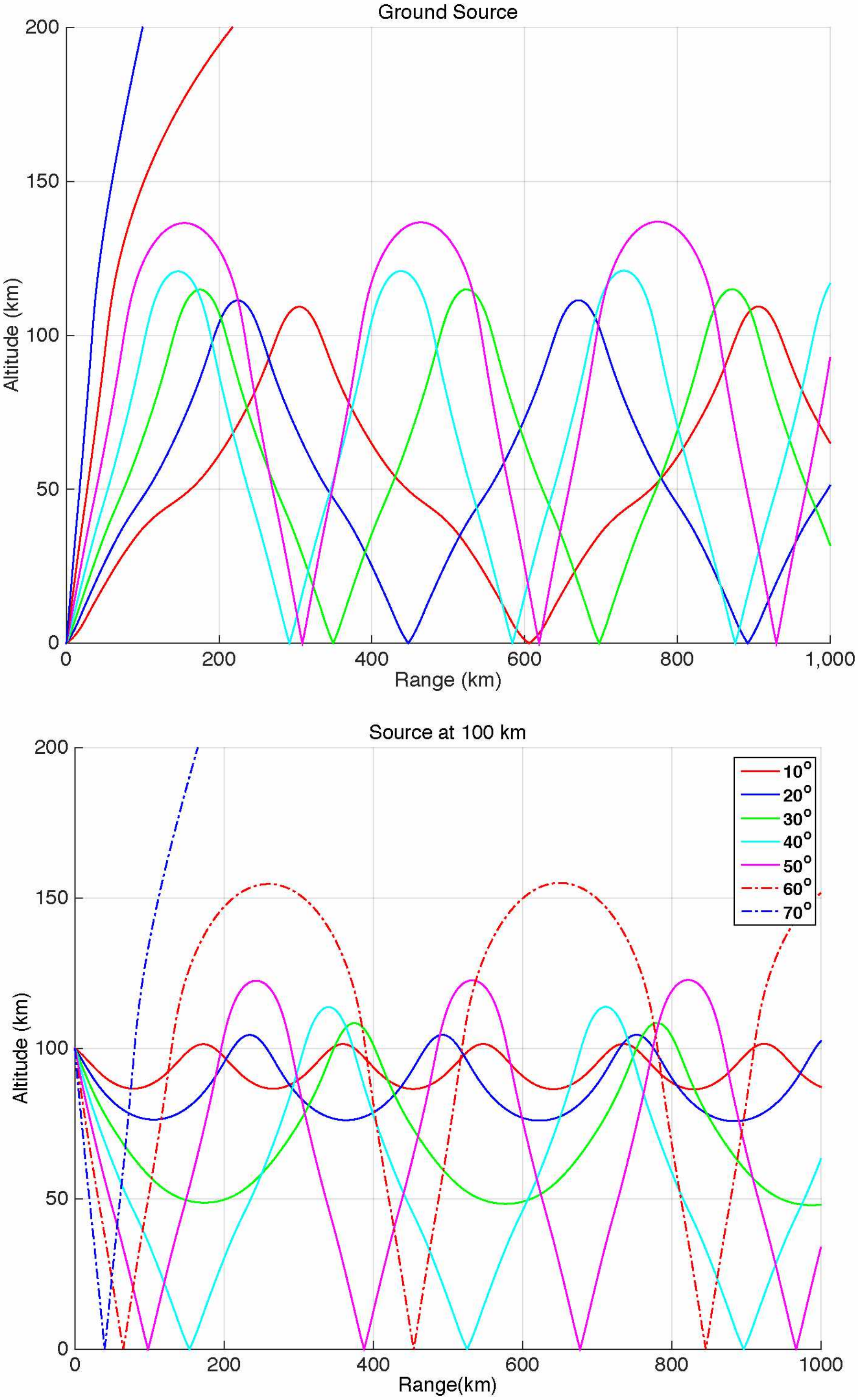

Fig 2.3. Ray tracing diagrams for (top panel) a point source located on the ground and (bottom panel) a point source located at 100 km altitude. The legend denotes the takeoff angle from horizontal, measured counterclockwise in panel a) and clockwise in panel b). the frequency is 1 Hz.

The ray tracing diagrams depicted in Fig. 2.3 illustrate the important concept that for certain takeoff angles ground source propagating waves will be refracted back to the surface, while sources located in the lower ionosphere will be refracted away from Earth's surface for takeoff angles close to horizontal. In fact, for a source at 100 km infrasonic disturbances propagating away at angles from the horizontal of less than approximately 40^0 will never reach ground-based sensors. This is an important result as it restricts the region underneath a high altitude source that can be expected to receive infrasound signals.

As a sound wave travels through the atmosphere its energy is lost to any radial spreading that occurs as well as physical processes such as relaxation of the oxygen molecules. In the lower atmosphere relative humidity plays a major role, whereas in the ionosphere the plasma dynamics have a large impact. At high altitudes, models of acoustic attenuation remain a major contemporary goal in the acoustics community [23, 30, 31]. The primary mechanism of sound attenuation in the neutral atmosphere is molecular relaxation from vibrational and torsional excitation of the oxygen, nitrogen, and water vapor. Shear viscosity and to a much lesser extent thermal diffusion also contribute. Estimates of attenuation usually depend on temperature, pressure, and relative humidity. Using the model parameters discussed above, the sound attenuation (neglecting geometric spreading) has been estimated based on the model by Bass and is displayed in Fig. 2.4 as a function of frequency [31]. For a source at 1 km altitude, the estimated parameters are taken as 20^0 C temperature, 1 atm pressure, and 50% relative humidity. For a source at 50 km the parameters are taken as: -10^0 C for temperature, 0.001 atm pressure, and 0.01% humidity. Clearly absorption is much greater for higher frequencies. In fact, infrasonic signals can travel many kilometers with very little attenuation as suggested in Fig. 2.4., particularly in the case of plane waves where little geometric spreading is occurs. Acoustic attenuation also tends to be much higher at high altitudes where the pressure is much lower. As a result, even should high frequency content be present at high altitudes, very little is expected to remain after a signal has traversed the distance to ground based sensors. For the source at 100 km altitude then, little or no acoustic energy is predicted to reach the ground at ranges of over 200 km from the source.

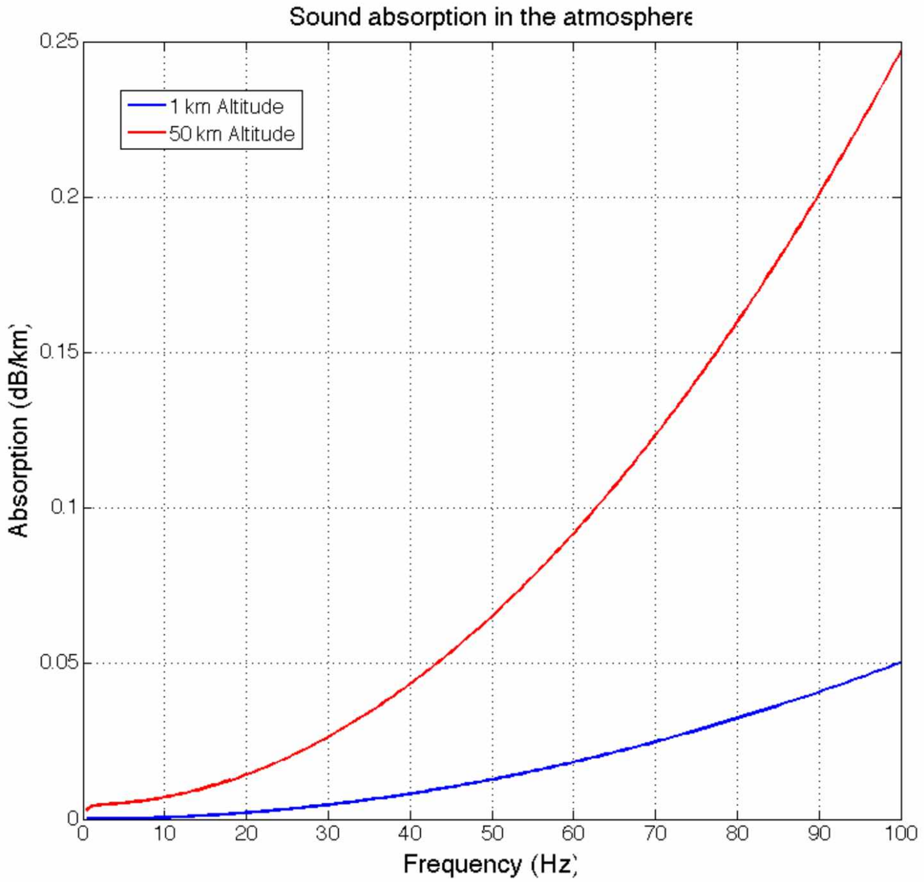

Fig 2.4. Bass model of atmospheric absorption as a function of frequency for ground level and approximately 50 km altitude parameters. At 1 km, the parameters used are 20^0 C temperature, 1 atm pressure, and 50% relative humidity. At 50 km the parameters are 10^0 C, 0.001 atm and 0.01% humidity.

2.4 CTBT/IMS Infrasound Arrays I53US and I55US

The acoustic data considered throughout this text is primarily gathered at CTBT/IMS (Comprehensive Test Ban Treaty/International monitoring system) infrasound arrays I53US located in College, Alaska (65^0 N 148^0 W) and I55US located in Windless Bight Antarctica (78^0 S 168^0 E). Both stations are eight-element arrays arranged in a pentagonal pattern of approximate aperture distance of 1.7 km with a centered, interior triangle of approximate aperture of 170 m. The array geometries are illustrated in Fig 2.5.

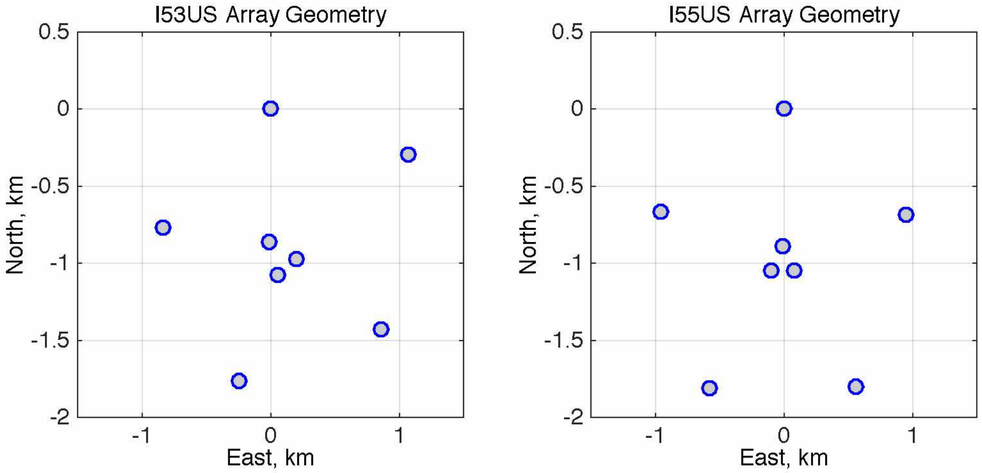

Fig. 2.5 Array geometries of I53US (left) and I55US (right) microphone arrays in km North and East of 0,0.

The microphones that constituted the array elements during the period encompassed by this study were Chaparral Model 5 sensors. These microphones are designed to have a roughly flat frequency response across a broad pass band in the infrasonic range as well as very low self-noise. Spatial averaging and initial low-pass filtering are accommodated by venting the sensors to the atmosphere through a system of noise reducing pipes. We primarily consider I53US in this text, which utilizes a pipe system venting each sensor as illustrated in Fig. 2.6. The air intakes are at the end of the pipes that make up the florets at the terminals of the four primary intake lines. Each floret is made up of 24 smaller intake pipes. At I55US the pipes are of a different design owing to environmental considerations, but the overall effect of wind noise reduction is similar.

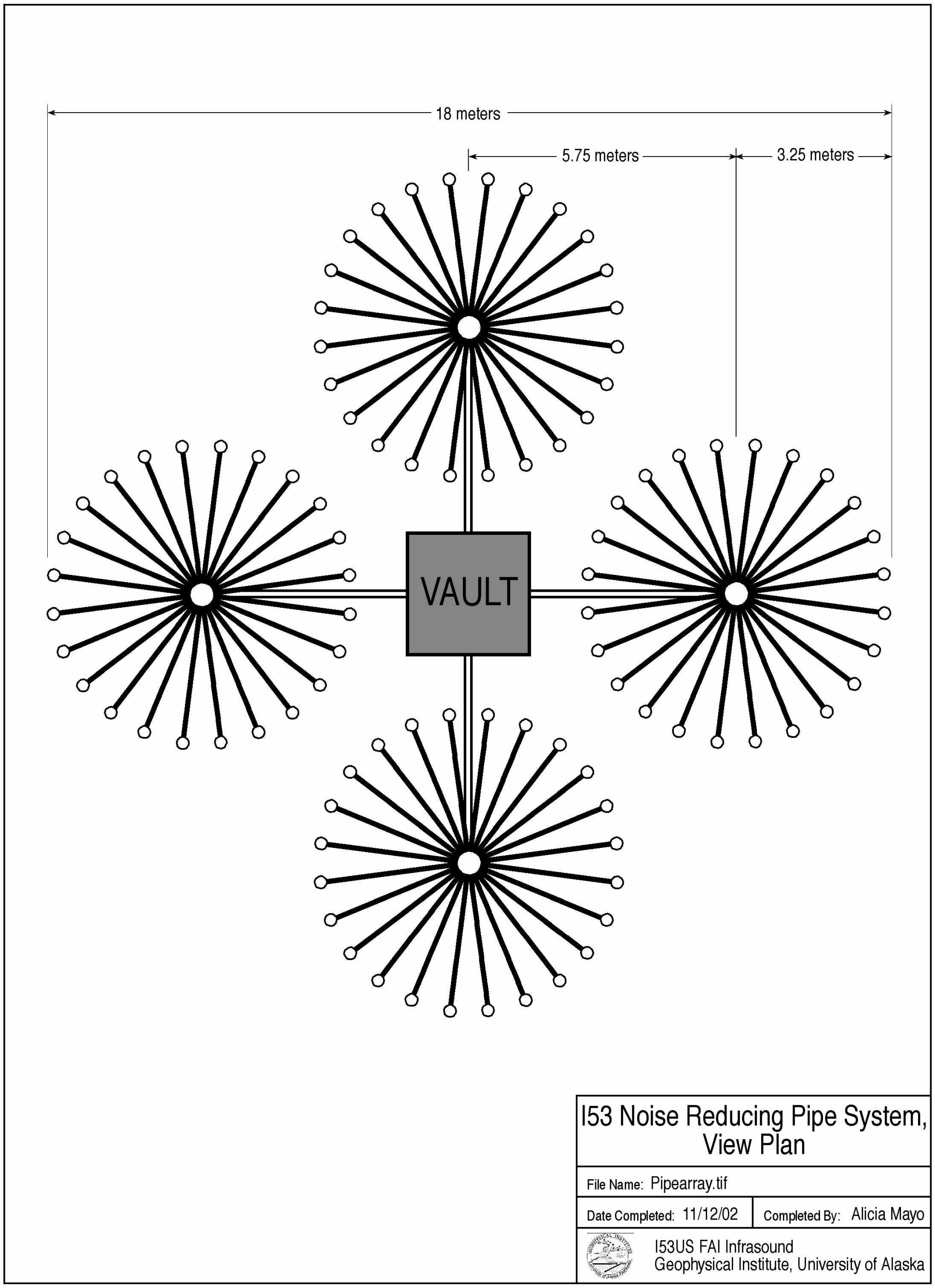

Fig. 2.6. Layout of the intake pipe system for the I53US microphone array.

The array I53US lies in College, Alaska at approximate geological coordinates 64.8° N, 147.8° W, while I55US at Windless Bight, Antarctica lies at 77.4° S, 167.3° E. These stations are ideally situated for observation of auroral infrasound as they both frequently lie within or just outside of the auroral oval during geomagnetically active times. Interestingly, the skew in Earth's magnetic pole has the effect of making it uncommon for both stations I53US and I55US to lie within the auroral oval simultaneously.

2.5 Linear Least-Squares Method of Beamforming

Consider a coherent pressure time series signal that is received across an array of *n* sensors. We would like to estimate the apparent velocity, back azimuth directivity, and a measure of the coherence of the signal. The following strategy is adopted, with notation closely following Szuberla and Olson 2004 [32]. The microphone arrays we consider are planar to excellent approximation; we designate the location of the *i*th array element as $[x_i, y_i]$ with the coordinate system chosen such that one of the elements lies at the origin. There are $N = n(n-1)/2$ unique separation vectors between array elements that we imbed in an $[N,2]$ matrix **X**. For infrasound generated in the ionosphere, the great distances between the source and the array ensure that the travelling perturbations may be treated as plane waves. Adopting Dirac's succinct Bra-ket notation for linear systems, we utilize the model for planar signal arrival [33]

$$|\tau\rangle = X|s\rangle + |\varepsilon_\tau\rangle \tag{2.20}$$

The vector $|\tau\rangle$ encodes the time delays between the arrivals, $|s\rangle$ is the slowness vector, the elements of which have units of inverse velocity and are related to the inverse of the signal velocity via a conformal mapping, and $|\varepsilon_\tau\rangle$ is the vector of uncertainties in $|\tau\rangle$. The actual vector of time delays is computed by determining the delays that maximize the mean of the cross-correlation maxima. We then seek a solution of Eq. (2.20) for $|s\rangle$ that minimizes the sum-squared error in $|\tau\rangle$, $\langle\varepsilon_\tau|\varepsilon_\tau\rangle$. Noting that $\langle\varepsilon_\tau|\varepsilon_\tau\rangle = \langle\tau - Xs|\tau - Xs\rangle$, we differentiate with respect to the slowness and set the result equal to zero. The resulting equation satisfies

$$|s\rangle = C|\tau\rangle \tag{2.21}$$

where the matrix C, known as the covariance matrix of intersensor separation, is defined as $C = X^T X$ where the superscript T denotes the adjoint of the matrix. Given a d dimensional estimate of $|s\rangle$ we can compute the trace velocity by

$$v_i = \frac{s_i}{\sum_{i=1}^{d} s_i^2}. \tag{2.22}$$

For the 2 dimensional case that we consider, the back azimuth is computed as the direction anti-parallel to $|s\rangle$:

$$\theta_A = \tan^{-1}\left(\frac{S_x}{S_y}\right). \tag{2.23}$$

Before applying the algorithm described above to real data sets, it is important to understand the assumptions and quantify the uncertainties associated with the model. There are a variety of factors that contribute to errors in measurements of $|\tau\rangle$, both physical noise (wind noise and turbulence effects, rapid temperature changes, multi path arrivals of signals, etc.), and artifacts of the data collection methods (finite sampling effects, sensor self noise, unexpected resonant cavities within the system, etc.). For the purposes of this thesis we assume the errors in the measured values of $|\tau\rangle$ and $|s\rangle$ to be normally distributed about the idealized theoretical values $|\tau_0\rangle$ and $|s_0\rangle$. Previous studies have shown this to be a good approximation for band pass filtered data in which the effects of turbulence on the noise distribution have been limited [32]. Then an estimate of the variance in $|\tau\rangle$ is give by [32]

$$\sigma_\tau^2 = \frac{\langle\tau|(I-R)|\tau\rangle}{N-r}, \tag{2.24}$$

where

$$R = XC^{-1}X^T, \tag{2.25}$$

and where r, the rank or R, is identically 2 for a two-dimensional array. Development of a probability density function for $|s\rangle$ requires the projection of the residuals onto the eigenspace of C. Since C is seen to be diagonalizable its matrix of eigenvectors E and eigenvalues D are factored via

$$D = E^T CE. \tag{2.26}$$

We define the projected residuals of $|s\rangle$ by

$$|\delta\rangle \equiv E^T\left(|s\rangle - |s_0\rangle\right). \tag{2.27}$$

The desired probability density function is then given by [34]

$$f\left(|s\rangle\right) = Ae^{-(1/2\sigma_\tau^2)\langle\delta|D|\delta\rangle} \tag{2.28}$$

where A is a normalization constant that we need not specify. Clearly f is constant if the exponent in Eq. (2.28) is. Following the statistical convention we denote the values of constant probability by $\Delta\chi^2_{\nu|p}$, meaning χ^2 for the system with ν degrees of freedom and fixed at confidence p. Finally, then, we arrive at

$$\Delta\chi^2_{\nu|p} = \frac{\langle\delta|D|\delta\rangle}{\sigma_\tau^2} = \sum_{i=1}^{d}\frac{D_{ii}\delta_i^2}{\sigma_\tau^2}. \tag{2.29}$$

For a two-dimensional array Eq. (2.29) defines an ellipse within which we expect to find a fraction p of the estimates $|s\rangle$ of the theoretical slowness vector $|s_0\rangle$. In this text we consider the far more intuitive trace velocity rather than the slowness, so we conformally map the ellipses back to velocity space via Eq. (2.22). The trace velocity V_t gives the component of the velocity in the plane of the array. A similar ellipse may then be generated to display the characteristic variation in back azimuth computation.

For both the cases of velocity and azimuth the area of the ellipses increase with increasing trace velocity. This is in keeping with physical intuition; for a source near the overhead zenith the time delays between sensors are very small and resolution of trace velocity and back azimuth becomes untenable. Observations of persistent high trace velocity geophysical signals generally show velocity space distributions commensurate with the confidence ellipses discussed above. Fig. 2.7 displays 90% confidence velocity ellipses for the CTBT/IMS infrasound arrays I53US and I55US for trace velocities ranging from 0.35 – 1.5 km/s. The ellipses were generated using an impulsive waveform test signal with center frequency 0.05 Hz and σ_τ = 0.05. The azimuth of arrival is 90^0. These figures demonstrate that uncertainties for a signal satisfying $V_t \geq 1.5$ km/s are roughly and order of magnitude larger than those for a ground based source.

In terms of signal detection, the continuously generated data from the eight sensor elements is broken up into temporal windows. For each time window, the cross correlation is then calculated for each non-redundant sensor pair. The mean of the cross correlation maxima [MCCM] is determined as an output value of the detection algorithm and provides a valuable measure of signal coherence. As an example, Fig. 2.8 displays a typical signal detection summary of the Fisher F-statistic (a measure of the signal to noise ratio), MCCM, trace velocity, and back azimuth for array I53US on JD 22 2013. The red circles represent signals detected that satisfied MCCM > 0.6. Such detection summaries are commonly used in the infrasonic communities and are frequently referred to throughout the body of this text. Also note that throughout this paper JD is abbreviated to day of year.

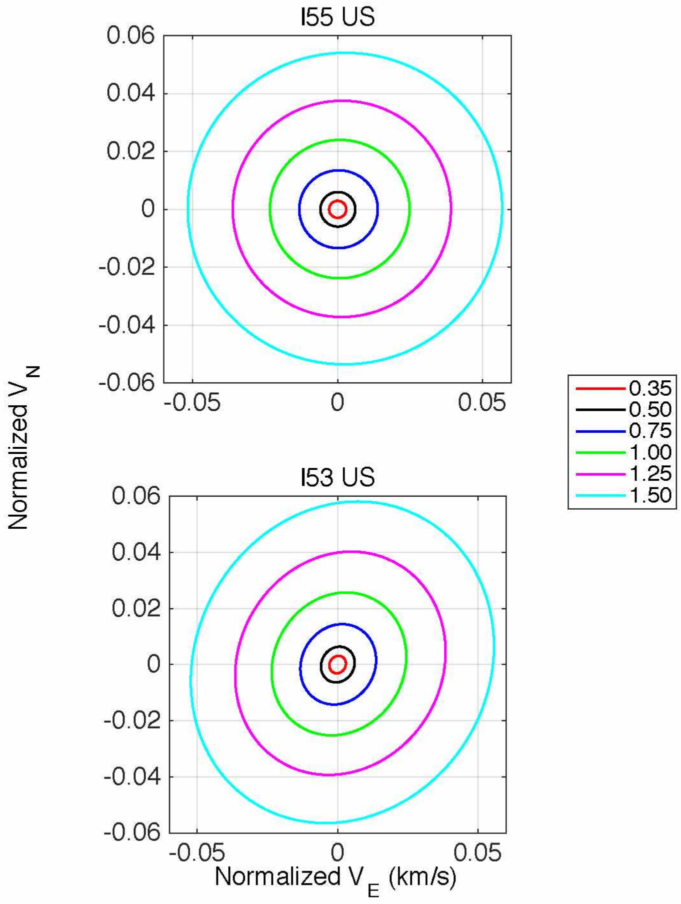

Figure 2.7. Velocity confidence ellipses for infrasound stations I55US and I53US. The ellipses encompass 90% confidence limits for the trace velocities shown in the legends (km/s). The test signal used to generate the ellipses is an impulse form with center frequency of 0.05 Hz and σ_τ = *0.05. The azimuth of arrival is* 90^0.

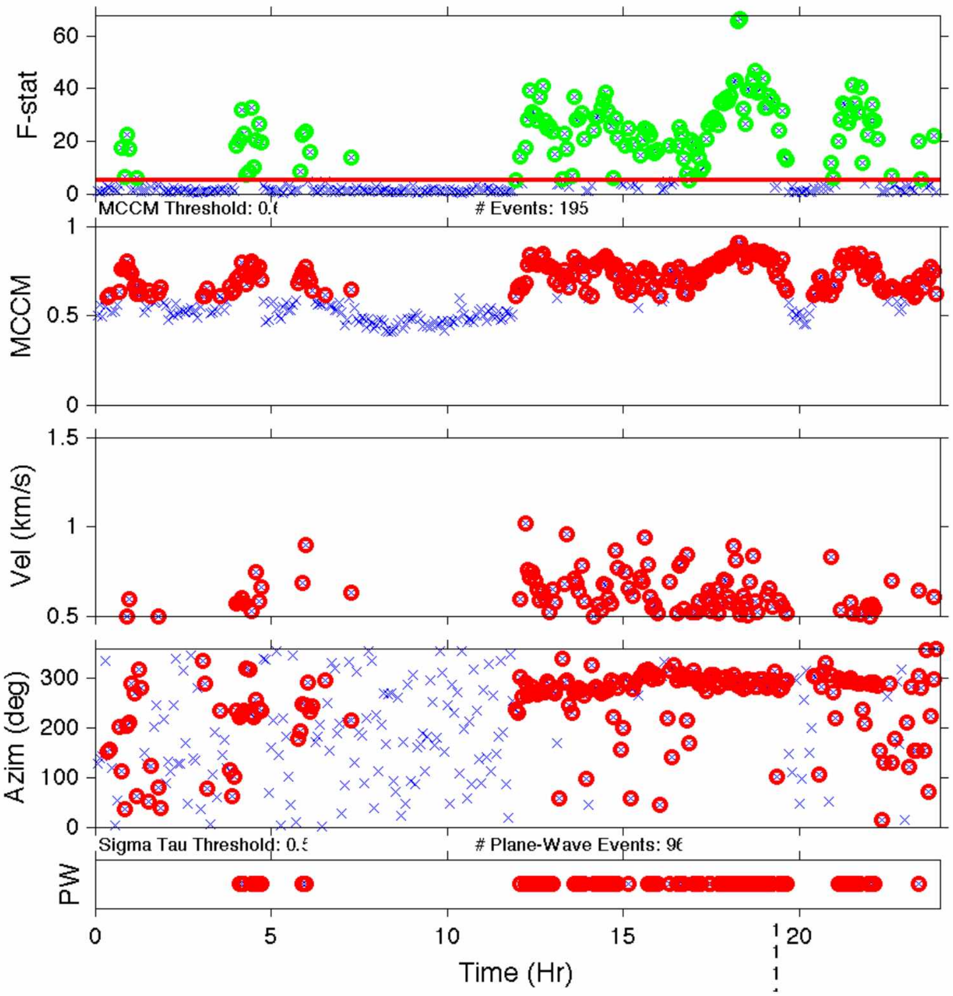

Figure 2.8 Example of an acoustic signal summary. This is a typical plot of parameters associated with signal detection algorithms (in this case is for array I53US on JD 22 2013). The Fisher F-statistic, mean of the cross correlation maxima, trace velocity, and back azimuth estimates are presented for 24 hours of data.

2.6 High Trace Velocity Signals

At both the I53US and I55US infrasonic stations signals are routinely observed with computed trace velocity far exceeding the speed of sound in air. If the source of the signal is not nearby the station such that planar arrival is a good approximation then these signals should be interpreted as having a source direction elevated from the plane of the array. It is not unusual for such high trace velocity signals [HTV's] to achieve trace velocities of well over 1000 km/s. Assuming a relatively constant sound speed in the neighborhood of the array the trace velocity is related to the sound speed by secant of the elevation angle ϕ.

A variety of geophysical sources of high trace velocity signals have been identified. Stations nearby mountainous areas frequently detect signals associated with hydrodynamic turbulence caused by air passage over the mountain ranges. These mountain associated waves [MAW] are common throughout Alaska and at I55US in Antarctica. At mid to high latitudes active auroral conditions contribute another common source. Bolides and lightning generate short-term high trace velocity signals. Displacement of the microphones during earthquakes also appear in the data as high trace velocity events. Of these geophysical sources, MAW shares the most parameter space with GAIW and as such is the most likely to be misinterpreted as auroral infrasound when it appears in conjunction with active geomagnetic conditions.

Ground source signals that have been refracted back to Earth can also be sources of high trace velocity signals. For take-off angles greater than $\sim 50^0$ a refracted signal is expected at some hundreds of kilometers from the source. Typically such signals suffer considerable attenuation before they are received. Even so, for very high amplitude, low frequency signals they are sometimes observed (volcanic eruptions provide good examples). Usually, refracted signals follow a high amplitude direct arrival signal carrying a similar waveform.

2.7 Mountain Associated Waves – Acoustic Signature

MAW's generally may be identified as high trace velocity signals that demonstrate: a strong seasonal dependence, no discernible diurnal variation, and persistent back azimuth directed towards a known mountainous region. The waves are associated with hydrodynamic turbulence generated as tropospheric winds pass over mountain ranges [35]. These turbulent infrasonic signals are routinely observed hundreds of kilometers from the source mountain ranges. It's not uncommon to observe temporally persistent MAW lasting for hours or even days.

At the station I53US several distinct sources of MAW in the surrounding terrain have been identified. The Alaska Range to the south, including Denali (North America's highest peak) is the most significant contributor. MAW also arrives from the Seward and Chukotsk peninsulas to the west and the St. Elias range to the southeast. Some occasional scattered MAW also arrive from the north, probably associated with the Brooks Range, although they are far less common. While fewer MAW events are observed in Antarctica at I55US there are mountainous regions in nearly every direction from the sensors. Most of the MAW signals received there come from the North, although the specific causal mountain ranges remain ambiguous, as there are multiple candidate ranges to the north but only one sensor array in the area.

Wilson et al. have provided an in-depth summary of MAW observed at I53US and I55US [35]. Their results, along with subsequent analysis, suggest MAW rarely exhibit trace velocities above 0.6 km/s, an important observation as it may be used to distinguish MAW from GAIW events. The waveforms are irregular but highly coherent across the array with MCCM values generally above 0.95; Fisher F-stat values generally average around 50. In the spectral band of primary interest between the Brunt-Väisälä frequency and the microbarom surge at ~ 0.2 Hz the spectrum of MAW exhibits a characteristic exponential decay with increasing frequency similar to the decay of turbulent wind noise (which it shares many common features with). There are no persistent spectral peaks or troughs. Fig. 2.9 displays a signal detection summary typical of an MAW event. This MAW event began on JD 35 2013 and lasted intermittently for more than 24 hours. Typical for MAW, the back azimuth estimate is very consistent averaging $\sim 280^0$ throughout the event. The trace velocity rarely exceeds 0.6 km/s. The MCCM remained above 0.95 throughout and the Fisher F-statistic, while exhibiting more variation, averaged ~ 50. Fig 2.10 demonstrates typical waveforms observed over 15 minutes during an MAW event with the phase-aligned overlay of the traces appearing in the bottom panel. A power spectral density [PSD] of the MAW event is displayed in Fig 2.11. The PSD was generated using Welch's method with a Hamming window of 500 seconds and 50% overlap between windows.

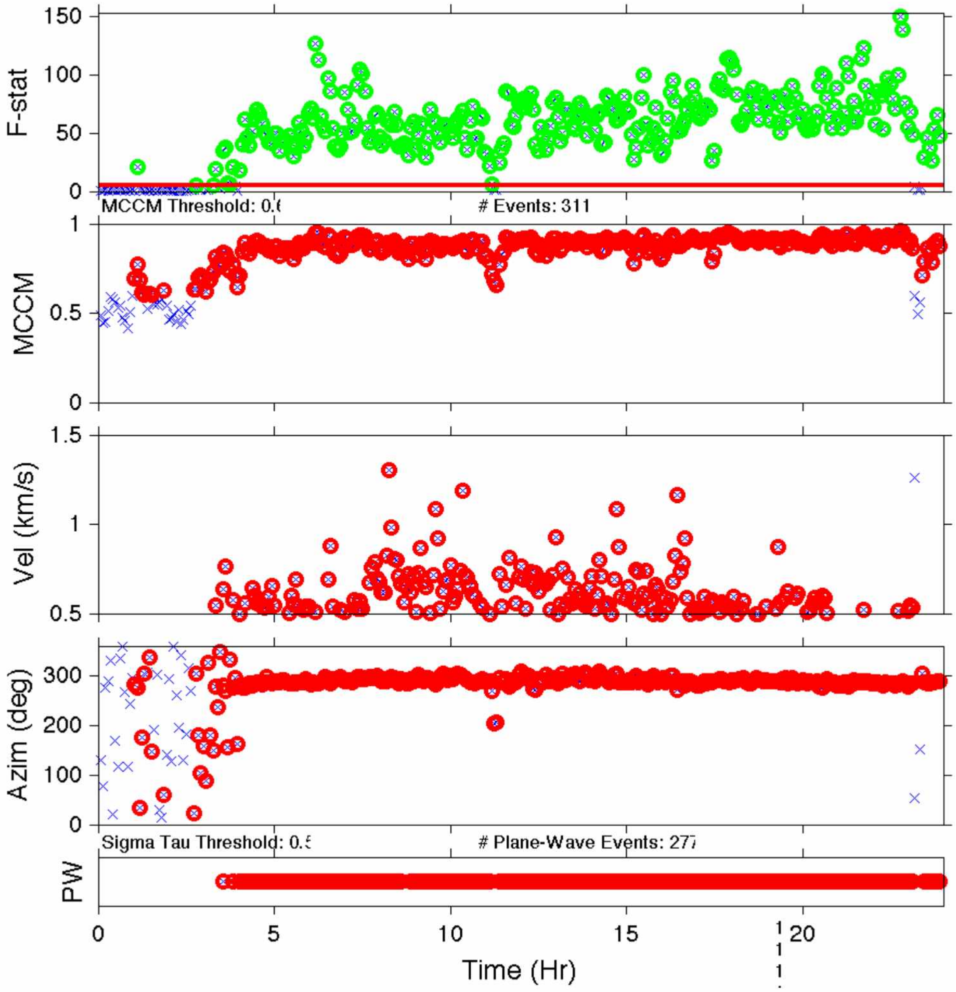

Fig 2.9. 24 hour summary of signal detections during a sustained MAW event beginning on JD 35 2013. The Fisher F-statistic, mean of the cross correlation maxima, trace velocity, and back azimuth estimates are presented for 24 hours of data. The MAW exhibits an average trace velocity of roughly 0.6 km/s. The back azimuth is temporally persistent at ~ 280^0 for many hours, and the signal is highly coherent

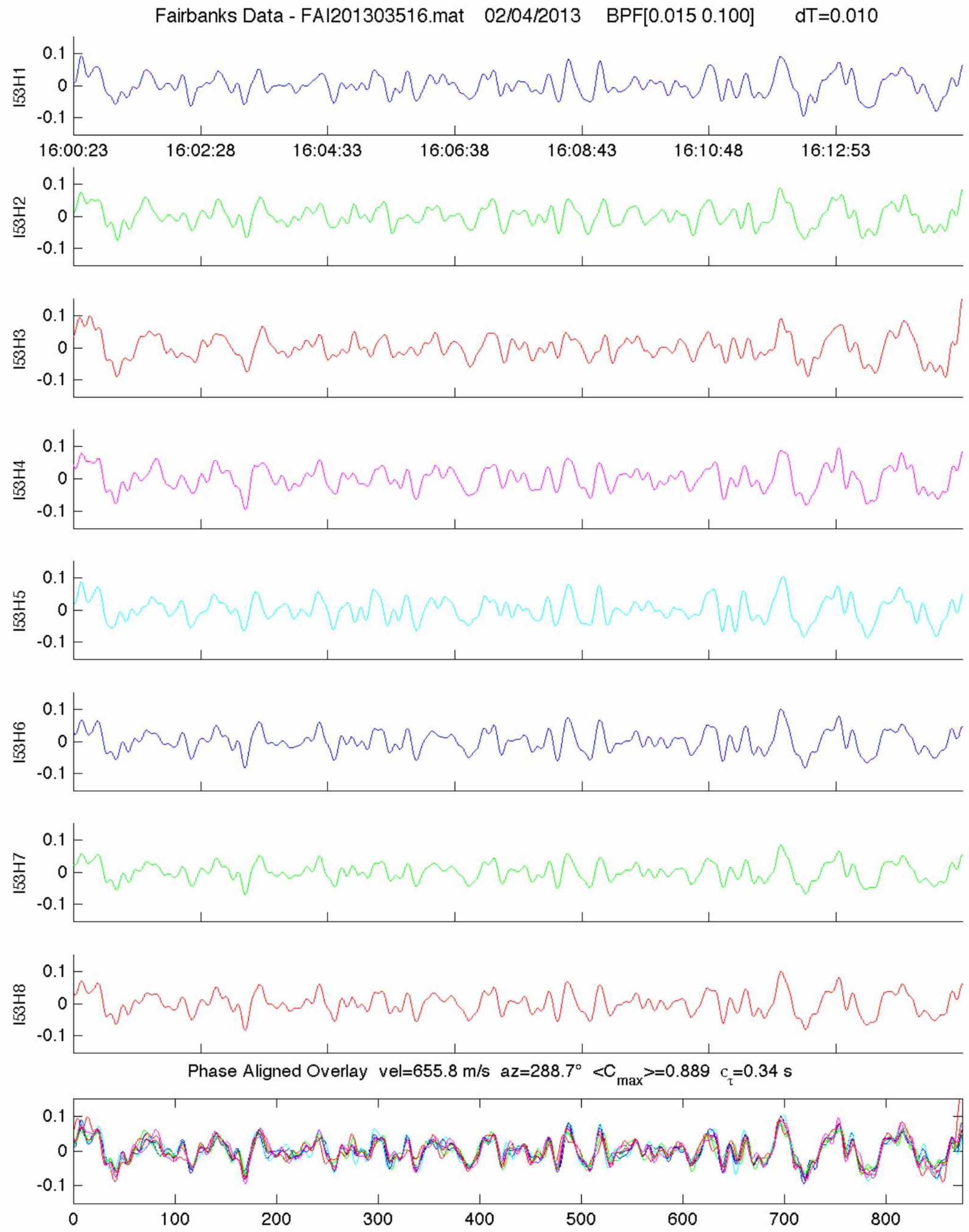

Fig 2.10. Pressure time series during MAW. The time series for each of the eight sensors and the phase-aligned overlay a given over approximately 15 minutes of active mountain associated waves. The data is band passed filtered to 0.015-0.1 Hz. The waveforms are irregular but highly coherent.

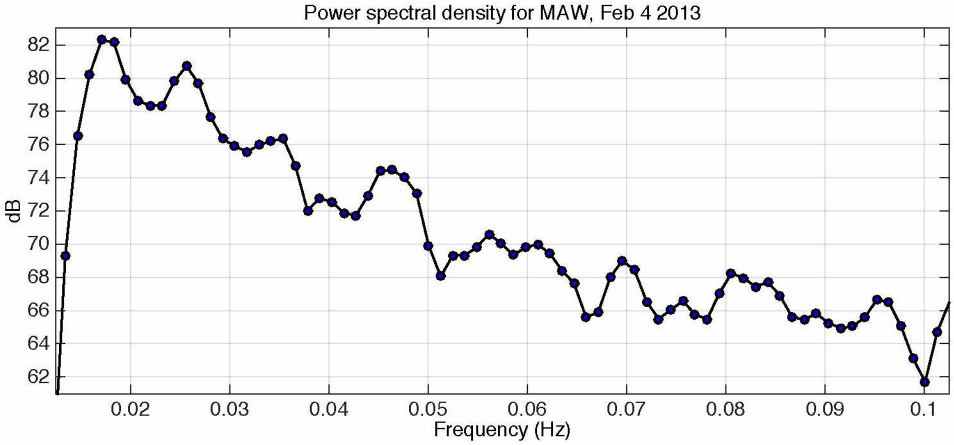

Fig 2.11. Power spectral density profile for MAW event of Feb 4, 2013. The PSD was generated using Welch's method with a Hamming window of 500 seconds and 50% overlap between windows. One hour of data was considered beginning 13:00 UT.

2.8 Auroral Infrasound Waves – Acoustic Signature

Auroral infrasound waves are best identified as very low frequency acoustic waves that occur during periods of active aurora or related geomagnetic storms. These events can include both short duration impulsive signals associated with auroral forms moving across the overhead zenith, as well as sustained signals that persist continuously over a period of hours.

Generally speaking, auroral infrasound is characterized by extremely high trace velocity. Since specific auroral events have been linked to subsequent infrasound signals, the time of delay allows an estimate of the source altitude as between 90 and 110 km. Analysis of the ray tracings presented above, alongside more sophisticated propagation studies, suggest that for a source at these altitudes signals with a take-off greater than about 40^0 will be refracted away. Basic trigonometry then suggests that absent strong winds only signals generated within about 125 km from the overhead zenith can usually be observed at a given station. The very high trace velocities associated with auroral infrasound result from this basic observation.

Like the MAW, auroral infrasound is composed of irregular waveforms with the greatest energy density in the spectral region just above the Brunt-Väisälä frequency. Signal detection of auroral infrasound has been empirically studied since the 1960's; it is usually effective to focus detection algorithms on the pass band from 0.015 – 0.1 Hz (between the Brunt-Väisälä and the microbarom surge).

Initial studies of auroral infrasound focused on impulsive signals generated when auroral electrojet currents crossed the overhead zenith at velocities comparable to the sound speed [36]. Recently, improving sensor technology alongside greater computational efficiency demonstrated that these impulsive signals frequently appear imbedded in lower amplitude, temporally persistent GAIW's that often persist throughout the breakup phase of a geomagnetic storm.

Fig 2.12 displays a detection summary observed during a typical GAIW event observed on JD 76 2013. The GAIW active time period is easily identified running from 14.5 to 19 hr UT. GAIW exhibits trace velocities usually averaging 0.7 km/s or higher. The variance in the trace velocities is often substantial, commensurate with the considerable uncertainties associated with a source near the overhead zenith. It is interesting to note that the variance in back azimuth estimates is typically much lower. At I53US the back azimuth measurements tend to the north, which is consistent with a source centered in the auroral oval, as it is most often over northern to central Alaska. Similarly I55US logs back azimuth measurements of GAIW tending to the south.

A pressure time series of the GAIW event recorded JD 75 2013 is presented in Fig 2.13. The waveforms are irregular with intermittent higher amplitude periods appearing amidst a background of low amplitude, highly coherent perturbations. Much like MAW, the spectrum of GAIW decays exponentially with increasing frequency in the pass-band of interest. Again, the PSD exhibits no particular peaks or troughs, although the general shape is reminiscent of turbulent wind noise (indeed, speeding up the data to audible frequencies, GAIW is heard to sound very similar to wind noise on a microphone). Fig 2.14 displays a PSD estimate of the GAIW event of JD 76 2013. The PSD was generated using Welch's method with a Hamming window of 500 seconds and 50% overlap between windows. The data has been band pass filtered to 0.015 – 0.1 HZ. One hour of data was considered beginning 15:00 UT.

Lee has argued that computational measures may be installed to disambiguate MAW from GAIW based on signal trace velocity, spectral characteristics, and statistical considerations such as MCCM and Fisher F-statistics [13, 37, 38]. In point of practice, however, it is difficult to quantify the effects that simultaneous MAW occurrences may have on studies involving GAIW signal detection and waveforms. Our group utilizes a variety of other diagnostic instruments to isolate GAIW events and determine concurrent phenomena that contribute to its generation. The following chapter is devoted to the data analysis methods and physical interpretations of these supporting instruments.

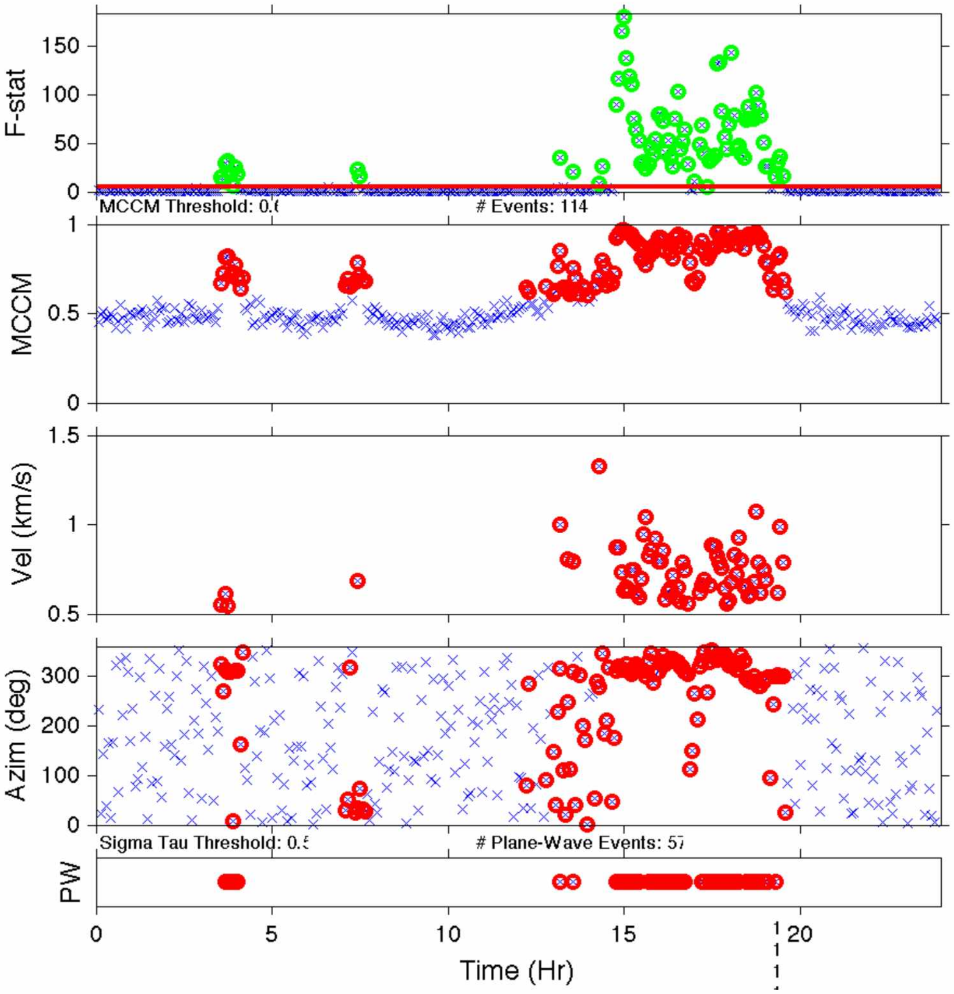

Fig 2.12. 24 hour summary of signal detections including a GAIW event beginning JD 76 2013. . The Fisher F-statistic, mean of the cross correlation maxima, trace velocity, and back azimuth estimates are presented for 24 hours of data.The GAIW event occurs between 14.5 and 19 hours UT, during which time HTV signals were received with trace velocities averaging ~ 0.75 km/s.

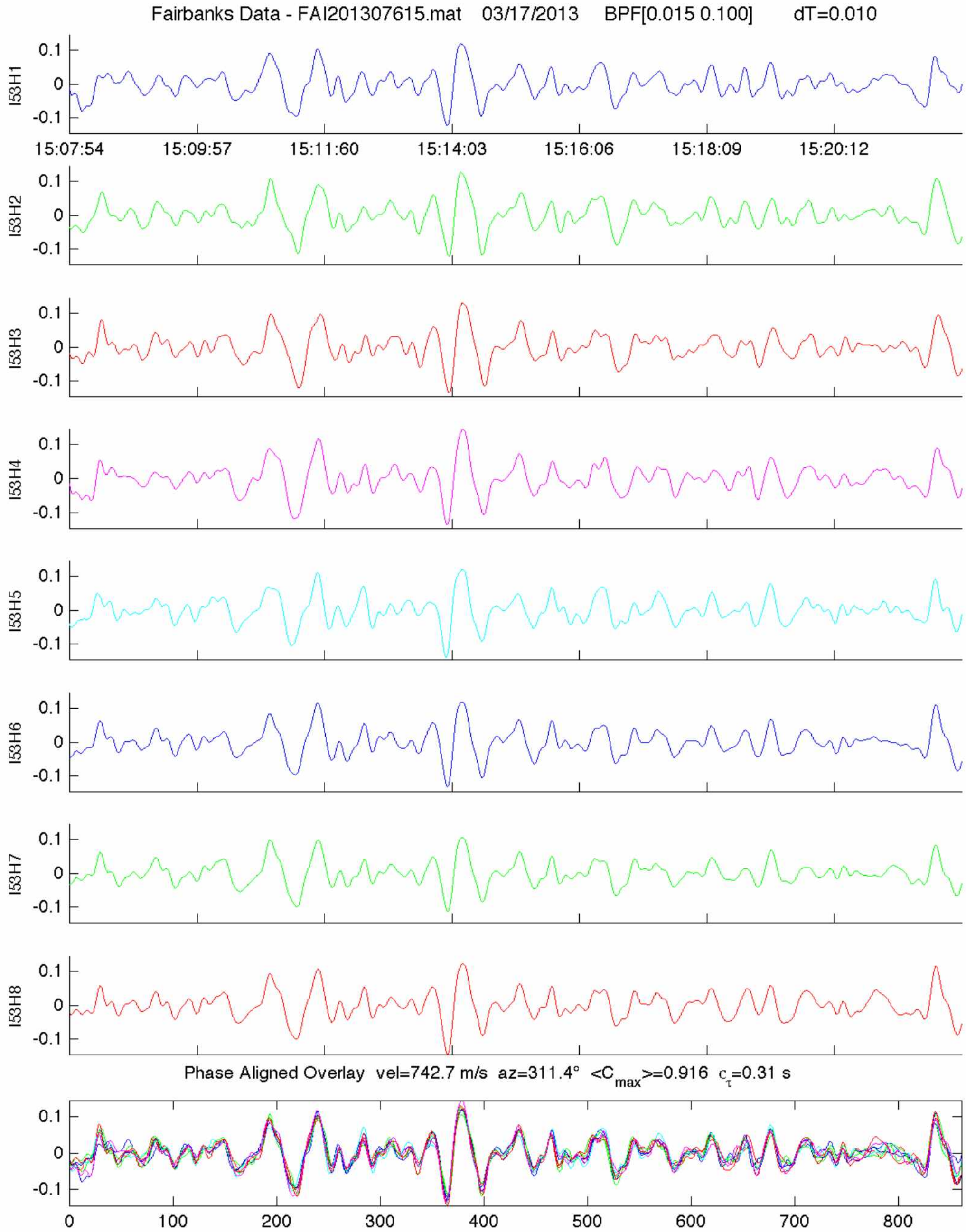

Fig. 2.13. Pressure time during GAIW event of JD 76 2013. The time series for each of the eight sensors and the phase aligned overay are given for approximately 15 minutes. The wave forms are irregular but very coherent across the array.

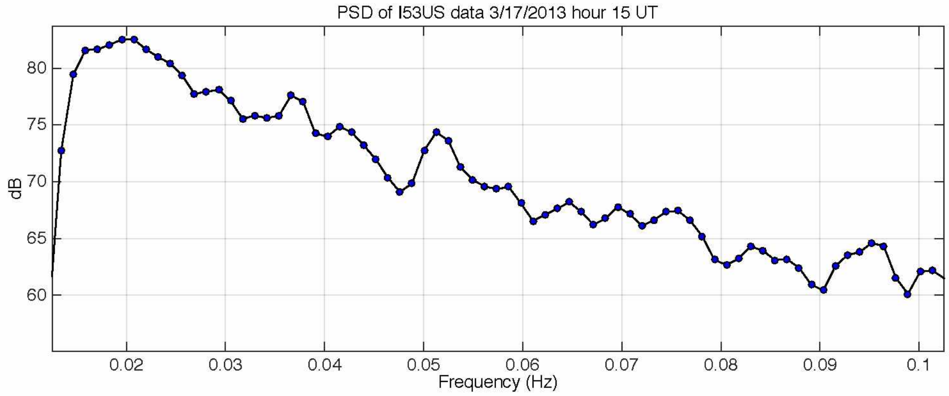

Fig 2.14. Power spectral density profile for GAIW event of JD 75 2013. The PSD was generated using Welch's method with a Hamming window of 500 seconds and 50% overlap between windows. The data has been band pass filtered to 0.015 – 0.1 HZ. One hour of data was considered beginning 15:00 UT.

Chapter 3

Diagnostic Instruments and Methods

3.1 Poker Flat Imaging Riometer

Several instruments, aside from the microphone arrays, are considered as diagnostic tools for auroral infrasound. Here we describe the physical principles, material design, and data analysis developed by our group for the Poker Flat Imaging Riometer [PFIR].

Riometer is an abbreviation for a relative ionospheric opacity meter. The apparatus itself is essentially a radio telescope receptive to high frequency radio radiation. In the case of the PFIR the receiver is a 16x16 array of antennae that utilize phasing techniques to form beams. The antennae are sensitive to electromagnetic radiation in a narrow pass band centered about 38 MHz. Incident radiation is measured as voltage, and each antenna is equipped with a small pre-amplifier to boost the signal. The data are compiled and stored in an on-site central vault that houses the necessary memory and data processing chips to perform the phasing and calibration routines. The riometer was originally developed at the UAF Geophysical Institute in 1956 by H. Leinbach and his team [39].

It was observed by the 1940's that Earth is immersed in a continuous microwave radiation field (A. Penzias and R. Wilson shared a nobel prize for long standing investigations into this in 1978) [40]. Subsequent observations made by orbiting radio telescopes have shown this cosmic background radiation [CBR] to exhibit a blackbody radiation spectrum with peak intensity around 160 GHz. However, Earth's atmosphere proves to be very efficient at absorbing radiation in these wavelengths, and very little CBR is received by a ground-based sensor above frequencies of around 100 MHz. Conversely, at frequencies below ~0.5 MHz the CBR suffers very little attenuation as it traverses Earth's atmosphere. In the intervening spectrum, particularly in the approximate range of 15 – 60 MHz, the atmospheric attenuation is very nearly linear with respect to frequency. The riometer seeks to monitor deviations in the attenuation of the CBR.

Ionospheric absorption of radio waves is related to the conductivity of the plasmas. For simplicity, we consider the geometry described in Fig 3.1. Specifically, the geomagnetic field is taken as identically vertical (a good approximation at high latitudes) while the **E** field is left arbitrary.

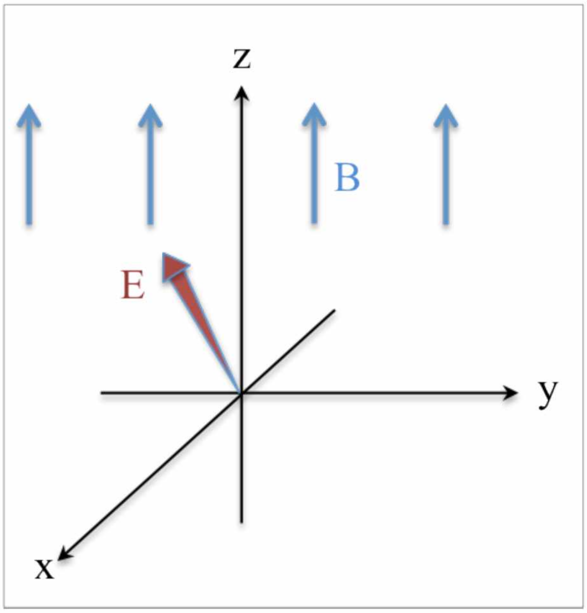

*Fig 3.1 The geometry of the model ionosphere used in mathematical development. The vertical **B** field is a good approximation at latitudes where the auroral oval forms. The **E** field is left arbitrary to account for diurnal and other variations.*

The force balance equation for a plasma composed of ion species k with density N_k immersed in an electric and magnetic field is given by

$$e\vec{E} + e(\vec{v} \times \vec{B}) = m\nu\vec{v} \, , \tag{3.1}$$

where e is the fundamental electron charge and ν is the ion collision frequency. According to the geometry above we arrive at the component-wise system:

$$\begin{aligned} m\nu v_x &= eE_x + ev_yB_z \\ m\nu v_y &= eE_y + ev_xB_z \\ m\nu v_z &= eE_z, \end{aligned} \tag{3.2}$$

which can be solved for the components of velocity to yield

$$\begin{aligned} v_x &= \left[\frac{\left(\frac{e}{m}\right)\nu}{\nu^2 + \omega_H^2}\right]E_z + \left[\frac{\left(\frac{e}{m}\right)\omega_H}{\nu^2 + \omega_H^2}\right]E_y \\ v_y &= -\left[\frac{\left(\frac{e}{m}\right)\omega_H}{\nu^2 + \omega_H^2}\right]E_x + \left[\frac{\left(\frac{e}{m}\right)\nu}{\nu^2 + \omega_H^2}\right]E_z \\ v_z &= \left[\frac{e}{m\nu}\right]E_z \end{aligned} \tag{3.3}$$

where we have defined a characteristic frequency $\omega_H = eB/m$. In general, current can be defined in terms of ion (or electron) density as

$$\vec{j} = \sum_k N_k e_k \vec{v}_k \quad , \tag{3.4}$$

where N_k is the number density. For a single ion species and corresponding electron density we can utilize the estimates of velocity given by Eqn. (3.3) to make explicit estimates of the components of current

$$\begin{aligned} j_x &= \left[\frac{\varepsilon_0\omega_i^2 + \nu_i}{\nu_i^2 + \omega_{Hi}^2} + \frac{\varepsilon_0\omega_e^2\nu_e^2}{\nu_e^2 + \omega_{He}^2}\right]E_x + \left[\frac{\varepsilon_0\omega_i^2\omega_{Hi}^2}{\nu_i^2 + \omega_{Hi}^2} - \frac{\varepsilon_0\omega_e^2\omega_{He}^2}{\nu_e^2 + \omega_{He}^2}\right]E_y \\ j_y &= -\left[\frac{\varepsilon_0\omega_i^2\omega_{Hi}^2}{\nu_i^2 + \omega_{Hi}^2} - \frac{\varepsilon_0\omega_e^2\omega_{He}^2}{\nu_e^2 + \omega_{He}^2}\right]E_x + \left[\frac{\varepsilon_0\omega_i^2 + \nu_i}{\nu_i^2 + \omega_{Hi}^2} + \frac{\varepsilon_0\omega_e^2\nu_e^2}{\nu_e^2 + \omega_{He}^2}\right]E_y \; . \\ j_z &= \left[\frac{\varepsilon_0\omega_i^2}{\nu_i} + \frac{\varepsilon_0\omega_e^2}{\nu_e}\right]E_z \end{aligned} \tag{3.5}$$

Here we have noted that $\omega_k^2 = N_k e^2/m_k \varepsilon_0$ defines the gyro frequency for species k. It is customary to write the relationship described by Eq. (3.5) in the succinct form suggestive of a generalization of Ohm's law $\vec{j} = \bar{\sigma} \cdot \vec{E}$

$$\begin{pmatrix} j_x \\ j_y \\ j_z \end{pmatrix} = \begin{pmatrix} \sigma_P & -\sigma_H & 0 \\ \sigma_H & \sigma_P & 0 \\ 0 & 0 & \sigma_0 \end{pmatrix} \begin{pmatrix} E_x \\ E_y \\ E_z \end{pmatrix} . \tag{3.6}$$

The conductivities σ_P, σ_H, and σ_0 are given explicitly by the coefficients in equations (3.5) and are termed the Pederson, Hall, and Parallel conductivity respectively. The Hall and, in particular, the Pederson conductivities are important parameters in models of AIW generation. The mathematical development of pressure fields resulting from auroral electrojets typically begins with the hydrodynamic equations relating neutral species number density to the pressure. Specifically, for the neutral species with number density n we consider conservation

$$\frac{dn}{dt} + n\nabla \cdot \vec{u} = 0, \tag{3.7}$$

momentum,

$$mn\left(\frac{d\vec{u}}{dt}\right) - mn\vec{g} + \nabla p = \frac{\vec{j} \times \vec{B}}{c}, \tag{3.8}$$

and pressure fluctuations due to Joule heating

$$\frac{dp}{dt} - \gamma kT\frac{dn}{dt} = (\gamma - 1)\vec{j} \cdot E . \tag{3.9}$$

Clearly, ionospheric conductivity plays a critical role in these equations.

The relationship between ionospheric conductivity and opacity is a complicated one. Here the relationship is discussed a little, but for complete development of the pertinent equations the reader is referred to Yeh and Lui [16]. For a radio wave traversing ionospheric plasmas the refractive index is generally modeled by the Appleton-Hartree formula [16]:

$$n^2 = 1 - \frac{X}{1 - iZ - \frac{1}{2}\left(\frac{Y^2 \sin^2\theta}{1 - X - iZ}\right) \pm \frac{1}{1 - X - iZ}\left(\frac{1}{4}Y^4 \sin^4\theta + Y^2 \cos^2\theta\left[1 - X - iZ\right]^2\right)^{1/2}} \tag{3.10}$$

$$X = \left(\frac{\omega_0}{\omega}\right)^2; \quad Y = \frac{\omega_H}{\omega}; \quad Z = \frac{\nu}{\omega}; \quad \omega_0 = \sqrt{\frac{Ne^2}{\varepsilon_0 m}}; \qquad \omega_H = \frac{B_0 e}{m}$$

Given a complex index of refraction *n*, the wave attenuation coefficient *k* in the medium is related to the complex component of *n* via *k = imag(n)*ω/c*. In point of practice, many of these parameters are difficult to monitor and remain unknown at a given region in time and space of the ionosphere. However, typical values may be inserted to give estimations of how atmospheric absorption and conductivity are related. Taking, for instance, constant values as quoted by the NRL Plasma Formulary for temperature and geomagnetic field strength, letting NO^+ be the dominant ion species with number density equal to the electron density, and approximating relationships between the number density and collision frequency the total conductivity and absorption coefficient may both be calculated as a function of electron number density [41]. Fig. 3.2 displays a plot of the radio wave absorption coefficient, shown as a blue curve, and total ionospheric conductivity displayed as a red curve, as a function of electron number density. While the absolute values of these variables differ by order of magnitude, the shapes of the two curves are qualitatively very similar. The upshot is that while an exact, quantitative knowledge of ionospheric currents is not given by a riometer measurement, horizontal regions of heightened conductivity are clearly defined.

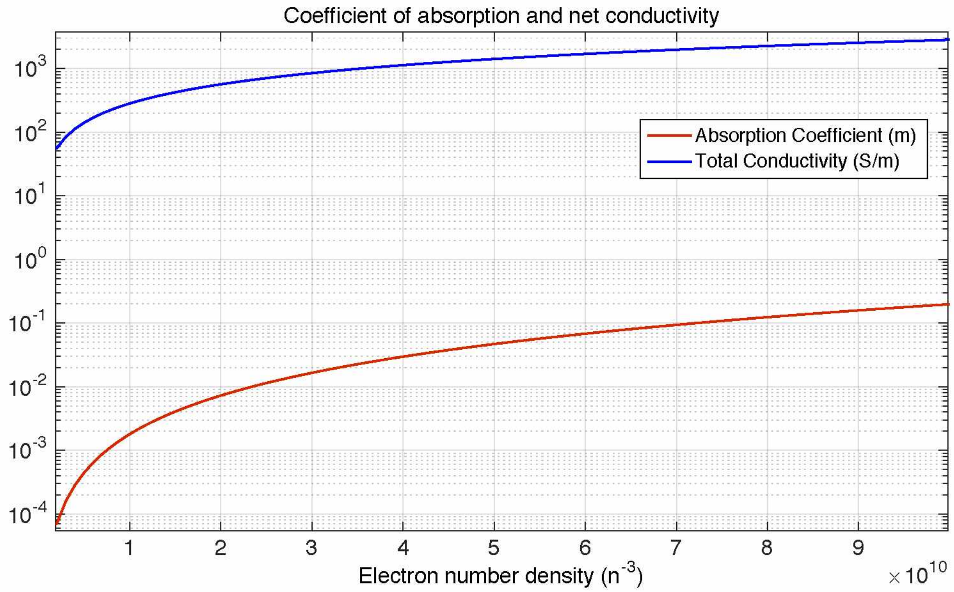

Fig 3.2 Radio wave absorption coefficient and total ionospheric conductivity as a function of electron number density.

Data from the PFIR is given in voltage at a sampling rate of 1Hz for each of the 256 independent beams. A periodic pulse is additionally present as part of the system's internal calibration mechanism. The pulse is represented as either an approximately zero or unphysically high value that usually appears quasi periodically several times per hour. Since this calibration pulse occasionally varies from predictable periodicity the calibration events must be individually identified and removed from the data. This may be accomplished by, for instance, linear interpolation or other methods. Fig 3.3 displays a typical plot of the raw data recorded by one element of the PFIR array. The periodic vertical structures are the calibration pulses; they generally log values much higher than the ambient voltages or very near zero.

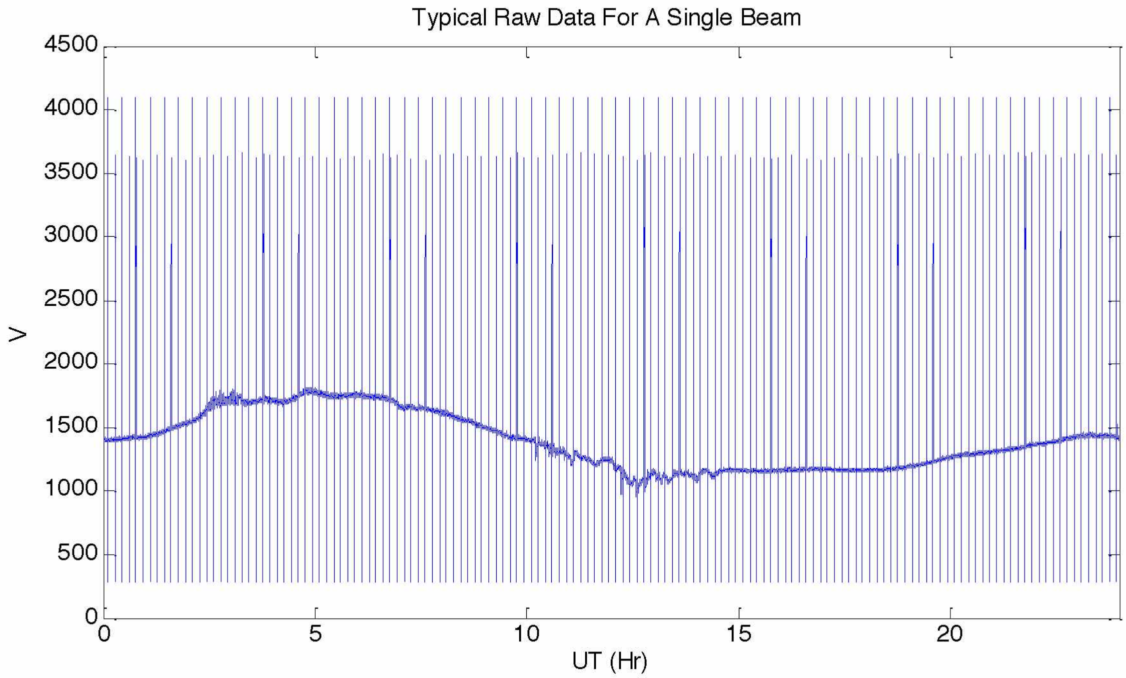

Fig 3.3. An example of the raw data collected for one of the 256 beams of the PFIR. The values around zero and 4000 V are artifacts of the instrument calibration system and must be judiciously removed for analysis.

While the riometer is continuously sampling at 1 Hz, the physical processes that we wish to examine often take place over time scales of hundreds or even thousands of seconds. We usually down-sample the data to 30-second averages and remove the calibration pulse during the decimation process. This routine serves both as a low-pass filter to target the low frequency events as well as providing the additional benefit of greatly reducing the computations required to process the 22,118,400 samples recorded each day of PFIR's operation. Fig 3.4 displays the same data plotted in Fig 3.3 following the decimation and pulse removal process. It should also be noted that in Fig 3.4 a conversion to sidereal time has been performed.

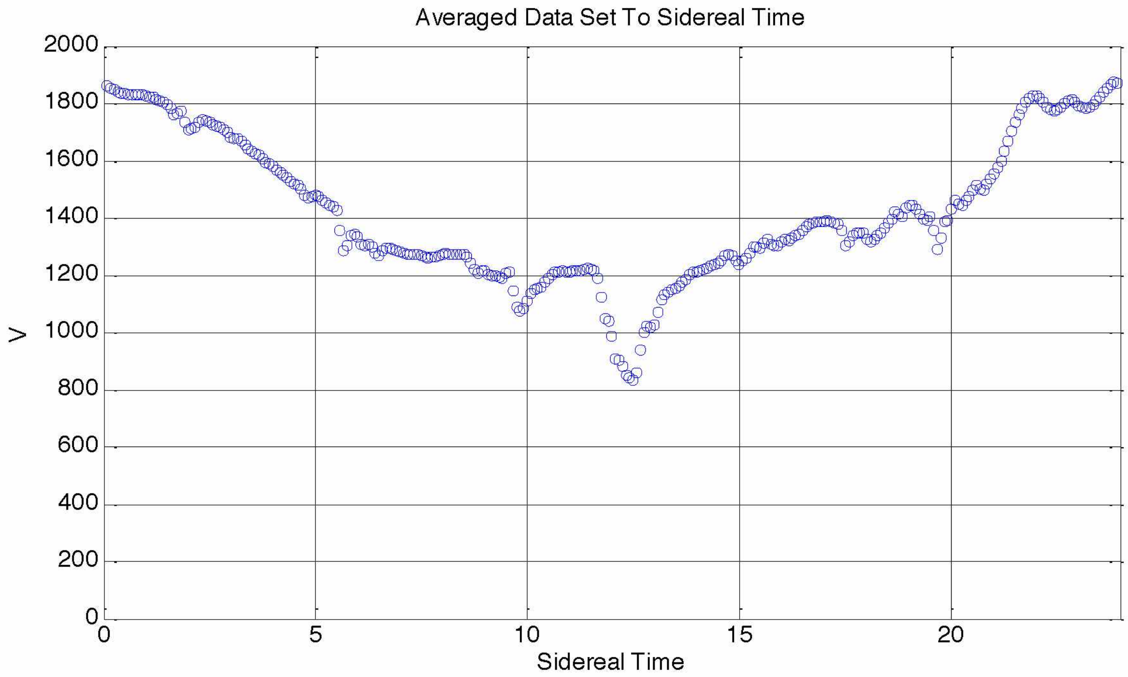

Fig 3.4. PFIR data after down-sampling and removal of calibration pulses. The data is for a single beam directed near the overhead zenith. A conversion to sidereal time has also been made.

When the raw data has been processed to remove the calibration pulses an algorithm may be developed to compute the expected value of received radiation for unperturbed times. The time series of the unperturbed voltage values is referred to as the quiet day curve [QDC]. There seems to be little consensus in the community for the best method of generating the QDC. Our group developed and employs the following algorithm, with detailed descriptions and justifications provided below. First, a conversion from universal to sidereal time is made via the standard mathematical transformation. This conversion is required as the QDC reflects the astronomical features. The data is then grouped into a two dimensional histogram for time and voltage. The mode, or most frequently hit bin, of the histogram values for the thirty days surrounding the date in question is then taken as the quiet day value. Finally, a low-pass filter is applied.

In developing the histogram for generating the QDC there is considerable freedom to choose the appropriate values for voltage and time windows. After a trial and error period we have settled on 5 volts per bin and 30 seconds per time window as effective values. Fig 3.5 displays a typical two-dimensional histogram of samples recorded by a single element of the PFIR array. Here, 30 consecutive days of records are used to generate the histogram with the color bar denoting the number of times the recorded value fell into a given bin. Inspection of Fig. 3.5 reveals that after conversion to sidereal time a daily pattern of voltage values becomes apparent. For a given time window the mode of voltages is taken as the quiet day value. Fig 3.6 gives a plot of the mode of the voltages as found by the two-dimensional histogram depicted in Fig. 3.5.

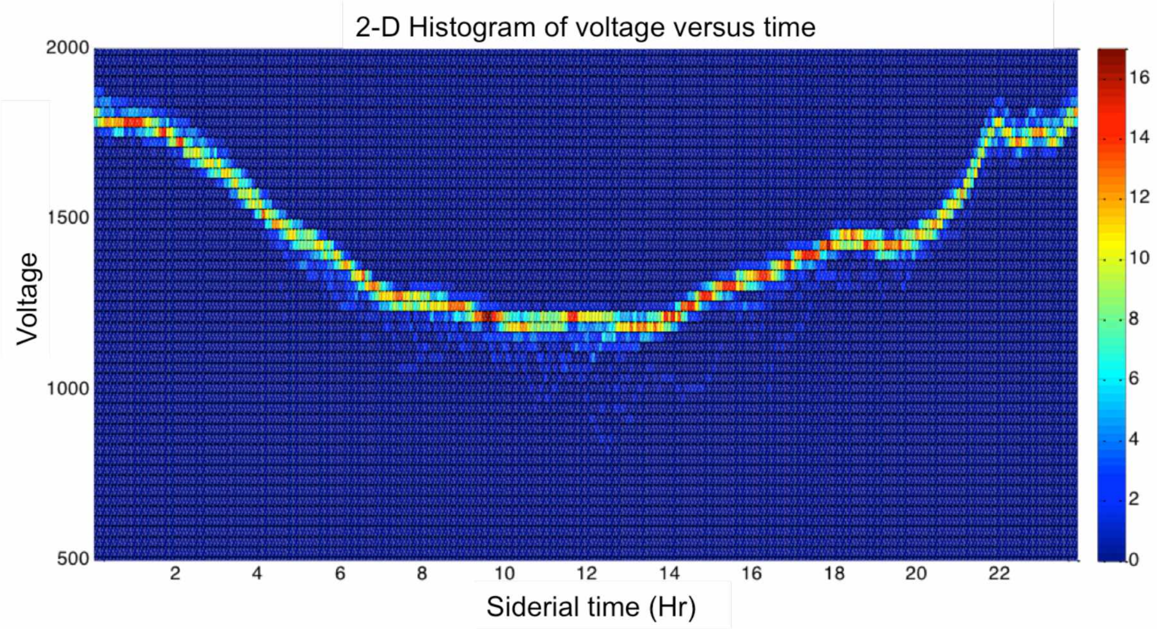

Fig. 3.5. Two-dimensional histogram of voltage versus time for 30 days of riometer data for a given beam. The color axis denotes the number of times a given value was found.

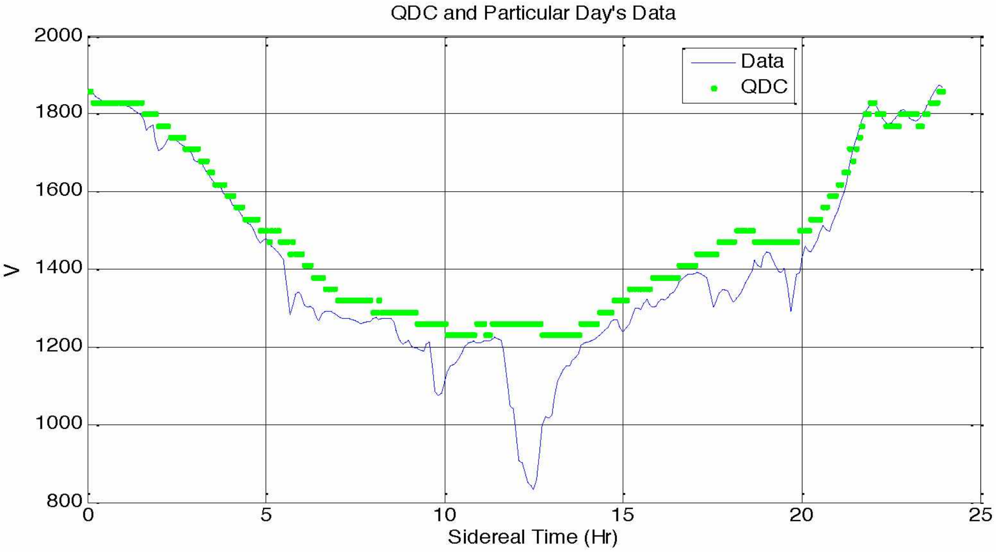

Fig. 3.6. Example of a PFIR quiet day curve before smoothing. The mode of the voltages over 30 days has been taken as the un-smoothed QDC. For comparison, a geomagnetically active voltage value is shown in blue.

The final step in generation of the quiet day curve is smoothing of the curve via a Fourier transform low-pass filter. The justification for such a filter comes from considerations of time scales. While the Earth is continuously impinged upon by CBR, the received radiation is more intense when certain stars that are emitters (often termed radio stars) fall within the solid angle subtended by the beam. Since the angle each beam subtends is roughly 6^0, it takes a radio star or any other astronomical phenomenon about 24 minutes to traverse the beam. As such, we set our filter to remove features occurring on time scales of less than 15 minutes. Fig 3.7 depicts the QDC plotted in Fig 3.6 after application of the Fourier transform low-pass filter. This is the final version of the QDC for the array element considered and corresponds to the QDC for the particular day of data plotted in Fig 3.3. The data plotted in Fig 3.4 are overlaid against the QDC in Fig 3.7 for comparison.

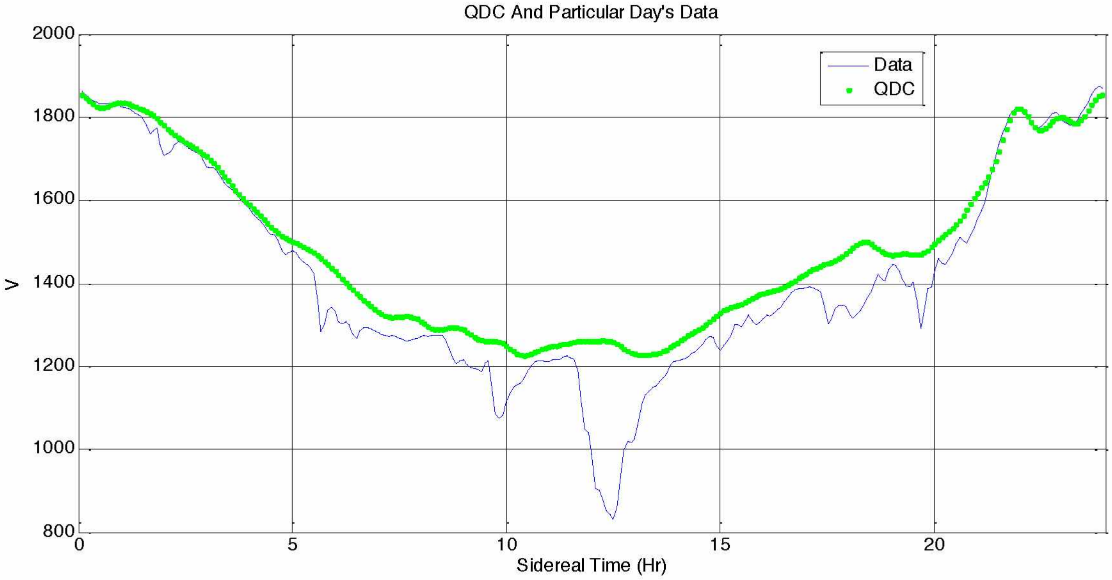

Fig 3.7. Example of a PFIR quiet day curve following smoothing. The data for a geomagnetically active day are shown in blue.

Once the QDC has been completed we may compare it against the received voltage to generate the CNA data. CNA is typically presented in decibels. While theoretically CNA values can exceed 10 or more decibels, in point of practice the PFIR rarely records values higher than 2 decibels. Fig 3.8 displays the CNA values in dB calculated from the ratio of QDC to daily values displayed in the Fig 3.7. The CNA time series, which is the desired parameter available from the riometer, is now complete for a given array element.

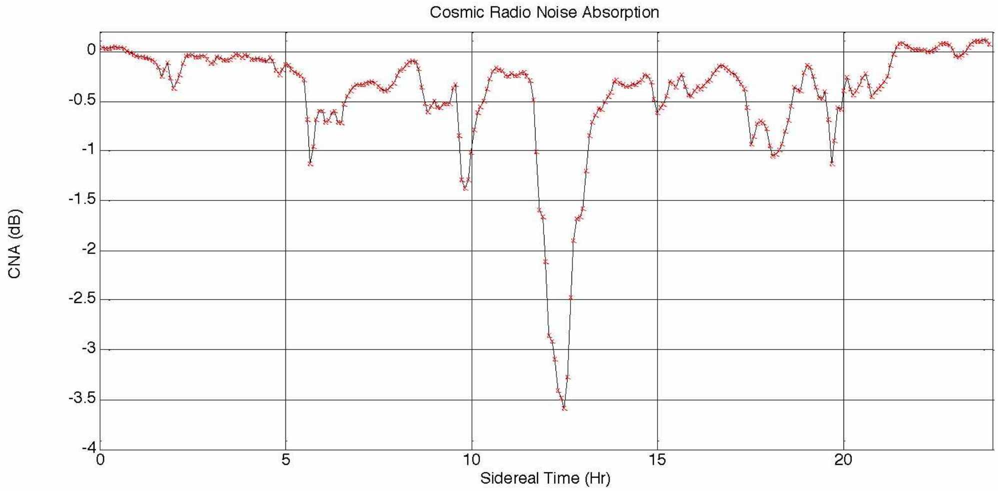

Fig 3.8. The time series of cosmic noise absorption id dB as calculated from the ratio of QDC to the daily values (blue and green curves in Fig 3.7).

PFIR's phasing system allows for a CNA map of the sky covering an overhead area of roughly 200 km side length with an overhead resolution of approximately 11 to 30 km. Away from the overhead zenith the resolution becomes increasingly poor; the 48 beams recording furthest from the overhead zenith are considered to be unreliable and are generally excluded. The grid is oriented toward magnetic north (or what was magnetic north at the time of installation), although for comparison with other instruments we prefer to present the data in terms of true north orientation. Fig 3.9 displays a typical map of CNA values recorded by the PFIR during a geomagnetically active time. High conductivity regions are shown in blue. The conversion from magnetic to true North accounts for the skewed rotation of the grid in Fig 3.9. The stretching of the beams away from the overhead zenith is a geometrical effect, the area of the ionosphere swept over by a beam making a 7^0 sweep in both the North and South directions increases non-linearly with distance from the overhead zenith. A final geometric correction is made to account for the increased distance travelled through the absorbing region of the atmosphere by CBR signals traversing at greater angles (this correction amounts to a factor of the secant of the angle).

Another point to consider is that the initial image generated is oriented for an observer facing north and looking up. This means that south is at the top of the image as it is in Fig 3.9. For comparison to acoustic data it is generally desirable to perform a reflection such that north is at the top of the image (the "looking down" perspective). Following Fig. 3.9 this reflection has been performed on all riometer data and is discussed no further. For more detail regarding the PFIR's instrumentation see Murayama et al [42].

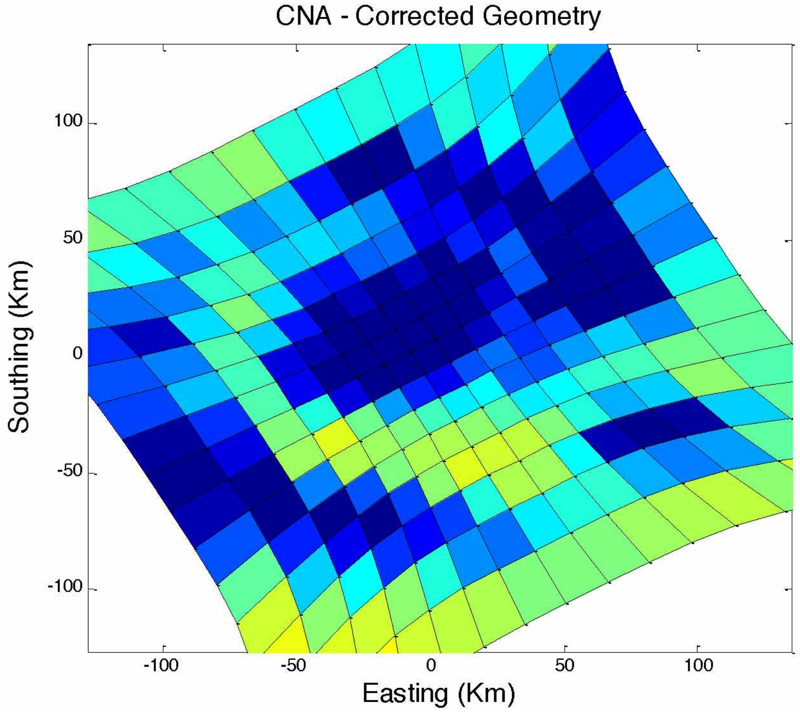

Fig 3.9. Map of CNA values gathered by the PFIR during a geomagnetically active time. Areas of intense CNA are shaded blue.

3.2 Geophysical Institute Magnetometer Array

The geophysical institute maintains an extensive array of magnetometers. In Alaska, the Geophysical Institute Magnetometer Array [GIMA] is currently composed of 12 sensors distributed in a roughly North to South chain stretching from near the arctic ocean at Arctic Village to the southern coastal city of Homer. For our study, we generally rely on the so called CIGO array element located in College, Alaska on the UAF campus, as it lies only meters from one of the I53US array elements and therefore gives the most nearby observations for comparison. For times when the CIGO magnetometer wasn't active we utilize the magnetometer located at the Poker Flat research area some 20 miles to the North and East. The instruments employed in the array are tri-axial fluxgate magnetometers manufactured by Narod Geophysics of Canada [43]. The three instrument cores are wrapped in copper wire and housed in a ceramic block. The block is enclosed in an aluminum chassis manufactured at the geophysical institute alongside a preamplifier. An S-100 computer serves as the digitizer; it utilizes internal calibration schemes to convert voltages to units of nT. The data are collected at a sampling rate of 1 Hz.

The geometry associated with the three field components is the H, D, and Z system often used to report variations in Earth's geomagnetic field. During geomagnetically active times perturbations to the field are frequently on the order of hundreds of nanoTesla (nT), with variations exceeding 1000 nT infrequent but sometimes reported. Fig 3.10 is a cartoon image designed to help visualize the components of the **B** field as reported by the GIMA sensors. The red arrows represent the arbitrary **B** vector considered and its projection into the horizontal plane, usually referred to as the total horizontal disturbance vector [THD]. The vertical axis points downward normal to the Earth's surface, and the horizontal axes point to the North and East.

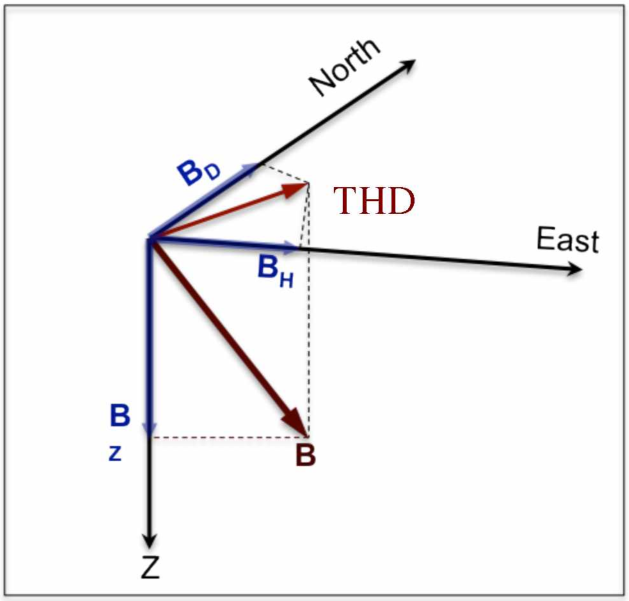

Fig. 3.10. Geometry of the field components as measured by the GIMA sensors. The vector projection onto the horizontal plane is referred to as the total horizontal disturbance vector [THD].

Much has been written about the evolution of the magnetic field fluctuations during geomagnetic storms and sub-storms [44 - 47, e.g.]. Here a very brief summary is presented. During the initial build-stage of a storm the H component shows a moderate increase that may last several hours and is often accompanied by small, irregular perturbations in the D and Z components. Later, the H component tends to cross over to negative with absolute values far exceeding those of the buildup phase. The D and Z components may exhibit large, irregular perturbations during this part of the storm and often move from positive to negative multiple times. These perturbations may continue through the recovery phase but with decreasing intensity, while the H component gradually returns to its quiet day value. Fig 3.11 gives a plot of the **B** field components recorded by the CIGO magnetometer over 24 hours in which a geomagnetic substorm was observed. Usually when displaying the three field components the plots are translated to bring the values closer together for efficient display with the mean values of the components explicitly noted. The substorm appears as the irregular field perturbations last from ~7 - ~15 UT.

There are a variety of features within the field fluctuations during a geomagnetic storm that are consistently associated with certain magnetospheric or ionospheric conditions. These features, referred to here as geomagnetic micropulsations, have been described in some detail [45]. Of particular interest to this study are the irregular micropulsations that are known to arise at high latitudes during geomagnetically active times, generally labeled pi1 (pulse irregular) and pi2 type pulsations. The interested reader may refer to the cited works for a comprehensive review of the subject.

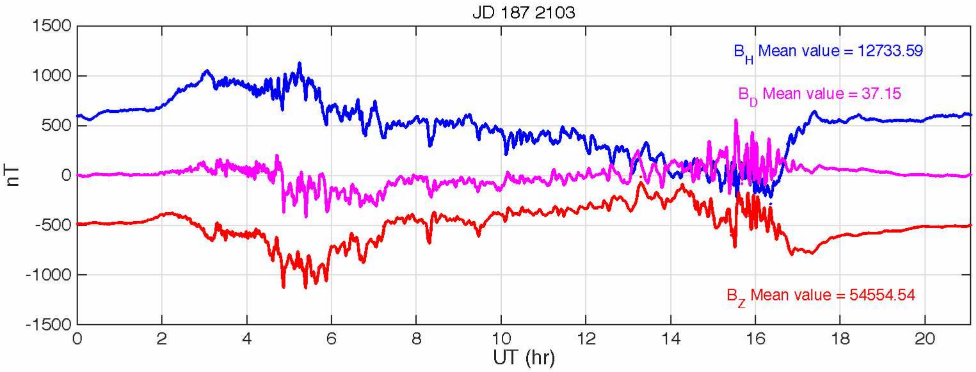

Fig. 3.11. Plot of magnetometer data for a geomagneticly active day. The data is presented in nT with the mean values appearing on the right.

3.3 Poker Flat All-Sky Camera

In discussing GAIW we will also sometimes refer to the direct visual observations of auroral luminosity provided by photographs. Optical sensors at Poker Flat have maintained consistent access to luminosity measurements over a wide-angle range of the sky sampled at 1 Hz for most winter nights. Over the years of GAIW observation at College, Alaska, the optical equipment available has become increasingly sophisticated. Fig. 3.12 displays a Poker Flat All-Sky Camera [PFASC] image taken during a period of active aurora in 2005. While the image doesn't have a color scale it may still be used to calculate total auroral luminosity as well as track dynamic regions of heightened luminosity over time.

Fig 3.12. Example black and white all sky camera image. This image represents a traditional black and white all sky image which may be utilized to calculate total auroral luminosity.

The current camera that is utilized is a KEO Scientific Sentry model with a 6-position filter wheel. The optical components are custom designed with an f/# of about 1. A telecentric design allows for the use of narrow band-pass filters to image specific auroral emissions. The detector is an electron multiplying CCD (EMCCD) from Andor Corporation. The camera is in a three-filter mode, which includes the 427.8 N2+ first negative emission, 557.7 nm atomic oxygen green-line, and 630.0 nm atomic oxygen red-line emissions. A set of three images takes about 13 seconds to complete and defines the imaging cadence [48].

It is often instructive to remove a spatial dimension when viewing PFASC (or PFIR) data in order to generate a two dimensional image suitable for print. Traditionally this is accomplished by taking a North-South or East-West cut through the overhead zenith of the luminosity values at each time. The result is referred to as a keogram, and provides a succinct history of the visible aurora as it passed over, for instance, the North-South cut. Directivity of the auroral forms is maintained as the slope in the vertical structures. In figure 3.13 a typical keogram is displayed (example taken is from 25 December 2013). The keogram has been generated from images taken by the PFASC; the vertical structures in the image suggest overhead crossings of heightened luminosity auroral forms.

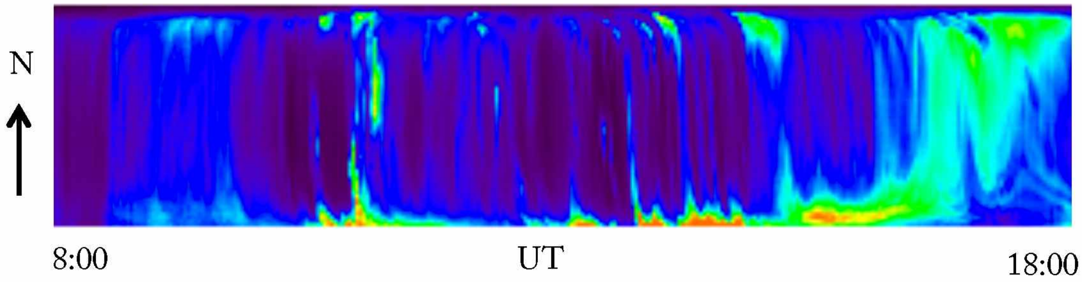

Fig 3.13. Example keogram of optical emissions during a geomagnetic storm. This was recorded by the PFASC; the intense greens and oranges show regions of high luminosity.

The PFASC provides considerable information regarding energy distribution, collision rates, plasma densities, and dynamic evolution in auroral forms. The principal factors that limit its application in the following discussions are its sensitivity to weather conditions and inoperability during summer months when sunlight dominates the sky throughout the night. It is unfortunate that most of the GAIW events that we consider occurred when all-sky camera imaging was not available. Nevertheless, the PFASC and other all sky cameras historically located in the auroral zone have shown the existence of pulsating aurora and other auroral features during periods of active GAIW, and as such should be included in any discussion of GAIW generation.

Each of the diagnostic instruments described above provide unique but limited information about historic ionospheric conditions. Chapter 4 presents an effort to describe and quantify the conditions observed on each of these instruments during GAIW events.

Chapter 4

GAIW in Space and Time

In this chapter we present a detailed review of 63 confirmed GAIW events stretching back to 2003. The data considered, encompassing over a decade of collection, represent a consistent record of GAIW events over an entire 11-year solar cycle. Such a long-term, continuous record of infrasonic and other data has not historically been available for discussions of auroral infrasound.

4.1 Example and Conditions for Inclusion in the Study

Throughout this chapter we present both quantitative statistical analysis and qualitative observations of the data associated with GAIW. Each GAIW event identified is analyzed utilizing whatever diagnostic equipment is available (ie. GIMA, PFIR, PFASC). The events chosen for the study are effectively cherry picked as no automated method was adopted as an identifying implement. However, it is instructive to consider a body of "good" examples in an effort to characterize and quantify the conditions observed during active GAIW. The results may then be applied both to implement or improve upon automated methods as well as constrict the possible mechanisms of generation. Before discussing the details of conditions for an event to be included in the study, it is instructive to consider an example.

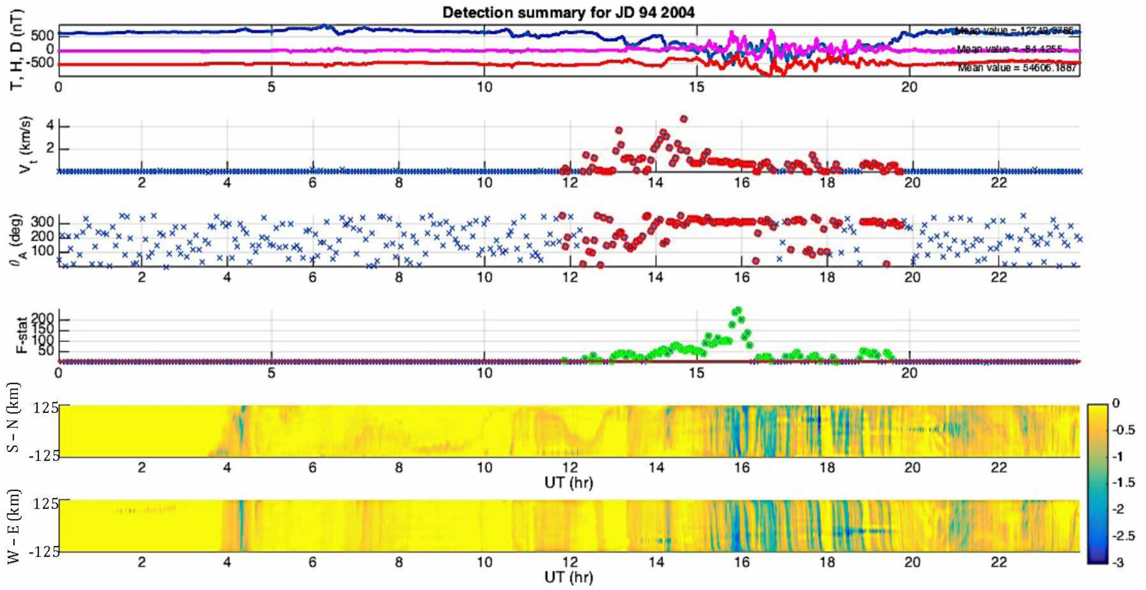

Fig 4.1 Example of data sets considered for GAIW study on JD 94 2004. The panels display (from top to bottom): the ***B*** *field components, estimated trave velocity, back azimuth, Fisher F-statistic, and riometer CNA keograms. The geomagnetically active time ranges from approximately 10 – 15 hours UT, during which time GAIW were received.*

Fig 4.1 illustrates the time series of the parameters that are considered when identifying a GAIW event. The panels display, from top to bottom, the three components of the geomagnetic field, the trace velocity, the back azimuth, the Fisher F-statistic, and the North-South and East-West PFIR keograms. It is immediately apparent that between the hours of roughly 10 – 15 UT a disturbance was concurrently recorded on the GIMA, the PFIR, and the I53US microphone array. During this disturbance we observe heightened geomagnetic activity and ionospheric opacity consistent with a geomagnetic sub-storm. The simultaneous acoustic HTV's have the characteristic parameters of GAIW. They have a consistent back azimuth, most frequently centered to the north. Over the period when the GAIW were being received there was some fluctuation in the F-stat, although it was largely over 50. Conversely, observations of the F-stat for MAW suggest that it rarely peaks 50, and as such the F-stat is a useful parameter to observe in identifying GAIW.

In all cases, when we identify a GAIW event we look for HTV's with the parameter distinctions discussed in Chapter 2, (namely $V_t > 0.6$ km/s, MCCM > 0.6 and Fisher F-statistic on average above 50), as well as concurrent geomagnetic activity. Whenever there is available data from the PFIR and PFASC they are also included. A received acoustical signal may be considered a GAIW signal relevant to this study provided it is persistent in time (both to remove spurious data due to clutter and to differentiate from the much better understood AIW) and is concurrent with active geomagnetic conditions and associated auroral phenomena.

Disambiguating AIW from GAIW events can be difficult. Secondary signals refracting from within the thermosphere and dispersion due to coupling with gravity waves can cause an isolated AIW waveform to result in several minutes of coherent signal detection on the ground [2,4,5]. Compounding matters further, isolated AIW events are frequently observed during times of active GAIW signal reception. We found that inclusion of HTV infrasonic events that lasted more than 1 hour was sufficient to differentiate isolated AIW from GAIW events when compared against events previously identified by experts in the field. If further disambiguation is required, then the waveforms may be considered. AIW usually exhibit an impulsive waveform with a sinusoidal ring of increasing period, in contrast to the sustained, irregular waveforms associated with GAIW.

Generally speaking we would like to confine our studies to well correlated signals. We have performed trial and error studies on GAIW and found that restricting our attention to signals satisfying MCCM > 0.6 is usual sufficient to disambiguate signals from clutter. Interestingly, in many cases restricting our attention to signals with higher MCCM, (for instance MCCM > 0.9), had little effect on the results.

Sometimes GAIW and MAW events occur simultaneously. While the GAIW are often high amplitude enough to observe through the MAW, separating the waveforms is essentially impossible and some contamination is expected. For this reason GAIW events that coincide with MAW's are removed from the study as well. It should be noted that MAW occur most frequently in the winter months as observed in Wislon and Olson's studies [35]. As a result, there is a greater frequency of GAIW events included for this study in the summer months. Fig 4.2

displays a magnetometer data and a signal detection summary for a concurrent MAW and GAIW event. Signals consistent with MAW are present from approximately 10-24 UT. Around 17 UT, there is a sudden increase in trace velocity along with a shift in back azimuth and spike in F-statistic values, suggesting a concurrent GAIW event. This example, and other similar cases, were rejected from the pool of GAIW events studied.

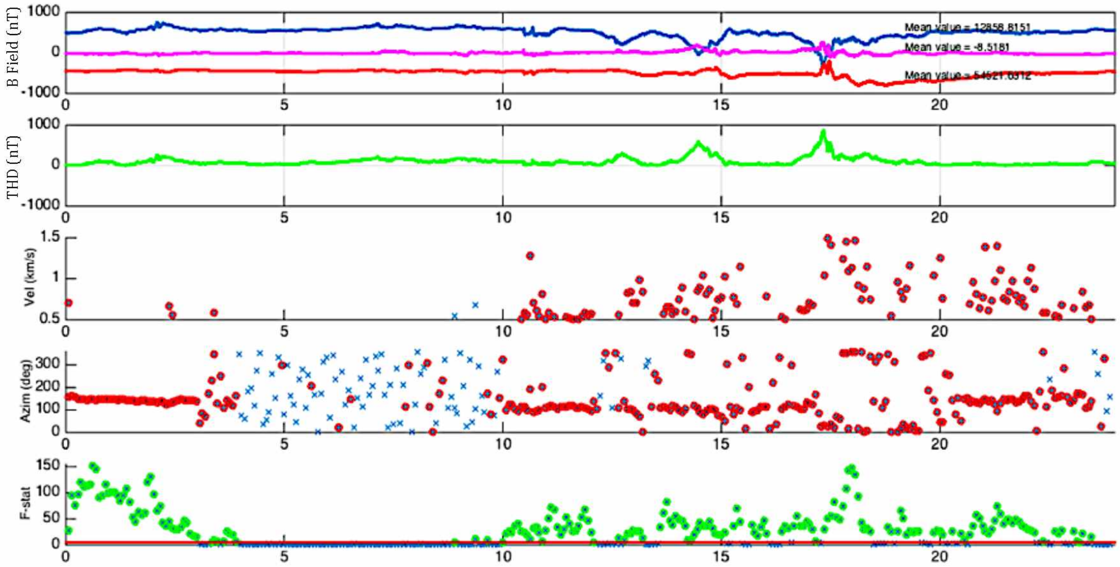

*Fig 4.2 An example of concurrent MAW and GAIW, a situation that is excluded from the study. The **B** field, THD vector, trace velocity, back azimuth, and Fisher F – statistic are shown. MAW HTV's are present from approximately 10-24 UT. Around 17 UT, the increased trace velocity, sudden shift in azimuth, and spike in F-stat values correspond with a concurrent GAIW event.*

Lee has suggested that MAW and other HTV's may be classified based on trace velocity alone, with MAW satisfying $v_t < 0.6$ km/s [13]. Certainly in many cases this holds true, as evidenced by the excellent performance of Lee's automated methods. Yet, conversely, over the course of the solar cycle studied we find many instances of long duration signals showing consistent back azimuths pointing to known MAW sources satisfying 6 km/s $< v_t <$ *2 km/s*, particularly over winter months when MAW are expected to occur. We interpret these signals as unusually high trace velocity MAW. As an example, in Fig 4.2 hours 21-23 UT show HTV's generally well over 0.6 km/s with some over 1 km/s. Yet the back azimuth is centered about 130^0, which is consistent with the known MAW signals received throughout the day and points toward the St. Elias mountain range, the second most common source of MAW received at I53US.

It should be noted that restricting our studies to events concurrent with heightened geomagnetic activity and free from MAW clutter causes considerable statistical selection. While this may limit certain information regarding temporal variation etc. it is justified by the principal goal of this study, which is to ascertain the specific ionospheric and geometric conditions suitable for GAIW production. For this effort it's important that we first understand the cherry-picked cases before we try to explain their statistical occurrence, etc. Therefore it is fundamental to the study that clutter, MAW contamination, and 'little green men' signals are judiciously excluded. As we will see, many consistent features of GAIW that may have been under-discussed in previous publications will become an integral part of the narrative given the heavy constraints of this study.

4.2 Characteristics and Consistent Features

During the period from January 2003 when I53US went online to 2014 a total of 63 GAIW events have been observed and included in the present discussion. Fig. 4.3 depicts histograms of the occurences by year (top panel) and month (middle panel), as well as signal arrival by hour (bottom panel). Occurrences by year and month follow predictable patterns, with the most events happening during years of solar maximum. We interpret the monthly variation as a roughly uniform distribution with the decline in occurrences in the winter due to exclusion based on the presence of MAW. The diurnal variation, however, is quite interesting. These signals are clustered about 15 UT. While it is somewhat rare, we occasionally see GAIW HTV's arrive as early as 5-6 UT; conversely after 16 UT signal detection drops off steeply with very few signals detected after 21 UT.

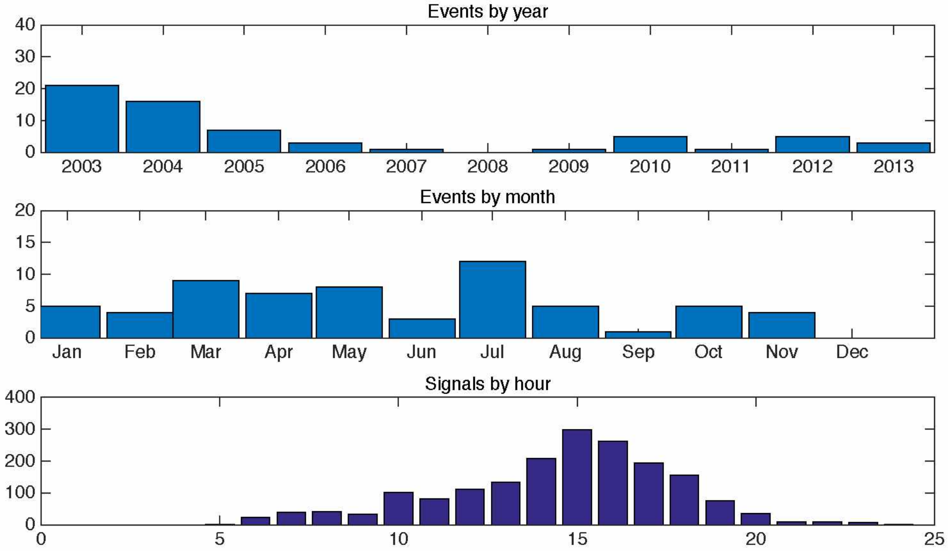

Fig 4.3 Histograms of GAIW detections 2003 – 2014 by year, month, and day. The top two panels demonstrate the number of events over each year and month respectively. The bottom panel shows when the signals were received during the day.

While there are great variations in many of the parameters of the GAIW events, consistent patterns are present. The vast majority of GAIW signals are received from the northern quadrant of the sky. There is a peak of signal back azimuth centered at 330^0, which is 30^0 west of geographical north and near magnetic north. This is in contrast with previous studies, in which presumably aurora related HTV's were shown to exhibit nearly uniform back azimuths with a slight increase in the range of 110^0 – 270^0, the exact range in which most MAW occurs [13]. This may serve to highlight the extent to which MAW's can masquerade as, or otherwise leak into and contaminate, GAIW signals.

Fig 4.4 gives histograms of back azimuths, trace velocities, and MCCM values for each of the signals received during the GAIW events considered. The majority of trace velocities associated with the signals fall in the range 0.6 km/s < V_t < 1.2 km/s. Even after carefully selecting to remove any MAW signals we find considerable numbers of detections with V_t ~ 0.6 km/s, commonly taken as the higher limit of MAW trace velocity for many prolonged MAW events.

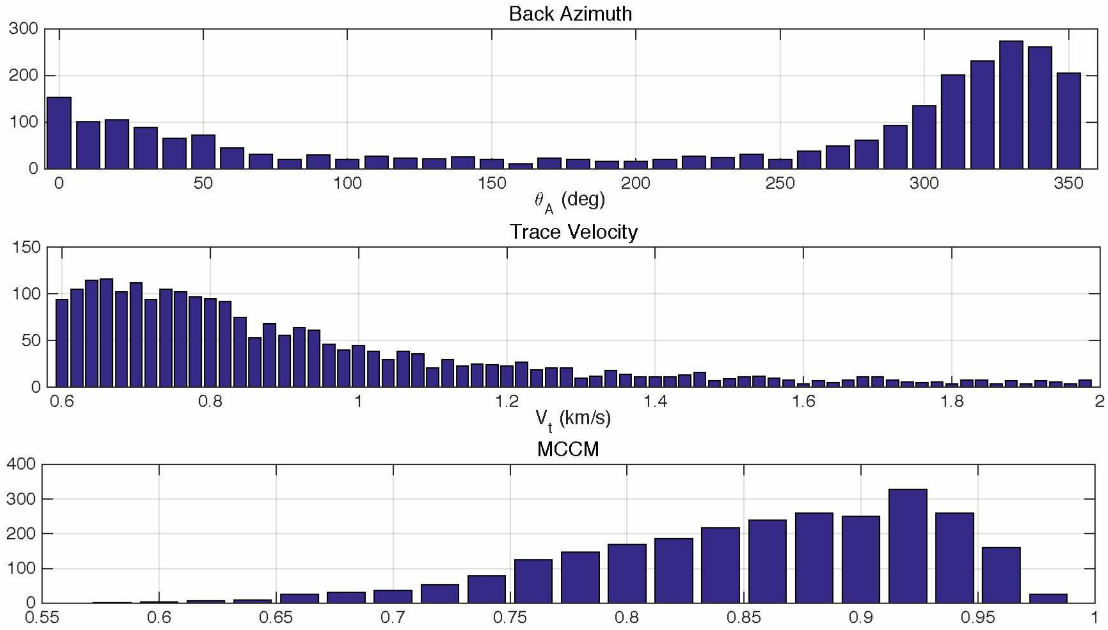

Fig 4.4 Histograms of back azimuth, trace velocity, and MCCM for the GAIW events studied.

Another noteworthy characteristic of the GAIW signals are the exceptionally high MCCM values. The median MCCM of the signals studied lies around 0.88, meaning that under the conditions specified for inclusion in the study the GAIW signals are highly coherent across the array.

Magnetometer data also reveals consistent trends. Oscillatory behavior in the H component of the field is present in all events for much of the duration of the periods over which the HTV's were received. Generally speaking the D component displays similar oscillatory behavior with a few counter examples. The oscillations exhibit a wide range of spectral content, with disturbances showing irregular features ranging from fractional second time scales to large-scale fluctuations averaging around twenty minutes in duration. Generally speaking, oscillations are irregular and PSD estimates show few significant extrema outside from the low frequency peak. Fig. 4.5 displays PSD's generated for the field *H* and *D* components for the GAIW event observed on JD 149, 2010. Window closing procedures found good resolution for 10 minute windows with an 80% overlap. The data has been band passed filtered to a passband of 0.01 – 0.15 Hz. The PSD estimate has been made using Welch's method with a Hamming window; the error curves represent a 95% confidence interval.

While the PSD for magnetometer data generally reflects irregular waveforms, in many cases a subtle broadband peak may be observed in the 15 – 30 mHz passband, as is present in the top panel of Fig 4.5 centered around 25 mHz. Such peaks are of particular interest as the frequency coincides with that of the observed infrasonic signals. In the GAIW examples included, these peaks occur in roughly 50% of the samples. In many cases there is also a large, sudden perturbation in the Z component (often referred to as a bay) which precedes the onset of GAIW. Bays and oscillations of the Z field component in excess of 200 nT occur in more than half of the cases (56%).

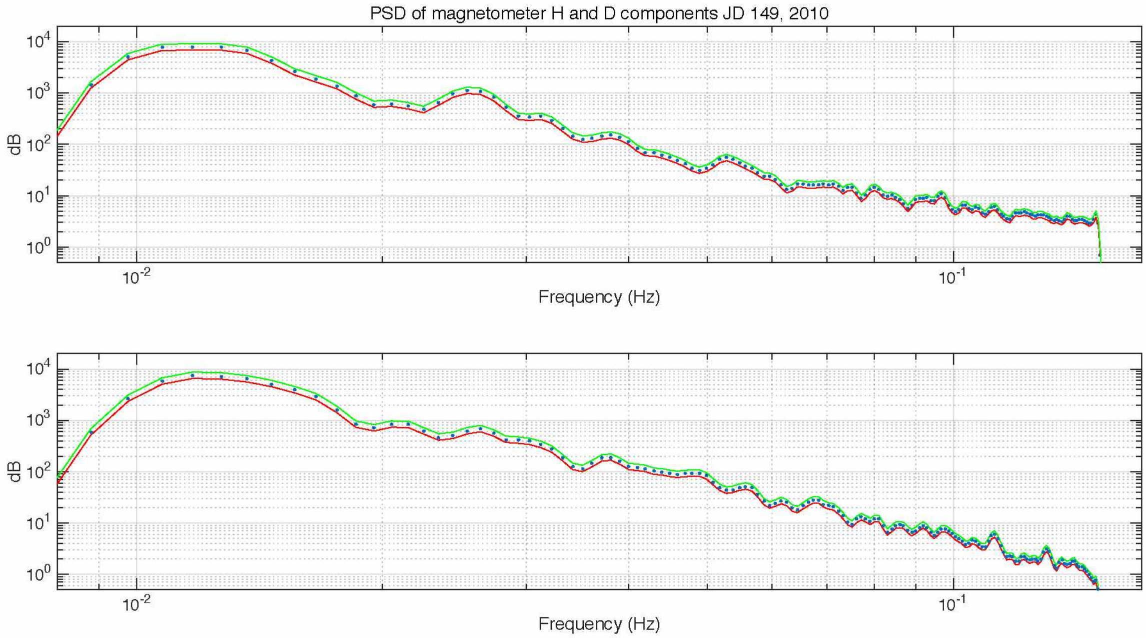

Fig 4.5 Example of magnetometer power spectral density for $\mathbf{B}_H$ *and* $\mathbf{B}_D$*. The H component is given by the top panel, the D component is on the bottom. The PSD's have been generated using Welch's method with a Hamming window. The data has been divided into 10 minute windows with an 80% overlap between windows. The confidence limits (red and green lines) have been generated for a 95% confidence interval. The field pulsations are generally irregular, although a subtle broadband peak between 15 and 30 mHz may be observed in many of the examples.*

Of the 63 included occurrences of GAIW, a total of 23 occurred while the PFIR was actively logging data. In all of these cases some CNA activity is present, with peaks in CNA data ranging from 1 to 5 dB with an average maximum absorption of ~ 3 dB. Every event that occurred while the riometer was running exhibited heightened conductivity moving across the overhead zenith at some point. When geomagnetic activity was particularly intense high conductivity regions crossed the overhead zenith several times per hour. During less intense geomagnetic storms regions of heightened conductivity passed overhead less frequently, with only one or two zenith crossings over the course of a GAIW event lasting more than an hour.

Fig 4.6 presents a summary of magnetometer, infrasonic, and CNA signals detected during the geomagnetic substorm of JD 94, 2004. During this period patches of heightened conductivity passed the overhead zenith at least several times per hour. When interpreting the PFIR keograms, directivity of the heightened conductivity motion is given by the “leaning” of the nearly vertical bands. In the panel second from the bottom the keogram cut is taken such that north is at the top, south the bottom of the graph. Therefore, a CNA band that has its top to the left of its bottom (i.e. exhibits a negative slope) moved across the field of view of the PFIR from North to South. Likewise, in the bottom panel the cut is taken from East to West such that the many bands that have an upper left to lower right diagonal tilt represent CNA peaks that moved from East to West. An estimate of the velocity of motion of the arc v is given by the slope of the vertical structures; in Fig 4.6 we see the Westward surging high conductivity regions moved through PFIR’s field of view at roughly 1 km/s.

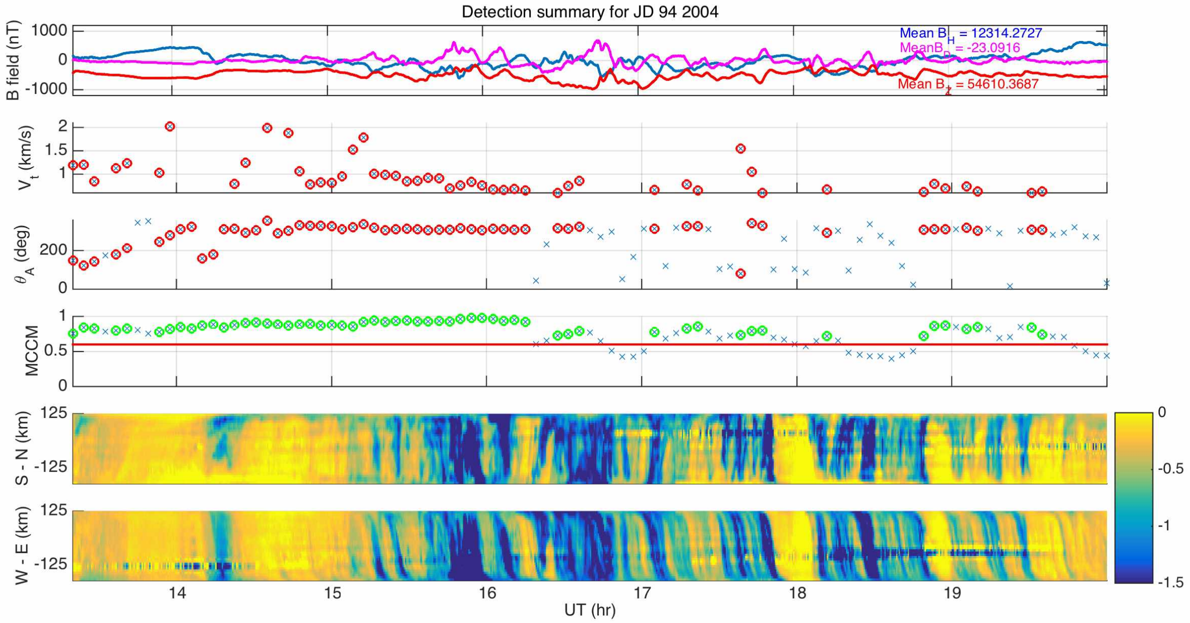

Fig 4.6 Detection summary for GAIW event of JD 94, 2004. The panels show, beginning from the top, the magnetic field components, trace velocity, back azimuth, MCCM, and riomenter keograms. The vertical structures in the bottom two panels demonstrate motion of electrojet currents crossing the overhead zenith.

In some cases it is possible to identify an infrasonic signal with a particular zenith-crossing event, as is depicted in Fig 4.7. The PFIR keogram shows that an isolated region of high conductivity crossed the overhead zenith beginning around 14:25 UT. Then a distinct, high amplitude infrasonic waveform arrived at the sensors of I53US approximately five minutes later, as one would expect from an acoustic source originating around 100 km altitude. The pictured infrasonic signal arrived with a very high trace velocity, indicating arrival from overhead. This event is interpreted as a prime example of traditional AIW in which an auroral electrojet current crosses the overhead zenith at a supersonic velocity and sets up an impulsive waveform in its wake.

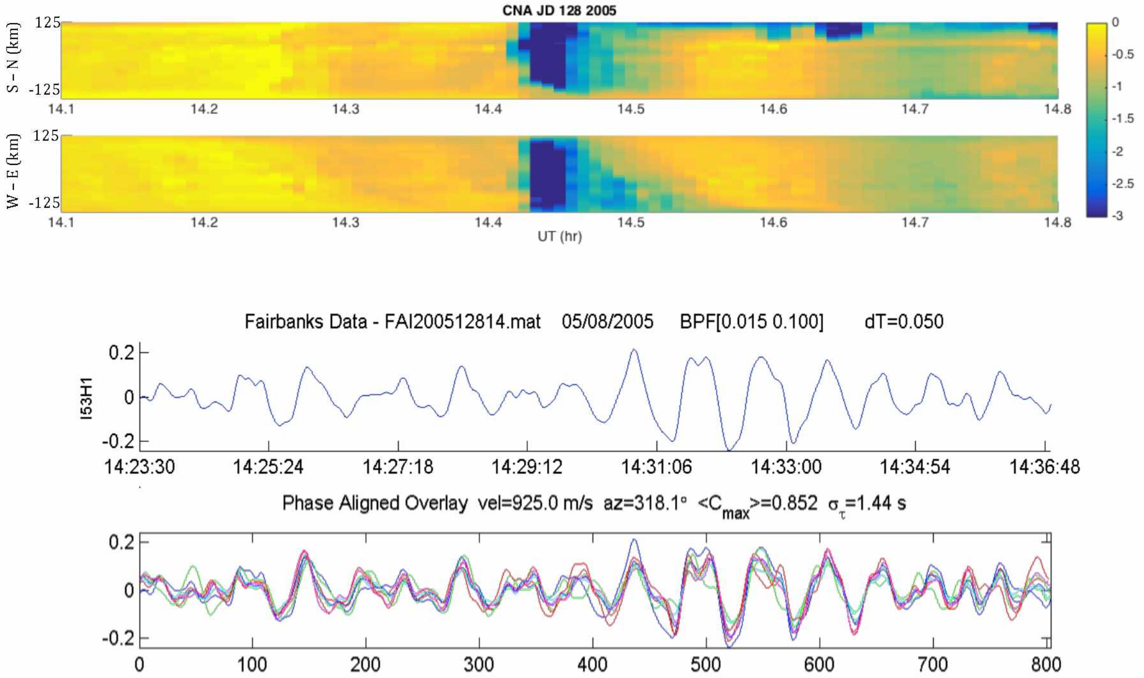

Fig 4.7 Example of a high conductivity arc and a correlated infrasonic signal. The first two panels display PFIR data where a region of high CNA (and therefore conductivity) passed the overhead zenith beginning at about 14:25 UT. The bottom two panels show the pressure time series for an individual sensor and the phase aligned overlay. A high amplitude infrasonic signal was observed at I53US some five minutes later.

In contrast, there are several examples in which heightened conductivity regions exhibit far less intensity and motion during GAIW events. Fig 4.8 presents a magnetometer, infrasonic, and CNA signal summary for the GAIW event recorded JD 161, 2004. In this example the magnitude of the THD vector rarely exceeded 100 nT, yet we observed many HTV's over the period. The PFIR shows that low intensity arcs of heightened conductivity passed back and forth across the overhead zenith very consistently throughout this period.

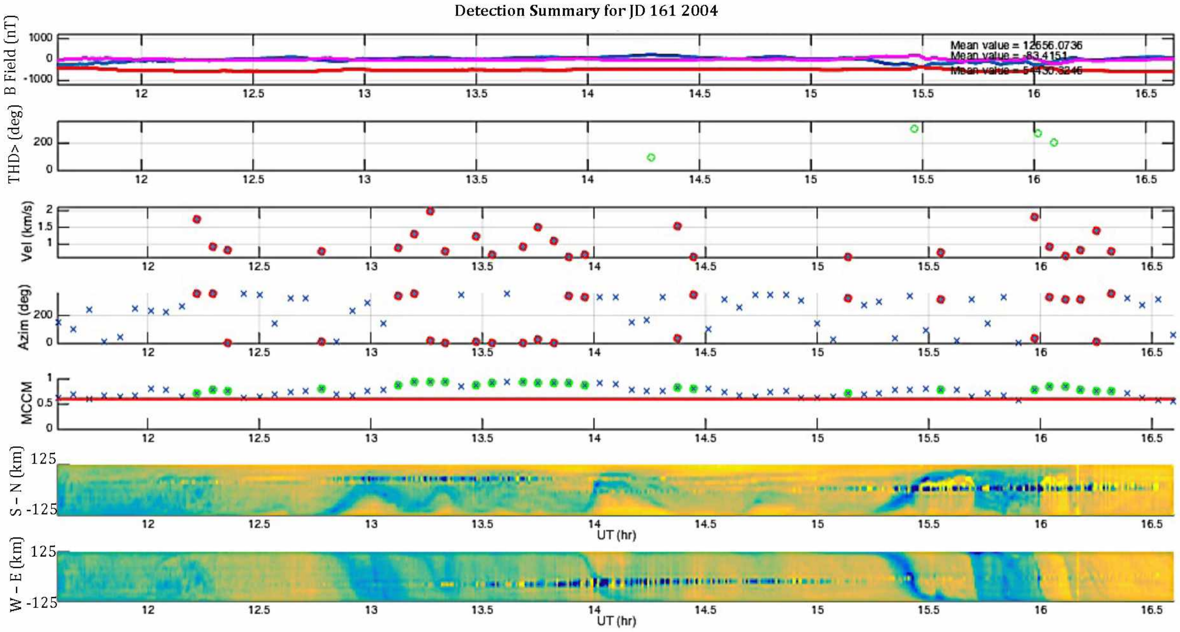

Fig 4.8 Signal summary of a GAIW event from JD 161 2004. Here the magnetic perturbations rarely exceeded 100 nT. The panels show, beginning from the top, the magnetic field components, the azimuth of the THD, trace velocity, back azimuth, MCCM, and riomenter keograms.

4.3 Model of Westward Drift

In most of the cases studied there is a clear tendency for the back azimuth to drift westward over the course of the event, particularly in the hours surrounding 15 UT. There is often an associated reduction in trace velocity, which suggests that the source has moved away from the overhead zenith. Fig. 4.9 presents an excellent example in which the westward drifting trend is very clear. Furthermore, in Fig 4.9 a subtle decrease in trace velocity may be observed. When the signals for all of the events are overlaid, the Westward moving trend becomes exceptionally clear. In Fig 4.10 the back azimuths for all of the signals have been overlaid, and a transformation has been made such that north lies at 180^0 for continuity.

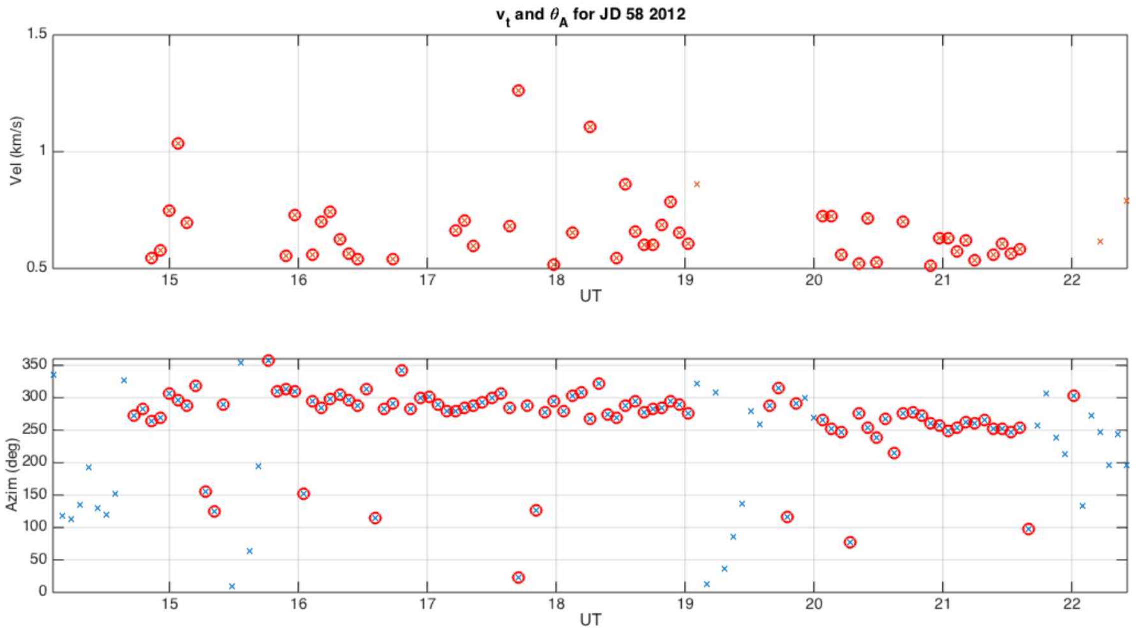

Fig 4.9. GAIW trace velocity and back azimuth signal summary for JD 58 2012. Westward drift is clearly observed in the back azimuth over the course of this event. As the event draws to a close there is a reduction in V_t consistent with a source moving away from the overhead zenith.

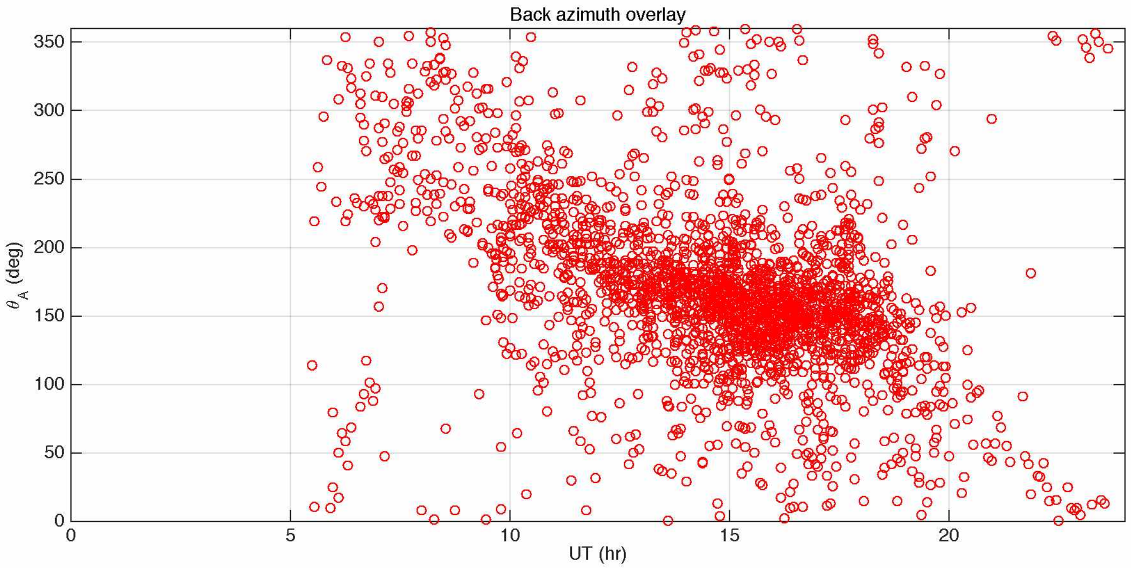

Fig 4.10 Overlay of back azimuth for all signals from GAIW events satisfying V_t > 0.65 km/s and MCCM > 0.6. Note a transformation has been made such that North lays at 180^0 for image continuity.

Wilson has proposed that this Westward drift could be associated with a stationary ionospheric source centered about the anti sun-earth line [49]. The Westward drift would then be attributable to the sensors passing underneath the source as the earth rotates. Fig 4.11 gives a cartoon of the geometry associated with this model. Here, the yellow dot represents the sun and the black great circle bisecting the Earth represents the intersection of the Earth's surface with the sun-Earth plane. The green circle represents an idealized auroral region where the infrasonic source is presumed to be. The spherical triangle elements are *a*, the arc from the source to the pole, *b*, the arc between the sensors to the source, and *c*, the arc from the sensors to the pole. Then according to the geometry pictured in Fig. 4.11, the back azimuth would coincide with the spherical angle *A*. Since the arc lengths *a, b,* and *c* are all readily available an expression for *A* is given from basic spherical trigonometry (see, for instance, Todhunter)[50]:

$$\cos(A) = \frac{\cos(a) - \cos(b)\cos(c)}{\sin(b)\sin(c)}. \tag{4.1}$$

Technically, this expression is valid for a source located on a spherical surface. In reality, we expect that the source is around 100 km elevated from the surface. This turns out to be a minor correction given that arcs *a, b*, and *c* typically have length scales of $\sim 10^3$ km and that the Earth itself deviates considerably from a perfect sphere. Fig 4.12 displays the source angle *A* for sources at latitudes of 50, 60, 70, and 80 degrees where due north from Fairbanks is represented by 180^0. The source angles are generated from (4.1) for a 24-hour period. It is worth noting that for sources south of Fairbanks there is a discontinuity as the source passes to the south at local midnight. Casual observation of Fig. 4.10 above demonstrates little observable trend of discontinuity at local midnight.

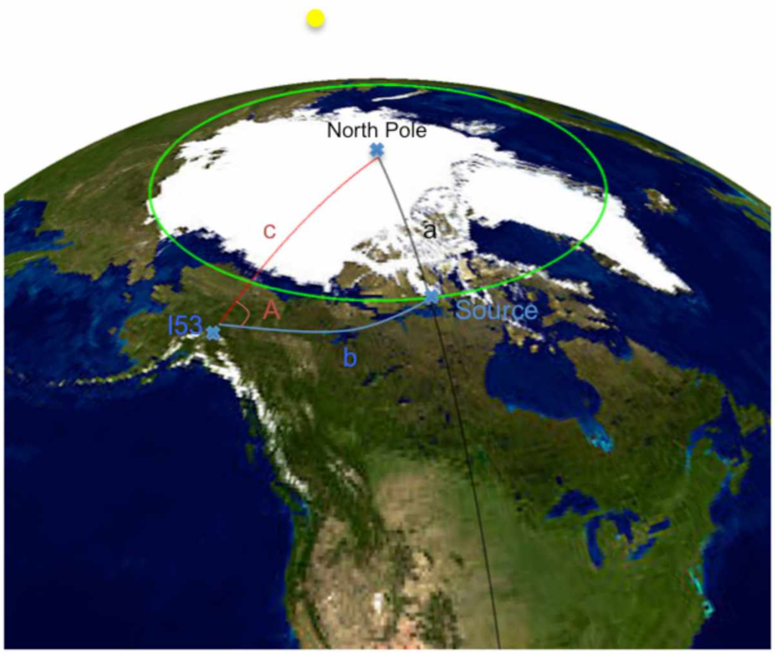

Fig 4.11 Model of westward drift where the angle A is the measured back azimuth. The black line represents the anti-sun Earth line (the sun is the yellow dot). The green circle represents 75^0 north with the arc lengths given in eqn. 4.1 labeled as a,b, and c.

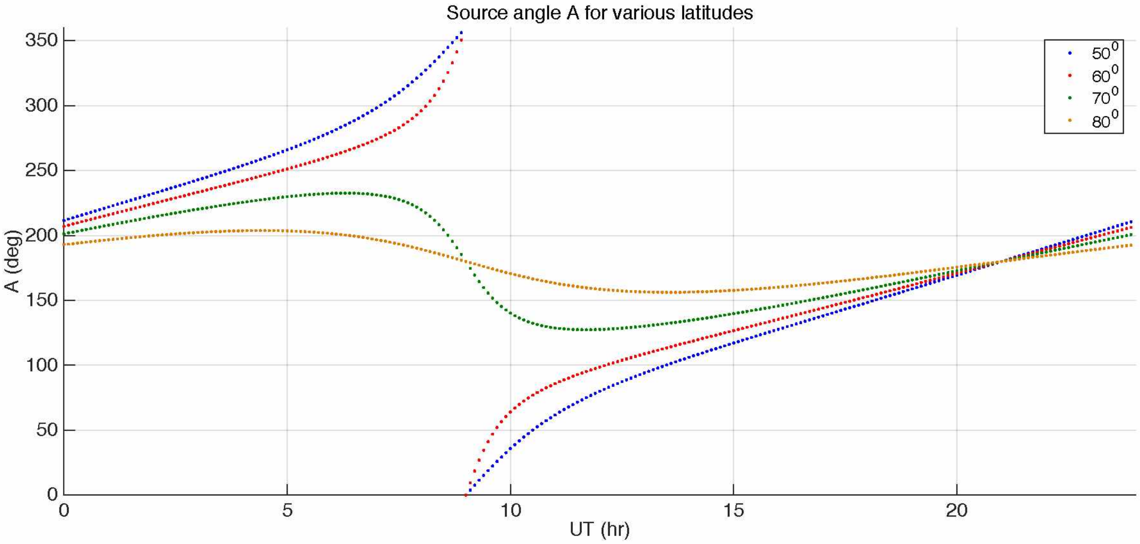

Fig 4.12 Source angles A over a 24 hour period for sources at 50,60,70, and 80 degrees.

In terms of testing the fit of the proposed westward drift model, non-linearity makes regression and other strategies untenable. Instead, we prefer to develop a loss function approach in which the root-squared-sum of the distance of the data values to the function value is minimized. For most of the events included in the study, there is considerable scatter in the values for back azimuth and too few values of back azimuth for reliable fitting. We therefore choose to overlay the various back azimuth values and make a fit to the resulting vector. The value for source latitude that we find is then interpreted as an average value for GAIW events as a whole. The computation is performed with Matlab's built in *fminsearch* function; we find the loss function is minimized for a source at 75^0 North latitude[51]. The result is robust; excluding signals based on low MCCM or varying V_t has little impact.

While Wilson suggested a source centered about the anti-sun Earth line there seems to be little physical evidence to constrain the source to this region. Instead, we relax this constraint and allow for a multivariate minimization. In our model, choosing a source stationary above a region removed from the anti-sun Earth line will result only in a translation of the source angle in time, which may easily be accomplished by a reindexing. The same loss function minimization approach may then be applied accounting for both the source latitude and angular distance from the anti-sun Earth line. This approach finds a best fit for a stationary source at $\sim 77^0$ north latitude and $\sim 60^0$ longitudinal measure east of the anti-sun Earth line. Fig. 4.13 displays an overlay of the observed back azimuths alongside the modeled back azimuth (blue line) for a point source at this location.

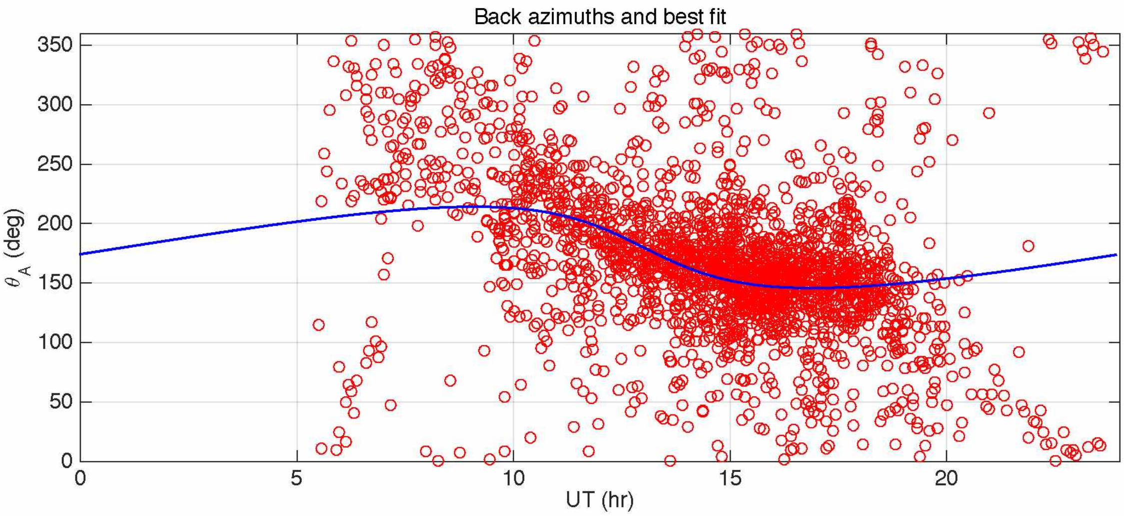

Fig 4.13 Best fit source angle and back azimuth overlay. The modeled back azimuth for a stationary source ~60^0 longitude east of the anti-sun Earth line at 77^0 north latitude (blue line) is present alongside the observed back azimuths for signals satisfying MCCM > 0.65.

As is apparent from fig 4.13, there are many outliers far from the expected angle value. This may in part be due to the large uncertainties in back azimuth for overhead incidence. Perhaps more importantly, as shown in Chapter 2 we typically expect ionospheric sources outside of a takeoff angle of 40^0 to be refracted away. Consider a point source stationary 100 km overhead a coordinate at 65^0 north latitude. Rudimentary calculations reveal that the observer on the ground would drift through the window of steep enough takeoff angles to receive signals on the ground in about 2 hours. The fact that the westward drift model fits well for GAIW infrasonic signals received anywhere from 13 to 17 UT (and in some cases considerably away from this regime) suggests that the source itself is substantially spatially extended as opposed to a point source – in keeping with both intuition and existing models. Notably, we can presume from this observation that the source of GAIW tends to be on the scale of hundreds of kilometers centered about 60^0 east of the anti sun-earth line. A significant feature of the westward drift model is that it yields an estimated source region consistent with the geomagnetic region wherein injections of energetic electrons are deposited during geomagnetic substorms. Unfortunately the high uncertainties and sporadic behavior of GAIW infrasonic signals impede an exact, quantitative description of the source geometry.

It must be noted that 77^0 latitude lies some 1500 km's north of College, Alaska where the infrasound array is receiving the signals. Sources so far distant are expected to be refracted away, so discussion is in order. First, we observe that the considerable spread in the received back azimuth values causes substantial uncertainty in the source latitude and longitude. Furthermore, as discussed above the source region must be spatially expanded to the order of 10^2 km's, whereas our model is valid for a point source. Finally, auroral features are typically dependent upon magnetic coordinates more so than geographic ones. A revised model incorporating an extended source region with comparisons to magnetic coordinates is currently being investigated.

As a final note, in principle it may be possible to further constrain the source location by expanding the Westward drift model to allow for an elevated source and to add V_T as a variable such that source elevation may be included as an additional parameter to be minimized. Again, the large uncertainties in V_T for very high velocities made preliminary results on such an expanded model very inconsistent. Specifically, using a Nelder-Mead approach, the model was unphysically sensitive to initial parameter inputs. Perhaps given enough signals to consider and a rigorous selection process some further information could be gleaned.

4.4 Comparison to Existing Models

There has been historic success in modeling AIW. In this text we reference the seminal papers from Wilson, Chimonas, Hines, and Swift in discussing comparison of the GAIW to existing models [2,4,5,36]. All of these models assume motion of the auroral electrojet arc as the primary generation mechanism for auroral infrasound. Here we consider such models, then in the following section we ask whether such models are sufficient to describe the variety of GAIW events included in this study.

As mentioned in chapter 3, the equations usually taken to govern the ionospheric ion-neutral interactions are:

$$\frac{dn}{dt}+n\nabla\cdot\vec{u}=0, \tag{4.2}$$

$$mn\left(\frac{d\vec{u}}{dt}\right)-mn\vec{g}+\nabla p=\frac{\vec{j}\times\vec{B}}{c}, \tag{4.3}$$

$$\frac{dp}{dt}-\gamma kT\frac{dn}{dt}=(\gamma-1)\vec{j}\cdot E. \tag{4.4}$$

In order to proceed from this point a specific model of ionospheric conductivity, geometry, and dynamic evolution must be adopted. After extensive studies of AIW events compared against all-sky camera images Wilson proposed the model diagramed in Fig 4.14. In this scenario, an auroral electrojet arc is present and persistent in some neighborhood of the overhead zenith. When an auroral surge passes along the arc it causes a bend or wrinkle in the arc to move along its length at velocity V_A. Wilson pointed out that if V_A is just above the sound propagation speed then a conical bow wave might be expected to develop in its wake. Subsequent studies have shown that considerable acoustic propagation is possible for V_A at or above the sound speed and that bow waves are not necessary for receiving AIW signals on the ground [4].

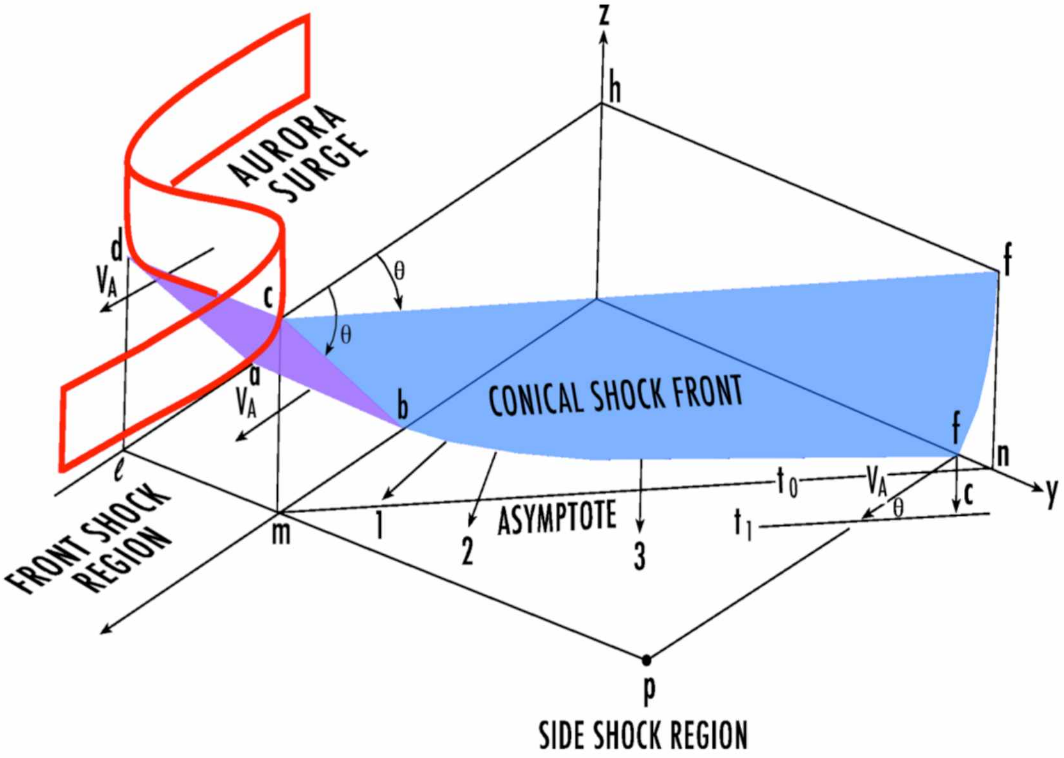

Fig 4.14 Model of AIW as a shock wave generated by supersonic surges along the auroral arc. This excellent and succinct imagery displaying the model parameters is borrowed from Wilson [6].

Mathematically, this model has been developed and tested by assuming a cross-sectional map of the travelling auroral arc. In order to cast equations (4.2)-(4.4) in a more tenable form the variables n, $\boldsymbol{u}$, and p are linearized by the usual method of letting $n = n_0 + n_1$ and so forth where n_0 and p_0 are constants. The source terms involving $\boldsymbol{j}$, $\boldsymbol{B}$, and $\boldsymbol{E}$ are assumed to be of first order already (see Swift 1973 for a detailed discussion of this assumption) [4]. The resulting linearized equations are given by:

$$\frac{\partial n_1}{\partial t} + \vec{u}_1 \cdot \nabla n_0 + n_0 \nabla \cdot \vec{u}_1 = 0 , \tag{4.5}$$

$$m n_0 g + \frac{\partial n_0}{\partial z} kT = 0 , \tag{4.6}$$

and,

$$mn_0 \frac{\partial \vec{u}_1}{\partial t} + mn_1 g\hat{z} + \nabla p_1 = \frac{1}{c}\left(\vec{J} \times \vec{B}\right). \tag{4.7}$$

Once again, in order to reduce the equations into a more intuitive form, the terms involving gravity are taken to be zero. We will discuss what effect these gravity terms have on the model subsequently. With these assumptions we can combine the equations by taking the divergence of Eq. (4.7) and the time derivative of Eq. (4.5). Finally, taking the ideal gas law as the equation of state, algebraic substitution yields

$$\nabla^2 p_1 - \frac{1}{C_s^2}\frac{\partial}{\partial t^2} p_1 = \nabla \cdot \left(\frac{\vec{J} \times \vec{B}}{c}\right) - \frac{(\gamma - 1)}{C_s^2}\frac{\partial}{\partial t}\left(\vec{J} \cdot \vec{E}\right), \tag{4.8}$$

where $C_s = (\gamma kT/m)^{1/2}$ is the local sound speed.

Equation (4.8) is an inhomogeneous wave equation for acoustic pressure with two independent source terms for the Lorentz force and Ohm dissipation [4]. The formal solutions to such equations have been extensively studied; see, for example, Jackson 1963 [51]. Further progress requires a specific model of electromagnetic fields and currents in the ionosphere. Traditionally, the model for an auroral electrojet is developed from an electron number density (n_e) approach. Numerous experimental and theoretical studies have suggested that the sharp increase in n_e within the auroral electrojets is largely confined to a narrow altitude band between 90 and 150 km [20]. Fig 4.15 illustrates the presumed electron density n_e profile for a realistic atmosphere during a quiet day scenario (blue curve) and an active auroral electrojet arc (black curve).

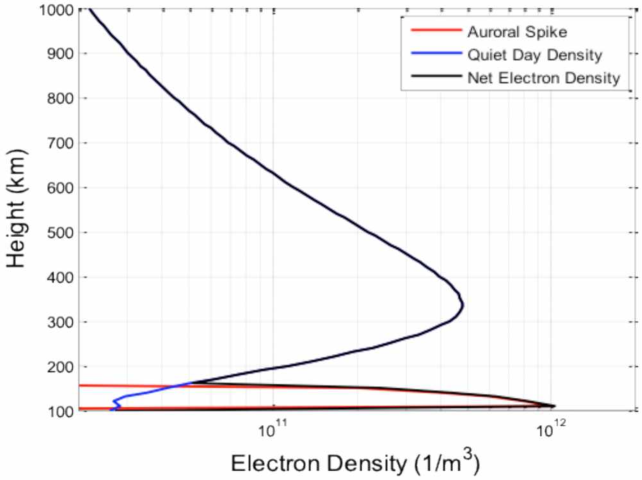

Fig 4.15 Modelled electron density profile during an active auroral arc. The spike in electron density centered about 110 km is presumed to be typical of the increased density within an auroral electrojet arc

Typically a somewhat simplified profile for the height integrated electron density (N_e) is taken for mathematical convenience. The electron density "spike" around 100 km is modeled as being confined to a vanishingly narrow vertical profile ΔZ. This proves to be a very important assumption for certain cases. The idea is that the region where the highest electron density meets the dense neutral atmosphere and the acoustic pressure waves are produced (around 100 km altitude) is well approximated as an interaction over small vertical scales. In point of fact, the increased electron density associated with electrojet arcs and other auroral forms may stretch tens to hundreds of kilometers into the sky. It is unclear that the observed infrasound is physically generated over such a thin altitude profile.

Horizontally, the arc is typically modeled as being of infinite length, which effectively makes the problem two-dimensional. Several studies have shown that this approach gives good approximation to fully three-dimensional models and allows for much more efficient computation and access to some closed form analysis. Taking the x-axis as the lengthwise axis along the arc, the cross section of the arc is modeled by the height integrated electron density as a piece-wise, linear function of y. A cartoon of an example cross section is depicted in figure 4.16. Smooth curve approximations have also been computationally considered. Swift has shown that the cross section of the arc has a major impact on the specific pressure waveforms generated [4].

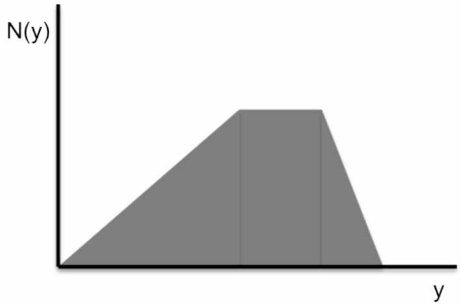

Fig 4.16. Example of a height integrated electron density profile. A variety of such profiles are assumed in the classic model of an auroral electrojet arc [4,5].

The final model parameter to consider is the assumed geometry of the electric field; both the ambient field in which the arc is immersed as well as the field resulting from the current-like behavior of the charges within the arc itself. Typically the **E** field is assumed to be in the y direction and perpendicular to the axis of the electrojet. Some evidence exists suggesting that this approximation is often justified; in any case it is a common simplification in aeronomy theory that has been validated by many positive results [20]. Under this assumption we can again utilize Ohm's law to arrive at (see equation 3.6)

$$\vec{J} = \sigma_H E_y \hat{x} + \sigma_P E_y \hat{y} \, . \tag{4.9}$$

Substituting Eq. (4.9) into Eq. (4.8) then yields an expression for the pressure pulse in terms of the fields and ionospheric conductivities

$$\left(\nabla^2 - \frac{1}{C_s^2} \frac{\partial^2}{\partial t^2} \right) p_1 = \left(\frac{E_0 B_0}{c} \sigma_H' + \frac{(\gamma - 1) \nu}{C_s^2} E_0^2 \sigma_P' \right) \frac{\partial}{\partial y} n_e \, . \tag{4.10}$$

Here C_s is the local sound speed and

$$\sigma'_{P,H} = \frac{\sigma_{P,H}}{n_e(x, y - vt, z)} \tag{4.11}$$

describes the time and space dependent Pederson and Hall conductivities for the arc moving in the y direction with constant velocity v and presumed electron density n_e satisfying the height integrated profile.

At this point, a series of algebra intensive manipulations may be applied to preserve some analytic insight, however solutions must still be pursued computationally [4,5]. We have an inhomogeneous wave equation with source terms described by ambient electromagnetic fields and ionospheric conductivity. The reader may well consider the referenced works for greater details on the mathematical and computational methods that have been considered. Here, I only summarize the results of this model as described in several previous papers.

An electrojet arc moving across the overhead zenith at super-sonic speeds will be expected to produce detectable pressure signals on the ground with the duration and intensity of the signals governed by the velocity of the arc's motion, the cross section profile of the electron density, and the field strengths and conductivities. Generally speaking, faster arc motion v produces briefer but higher amplitude signals up to a very high velocity limit. All other parameters remaining equal, broader profiles for the arc also produce longer signals. For a singular zenith crossing of the arc and neglecting reflected signals etc. this model predicts a detectable infrasonic wave train of 10 to 20 minute duration. Observationally, this wave train duration proves to be somewhat high – a typical isolated AIW signal is rarely longer in duration than 10 minutes. Interestingly, in most of the instances in which GAIW events occurred during PFIR's operation, overhead crossing events occurred at a frequency of at least one every 20 minutes for some duration of the event, supporting an interpretation that many of the observed GAIW signals might be describable as a series of isolated AIW's interacting.

In keeping with Wilson's intuitive suggestion, evaluating equation (4.10) for subsonic velocities shows that for arc's moving overhead subsonically very little energy is propagated above the acoustic cutoff frequency. A ground-based sensor would not be expected to receive any signals for such a situation. In each of the 23 GAIW events recorded during PFIR's operation, we note frequent overhead passing of high conductivity regions. In all cases the motion of these heightened conductivity patches was well above the sound speed. Fig. 4.8 displays some of the slower motions of these high conductivity regions; evaluation of the bottom panels shows that the high conductivity arcs moved overhead at velocities in the range of 0.5 km/s to 1 km/s. HTV's arrived exclusively following these zenith crossing events and occurred despite relatively low CNA values (~ 1 dB) and very subtle magnetic perturbations. In most of the other cases much higher CNA and magnetic perturbation values were logged, alongside much higher velocity of the electrojet arcs. This is also expected from the Chimonas, et al. model, since for arc velocities very far above the sound speed the resulting pressure pulses become smaller in amplitude [5]. We expect that for very fast arc motions higher values for conductivity and field strengths are necessary for the generation of AIW.

In comparing the model to observed data it is instructive to consider the direction of the THD vector. For an electrojet arc exhibiting the characteristics discussed in the model above, the expectation is that the THD vector will be perpendicular to the axis of the arc and parallel to it's direction of motion (again, analogous to a line current). Assuming that the observed infrasonic signals are generated at ~100 km altitude then it is reasonable to expect that the direction of the THD vector should be roughly equivalent to the back azimuth of the observed AIW infrasound signals, providing for the approximately five minute travel time of the acoustic signal. Through trial and error it has been established that a 5.5 minute lag between the THD measurement and corresponding infrasonic signal arrival yields particularly consistent results. Fig 4.17 provides a signal detection summary for magnetometer data, direction of the THD vector, and infrasonic back azimuth for the GAIW event of JD 104, 2003. The THD directions plotted represent the values calculated 5.5 minutes previous to the corresponding back azimuth estimates and measured clockwise from north.

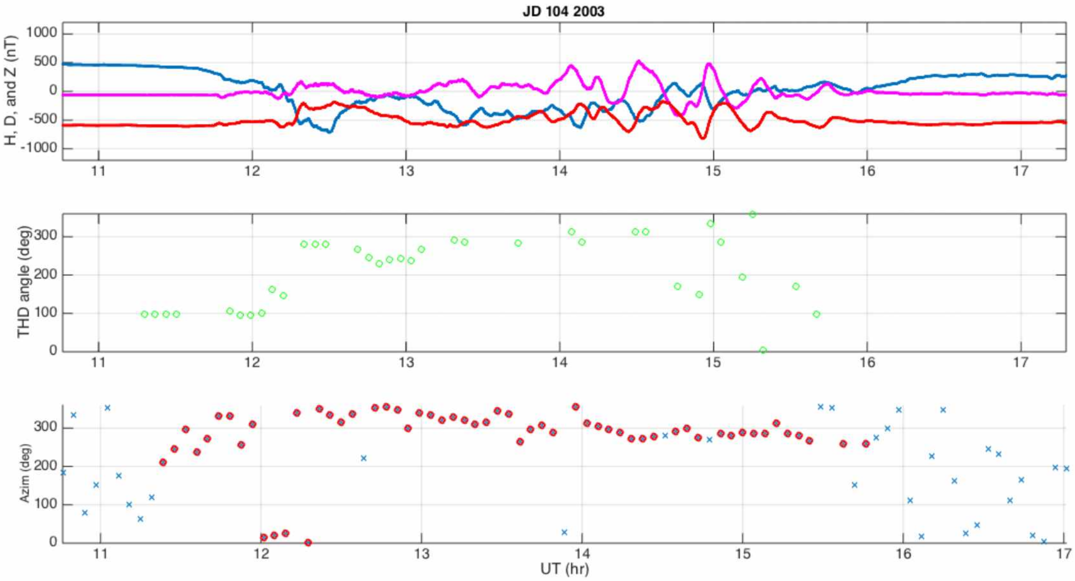

Fig 4.17 Plots of magnetometer time series, THD vector direction, and infrasonic back azimuth. The green data represent the THD angle measured clockwise from north and computed 5.5 minutes prior to the corresponding infrasonic signal shown as red circles in panel c.

When comparing the direction of the THD vector to θ_A we would like to restrict our observations to periods when some arc-like current form was present for appropriate comparison to the model. As a first effort towards this end, signals occurring when the magnitude of the detrended THD vector is less than 100 nT have been excluded. Furthermore, only acoustic signals with high trace velocities should be expected to correspond to ionospheric disturbances, hence an additional constraint that only signals with $V_t \geq 0.6$ km/s are considered. In Fig 4.18 there appears a histogram of the difference between the THD direction vector and back azimuth estimates for all of the signals that satisfied these conditions.

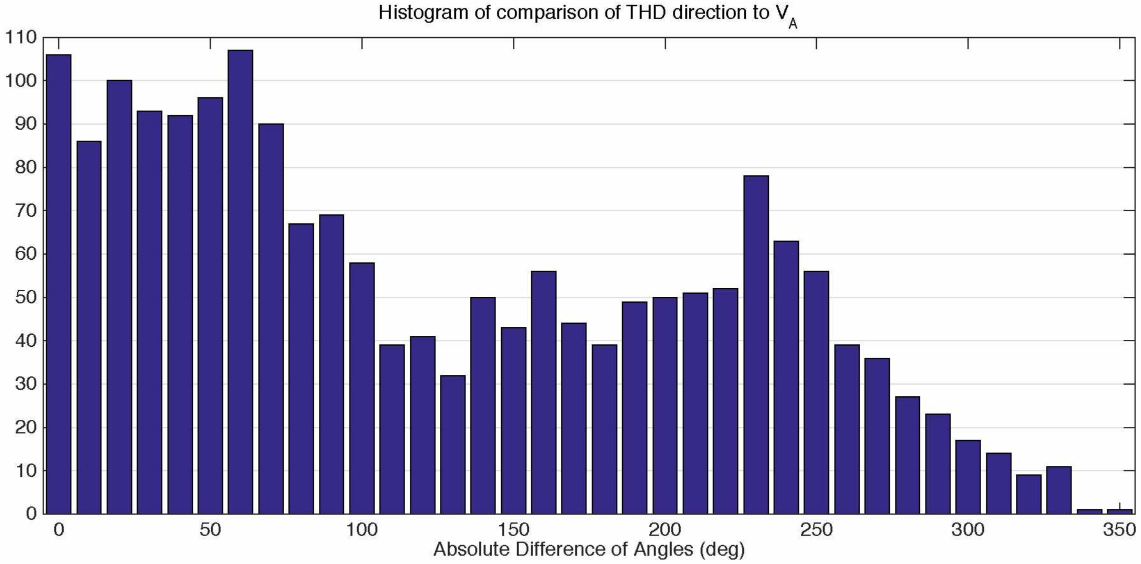

Fig 4.18 Histogram of the difference in angles between the THD direction and the back azimuth θ_A (absolute value). The THD angle is computed for 5.5 minutes prior to each HTV event satisfying $V_t \geq 0.6$ km/s and norm(THD) > 100 nT.

Consideration of figure 4.18 reveals that the differences between the angles do indeed often tend toward small values, as expected from traditional AIW models. The largest peak of values lies between 0 and 50 degrees while a smaller peak is centered about 230^0. This suggests that the THD vector is regularly pointed somewhat to the East of θ_A. The smaller peak around 230^0 may be related to roughly anti-parallel angles corresponding to, as an example, motion of the electrojet arc during a contraction of the auroral oval, but with the same systematic tendency to Eastward as seen in the parallel case. However, there are clearly many cases in which the angles are nowhere near parallel.

Despite the many instances in which sequential AIW events are demonstrably present during periods of GAIW, there remain counter examples in which HTV's are received during periods of heightened geomagnetic activity yet no overhead passing of an auroral arc is observed. Wilson has observed that such situations often arise during the break up phase of the geomagnetic sub-storm when pulsating aurora is present. Pulsating aurora is an auroral form in which broad patches of diffuse aurora glow oscillate in intensity with a periodicity on the order of a minute. In studies by Wilson et al. examples were found in which the GAIW waveforms showed similar periodicity with enhanced coherence with the auroral intensity pulsations when the expected 5 to 6 minute delay between generation and detection was accounted for [10]. Further studies demonstrated that while such examples could be found, there was no statically reliable coherence between the pulsating auroral intensity and the infrasonic waveforms [11,12]. Nevertheless, the fact that GAIW signals are detected during these periods and in the absence of any clearly defined auroral arc or high conductivity zenith crossing events suggests that the model by Chimonas et al. may be insufficient to fully capture the physical mechanisms responsible for the generation of GAIW.

Energetic precipitating particle interactions, a major factor associated with pulsating aurora and generally present during periods of heightened auroral activity, is absent from the Chimonas model as described above. Taken either independently or in conjunction with Joule heating from electrojet arcs, energetic particle precipitation (EPP) could contribute substantially to ionospheric pressure perturbations under certain circumstances. In an effort to better understand the specific conditions under which EPP may contribute to GAIW formation an experiment was undertaken at the HAARP (High Frequency Active Auroral Research Program) facility the Fall of 2012 in which the high energy radio transmitter, (usually referred to as the ionospheric research instrument, or IRI), was utilized to heat the upper atmosphere in an attempt to simulate heating similar to that due to EPP. Chapter 5 is devoted to theory and observations regarding pulsating aurora, the relationship between these concepts and the HAARP experiment, and conclusions to be drawn from the experimental results.

Chapter 5

HAARP Campaign 2012

5.1 Introduction

In chapter 4 it was noted that much of the observed auroral infrasound may be described by the existing models of AIW generation. However, there exist a number of examples in which GAIW's are received while no discrete auroral arc or similar structure is observed. Furthermore, this situation has been noted several times in the post-midnight sector to early dawn, when pulsating aurora was active. In this chapter we review observations and theories of pulsating aurora before considering it as a contributor to GAIW's. We then discuss the results of an experiment undertaken at the HAARP (High Frequency Active Auroral Research Program) facility in 2012 in an effort to artificially induce conditions similar to those expected within the ionosphere during pulsating auroral events and observe any infrasonic signals that propagate to ground based sensors.

5.2 Pulsating Auroras

Pulsating auroras have been well documented and studied since at least the 1970's. They are generally defined by characteristic features of temporal frequency and spatial extent. Typically pulsating auroras occur in the midnight to dawn quadrant and are observed during the break-up phase of an auroral substorm. The luminosity of the associated aurora generally oscillates with periods of seconds up to a minute or more. Spatially, the pulsating forms tend to span the range of 1-100 km extent horizontally and may appear in irregular patches or partial band or arc type structures. Vertically, pulsating aurora is observed to be very thin with vertical extent often limited to less than 2 km [53]. They also occur at altitudes lower than discrete auroral arcs. Within these constraints additional specification of pulsating auroral forms is sometimes made [12].

Observational data made by rocket-based sensors suggests that the primary generation mechanism for pulsating aurora is precipitating energetic electrons. Additionally, precipitating electron flux has been found to vary temporally in excellent synchronization with the observed auroral forms [10]. There has been an active debate regarding the physical processes that might limit the energy deposition of the impinging energetic electron beam to such a small vertical layer. For the purposes of the current discussion it is sufficient only to note that the thermalization of the electron beam may sometimes take place over these short vertical length scales; the interested reader may refer to the citations for many discussions of this phenomenon [54, e.g.].

In theory, given sufficient knowledge of the ionospheric conditions during pulsating aurora events it may be possible to develop another source term in equation (4.8) to describe the dynamic effects of energetic particle precipitation on the propagation of pressure wave forms. However, during pulsating aurora events the assumptions made in the Chimonas model of AIW are presumably no longer valid as specific auroral electrojet arcs are not necessarily observed. Maeda and Watanabe developed an analytic model of pressure perturbations due to EPP thermalization in 1964 [54]. However, analytic solutions demanded approximations such as an isothermal atmosphere that limit the validity of the results. Here we instead adopt Wilson et al.'s zeroeth order approximation of the over-pressure that is easily made by treating the thermalization as taking place over a cylindrical section of the lower ionosphere [10]. This approach also has the advantage of remaining valid for the ionospheric heating made by HAARP's IRI as discussed below.

Analysis of visual emissions during pulsating aurora has been used to estimate the energy flux over a cross section of the EPP beam yielding typical values of $F \approx 5$ erg/cm^{2}s. Often the heating appears to occur over a uniform horizontal area A during the pulsation. Then the rate of energy delivery over the area A satisfies

$$\frac{dU}{dt} = FA \,. \tag{5.1}$$

For convenience, we take the flux to be constant over the period of heating, noting that generalization to dynamic flux rates may be made if desired. Then

$$\Delta U = FA\Delta t\,. \tag{5.2}$$

Since the heating appears to take place over a roughly uniform volume, thermodynamic considerations state

$$\left(\frac{\partial U}{\partial T}\right)_V = C_V = \frac{5}{2}Nk_B \approx \frac{\Delta U}{\Delta T}, \tag{5.3}$$

where T is the temperature, C_V is the specific heat, and the factor 5/2 is taken for diatomic gaseous molecules as expected in that region of the atmosphere. Combining equations (5.2) and (5.3) and utilizing the ideal gas law gives

$$FA\Delta t = \frac{5}{2}Nk_B\Delta T = \frac{5}{2}Nk_B\left(\frac{\Delta PV}{Nk_B}\right). \tag{5.4}$$

Noting that $V/A = h$, the height of the cylinder, a simple expression is obtained

$$\Delta P = \frac{2F\Delta t}{5h}. \tag{5.5}$$

As stated above, F is known approximately from observational evidence. The period of the heating Δt is half the period of the oscillations; as an approximate average duration we take 10 seconds. Taking the height of the heating region as h = 2 km to match observations of thin pulsating auroras Eq. (5.5) gives $\Delta P = 10^{-4}$ Pa. This is well below the amplitude of typical observed signals of GAIW, which tend to have average amplitudes around 0.05 Pa. However, very thin thermalization heights have been observed in which $h < 1$ km; also, F is a rough estimate, and values as high as 30 egs/cm^{2}s have been described [55]. Furthermore, the presence of pulsating aurora associated with EPP doesn't necessarily preclude the presence of Joule heating due to electrojet arcs or other dynamic factors, so some coupling between GAIW sources may be present. More precise modeling regarding the role of EPP in GAIW generation is hampered by limited knowledge of ionospheric conditions during the process.

5.3 Motivation, Experimental Design, and Set-up

Referring to chapter 4 it is apparent that Lorentz forces, Ohm heating, and energetic precipitating particle momentum transfer might all contribute some energy to the generation of GAIW's. Unfortunately the ground-based sensors available to us offer little to disambiguate the relative importance of each process and even less to highlight the nature of any coupling between them. Of the three processes described, Lorentz forces have been shown to provide sufficient energy to produce infrasonic signals detectable on the ground. However, GAIW is sometimes received in which the sustained, high intensity current-like behavior expected for Lorentz force generation appears to be diminished or absent. In an effort to better understand the role of EPP in GAIW generation, an experiment was designed in which conditions similar to pulsating aurora were artificially stimulated in the lower ionospher.

In August 2012 an experiment was undertaken at Alaska's HAARP facility in an attempt to excite the lower ionosphere to induce high altitude infrasonic waves. Since during the experiment we expected to have direct knowledge of the source of the thermalization, we sought to gnereate HTV's free from the clutter and ambiguity inherent in geophysical observations. The experiment was undertaken as part of the Polar Aeronomy and Radio Science (PARS) summer student research program in which accepted student researchers are mentored by UAF faculty and HAARP staff and given access to the facility's Ionospheric Research Instrument (IRI) radio transmitter and diagnostic equipment. In the case of our experiment an infrasonic microphone array was deployed as an additional, primary diagnostic tool. The microphones recorded continuously throughout the campaign, collecting data during all of the students' various experiments. Most of the experiments other student groups spearheaded focused on ionospheric excitation at both too high an altitude and too high a frequency to produce perceptible infrasonic perturbations on the ground. Therefore, during the periods when the IRI operators were devoted to our experiment, the IRI parameters were set to specific conditions for lower ionospheric heating that should be expected to produce ionospheric infrasonic waves.

The primary instrument that we used at the HAARP facility to stimulate pressure disturbances in the upper atmosphere is the IRI. The IRI is a 12 x 15 element phased-array radio transmitter. Each array element is an 80-foot tall, broadband radio frequency transmitter designed to operate between 2.7 MHz and 10 MHz. The antennae are crossed dipoles; they may be polarized to linear, ordinary mode (o-mode), or extraordinary mode (x-mode). To avoid a lengthy digression to details of the Appleton-Hartree equation here we only make a brief statement about o-mode versus x-mode waves in the ionosphere. O-mode waves are plane-polarized waves with a dispersion relation that is the same as that for an unmagnetized plasma. X-mode waves have a more complicated dispersion relation and propagate with both transverse and longitudinal elements. For a detailed discussion on these wave forms refer to Yeh and Lui [16]. It has been shown that x-mode waves suffer considerable attenuation in the upper D and lower E regions of the ionosphere, particularly when plasma density is high. For delivering energy over a narrow altitude profile in the lower E region, x-mode transmission is the appropriate choice. We sought to target the lower E region between 90 – 110 km for heating. Referring to chapter 3 it is clear that radio absorption in the ionosphere is dependent upon frequency, plasma density, and collision rates. The lower E and D regions already possess high collision rates, and we can further ensure that the thermalization occurs in this region by choosing low frequency transmission. The plasma density is quite dynamic at high latitudes in this altitude range; the best chances for successful infrasonic generation are found when thin layers of dense plasma appear low in the ionosphere. For this reason we specifically sought to transmit the IRI while sporadic E-layer (E_s) plasmas were present overhead.

HAARP researchers have determined an approximate value of the energy flux delivered by the IRI as a function of alititude, frequency, and mode. Given an estimate of the energy flux we may use equation 5.5 to determine an approximate value for the pressure disturbance we may expect to generate. For example, transmitting at 3 MHz and given a heating time of 10 seconds and a height distribution of the thermalization of 10 km we find $\Delta P \approx 10^{-4}$ Pa. Importanty, during periods when E_s plasmas drift across the overhead zenith very thin vertical cross sections of high plasma density are sometimes observed wherein h is on the order of 1 km. Furthermore, longer heating periods may still be expected to produce detectable infrasound. Then under ideal conditions we may heat for (as an example) 25 seconds at 4 MHz a cross section of 1 km to produce $\Delta P \approx 0.05$ Pa. Even after considerable attenuation such a disturbance is well within the ability of our sensors to resolve. As such, the success of the experiment was heavily dependent upon favorable geophysical conditions.

On 4 August 2012, a four element infrasonic array was deployed on the HAARP facility. The microphones used were Chapparal Physics model 25 infrasonic microphones. These microphones have a flat response over a broad, low frequency range from 0.1-100 Hz and a sampling rate of 1000 Hz. Signals down to 0.01 Hz should still be discernible despite sensitivity roll off below 0.1 Hz. The fed the data to Chaparral digitizers that stored the data on a thumb drive. The microphones were arranged in a roughly 1.5 km side length centered triangle. Fig 5.1 shows the approximate locations for the microphone array elements relative to the HAARP facility roads and instruments as captured by Google Earth [56]. The array elements were entirely contained within the HAARP facility grounds with specific deployment positions chosen for accessibility, innocuousness, and protection from wind noise. Where possible the array elements were covered with rigid frame canvas tents for protection from elements, otherwise a tarp was erected above them. Thick foam housings covered the microphones for additional wind damping.

Fig 5.1 Position of microphones relative to HAARP's road network [56]. The side length of the outside triangle is approximately 1.5 km.

In order to test the efficacy of an infrasonic microphone, it is often instructive to collect data, perform a Fourier transform, and isolate the ubiquitous microbaroms to verify that the system is functioning properly. The PSD of one of the microphone elements is provided in Fig 5.2. The PSD is for microphone 3 on 8/9/2012 and was generated using Welch's method with a Hamming window of 8.33 minute duration per window and an 80% segment overlap. The solid lines show the upper and lower bounds for a 95% confidence interval. The microbarom surge is clearly visible centered below 0.2 Hz.

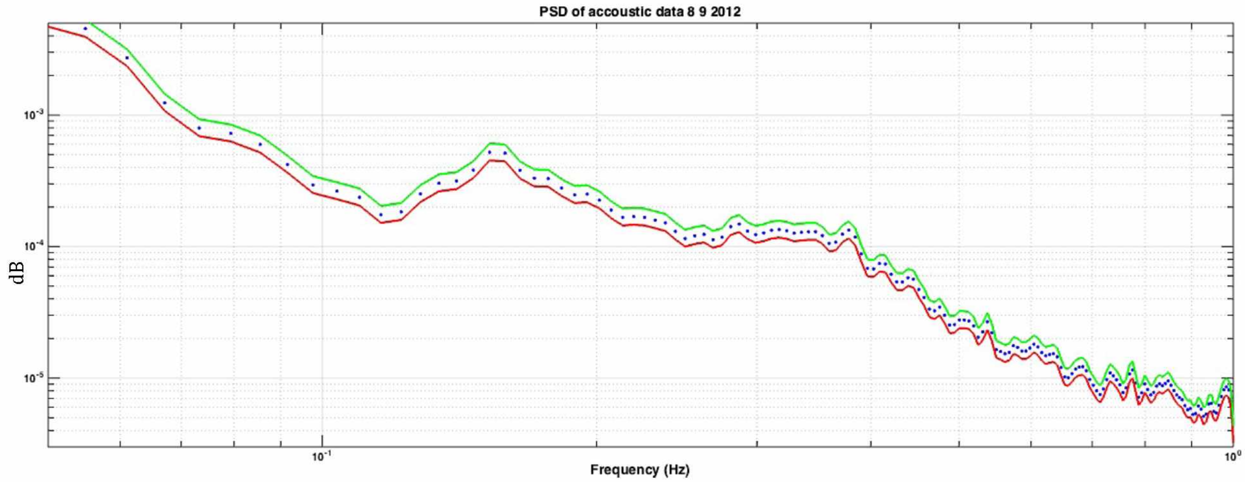

Fig 5.2 PSD of acoustic data for microphone 3 on 9 August, 2012. The broad band peak centered below 0.2 Hz is due to microbaroms. The PSD was generated using Welch's method with a Hamming window with 8.33 minute duration per window and an 80% segment overlap. The solid lines show the upper and lower bounds for a 95% confidence interval.

5.4 Results

The HAARP campaign for PARS 2012 ran from Aug 6-9. Over the course of the campaign the IRI was run throughout over many hours of each day. Our group directed the IRI operators on three separate occasions during the campaign on Aug 6, 8, and 9. In each case, our period of operation was about 20 mintues (sometimes transmission must be interrupted for aircraft fly-overs, etc.) in the neighborhood of local midnight as it had been noted that strong E_s had been sometimes occurring around this time.

Throughout the experiment the generators that power the IRI were clearly audible at all of the microphone sites. Furthermore the antennae themselves produce considerable noise that was audible at the microphones nearest the IRI. Figure 5.3 presents a spectrograph of upper infrasonic to lower audible acoustic frequencies over the course of an hour beginning 9 UT on 6 August 2012. The horizontal yellow lines correspond to acoustic signals from the generators and the IRI. It is apparent that the noises from these sources are confined to a series of very narrow pass band frequency ranges. Fig 5.4 illustrates the infrasound detection summary for this period. The data is band-pass filtered from 1-1.5 Hz with a window of 100 seconds and a 90% overlap.

In this pass band we note two periods in which we resolved signals originating from the facility generators located at a relative back azimuth of ~110^0.

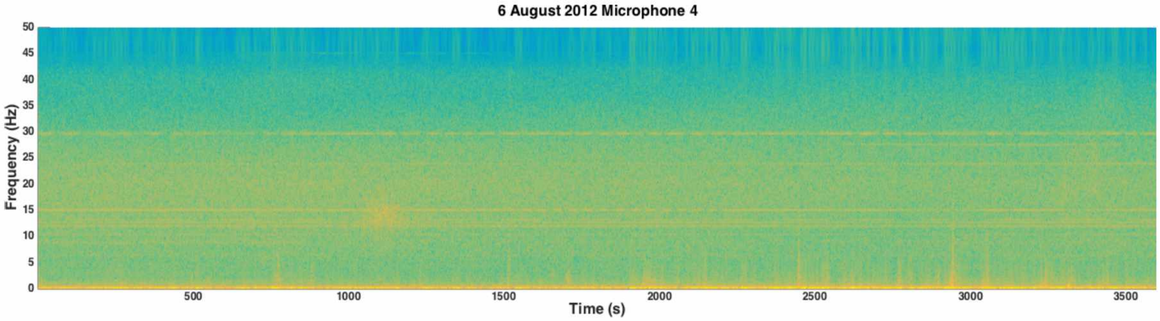

Fig 5.3 Spectrograph of HAARP acoustic data during 6 August 2012, beginning 9 UT. The data has been detrended and decimated to 100 Hz. The data is windowed into 10 second frames with an 80% overlap. The horizontal lines correspond to acoustic emissions from the IRI and generators.

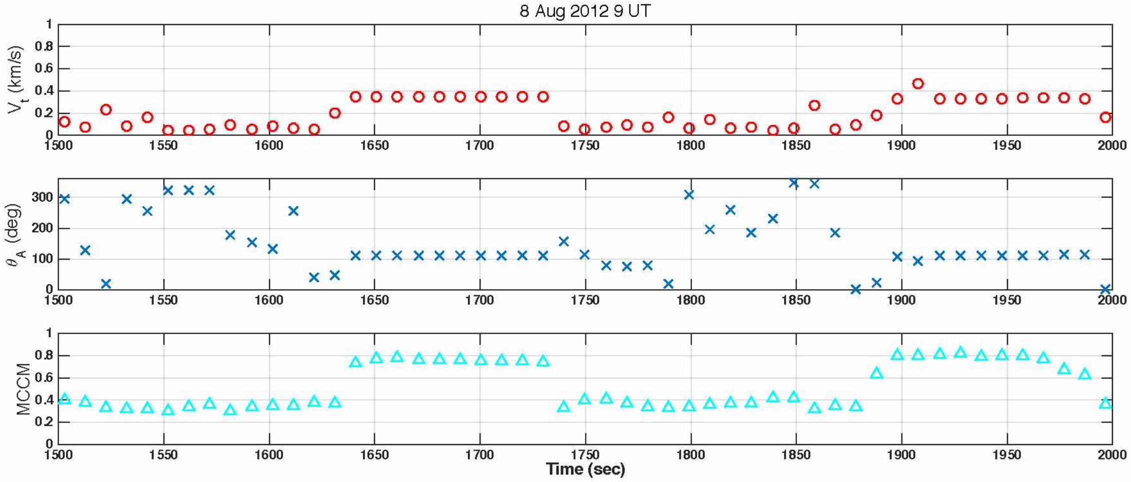

Fig 5.4 Signal detection summary for 6 August, 2012 hour 9 UT pass band 1 – 1.5 Hz. Here the data is band-pass filtered from 1-1.5 Hz with a window of 100 seconds and a 90% overlap. The signals with high MCCM have trace velocities consistent with a gound based source. The back azimuth points towards the generators.

In order to avoid contamination from the generators and IRI the data may be filtered into narrow frequency pass-bands where the contamination is not observed. As is apparent from figure 5.3

the infrasonic radiation from the generators is predominantly confined to a series of narrow frequency bands that may be avoided through filtering. Filtering to the pass band 0.015 – 0.2 Hz proved to be effective in avoiding this contamination while still allowing other signals to be detected. Of note is the narrow band emission around 15 Hz. During the fifteen minutes while our IRI parameters are transmitting (roughly 1200 – 2200 seconds) the 20 second heating intervals are clearly visible at this frequency as periodic blips in the yellow line.

Figure 5.5 displays the detection summary for 6 August, 2012 over the hour during which our IRI transmission occurred and in the pass band of interest. Here the least-squares approach was used with parameters for detection set similarly to those for optimum GIAW signals. Specifically, the data is band pass filtered to 0.015 – 0.2 Hz and a 8.33 minute (500 second) window with an 80% overlap is taken. Under these constraints, no well-correlated signals were received.

Figure 5.6 displays an ionogram for 6 August 2012. The ionogram is generated from an ionosonde on the HAARP facility. The graphic displays broadcast frequency versus altitude of peak reflection based on analysis of travel times. At low frequencies a strong, transient E_s plasma layer caused considerable reflection and suggested ideal conditions for heating of the lower E region. We chose to transmit at frequencies near Eo_s, and we modulated the frequency over the course of our 20 minutes of IRI transmission between 3 – 4.5 MHz.

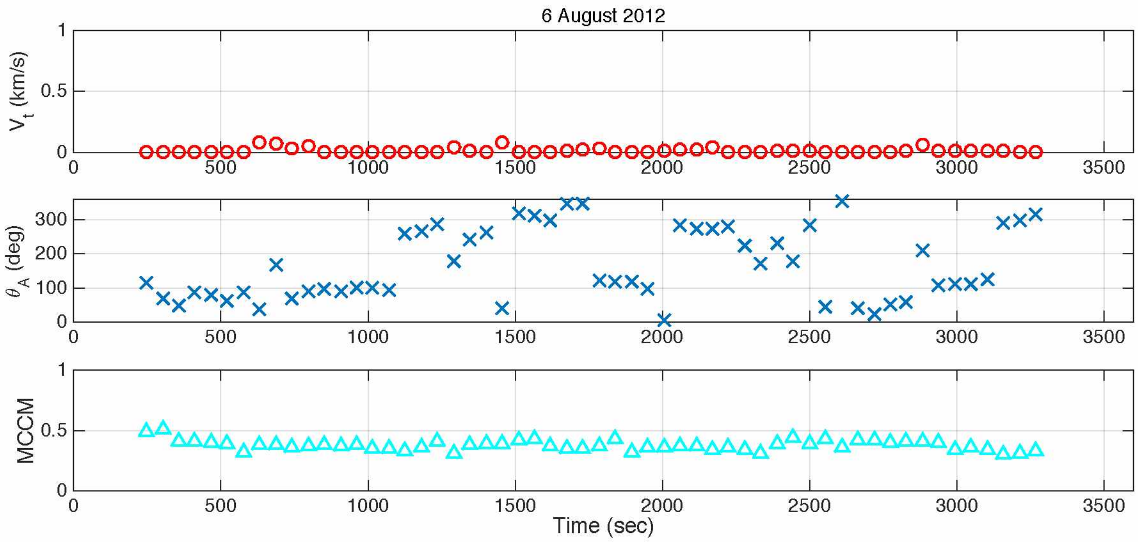

Fig 5.5 Signal detection summary for 6 August 2012, hour 9 UT passband 0.015 – 0.2 Hz. The data is band pass filtered from 0.015 to 0.2 Hz. The window is 8.33 minutes long with a 90% overlap. No well-correlated acoustic signals within this pass-band are apparent.

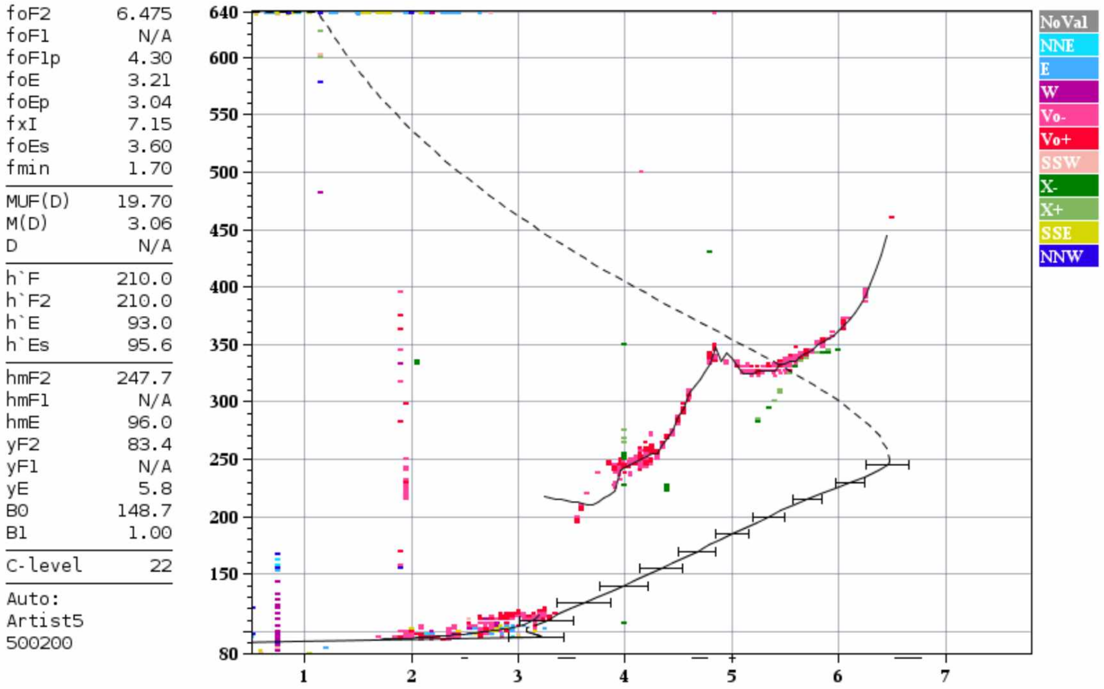

foF2	6.475
foF1	N/A
foF1p	4.30
foE	3.21
foEp	3.04
fxI	7.15
foEs	3.60
fmin	1.70
MUF(D)	19.70
M(D)	3.06
D	N/A
h\`F	210.0
h\`F2	210.0
h\`E	93.0
h\`Es	95.6
hmF2	247.7
hmF1	N/A
hmE	96.0
yF2	83.4
yF1	N/A
yE	5.8
B0	148.7
B1	1.00
C-level	22

Auto:
Artist5
500200

Fig 5.6 Ionogram from the HAARP facility ionosonde 6 August, 2012 9:24 UT. The pink horizontal structure in the lower left indicates strong reflection of radio waves up to ~ 3.5 MHz and suggests the presence of a strong E_s layer in the neighborhood of 100 km altitude.

In the field, after the first day's experiments were complete, we made our way to the sensors to recover the data and batteries for recharging. Preliminary investigations did not yield apparent HTV's. Filtering and studying the data from the individual microphones showed very little change in the waveforms during the period when we were attempting ionospheric heating. In fact at the very low infrasonic wavelengths, where we expected any HTV's to be apparent, there was very little correlation between sensors at all. Given the seemingly excellent conditions for infrasound generation on August 6, the lack of apparent signals necessitated adjustments in the experiment. Our next attempt to generate HTV's came on the night of 8 August 2012. We decided to try varying the duration of the heating pulses over our heating period under the assumption that 20 second heating pulses may produce too low frequency or low amplitude infrasonic perturbations for our microphones to resolve. Over the course of the 15 minutes that the IRI was running for our experiment we varied the duration of the heating pulses from 10 to 30 seconds.

Unfortunately during this experiment one of the data storage devices recording the data from the microphone digitizer reported a heavily corrupted file. Some possible causes for such a malfunction may be rainfall and high humidity causing physical damage or jostling loose of the thumb drive storage device during deployment or pick up. The upshot is that microphone 4 (the triangle's centered microphone) was not logging during the experiment. We retained a triangle of logging sensors adequate for resolving time delay of arrival analysis, however without the centered sensor the triangle has a much larger distance between elements, which is detrimental to resolving higher frequency (shorter wavelength) signals. It is worth mention that a minimum of four active sensors is necessary to determine a non-planar source location. The detection summary for the hour in which our transmission time occurred appears in Fig 5.7 with the same parameters as described for Fig 5.6. An ionogram appears in Fig 5.8, and we again note the presence of a dense E_s layer during our experiment.

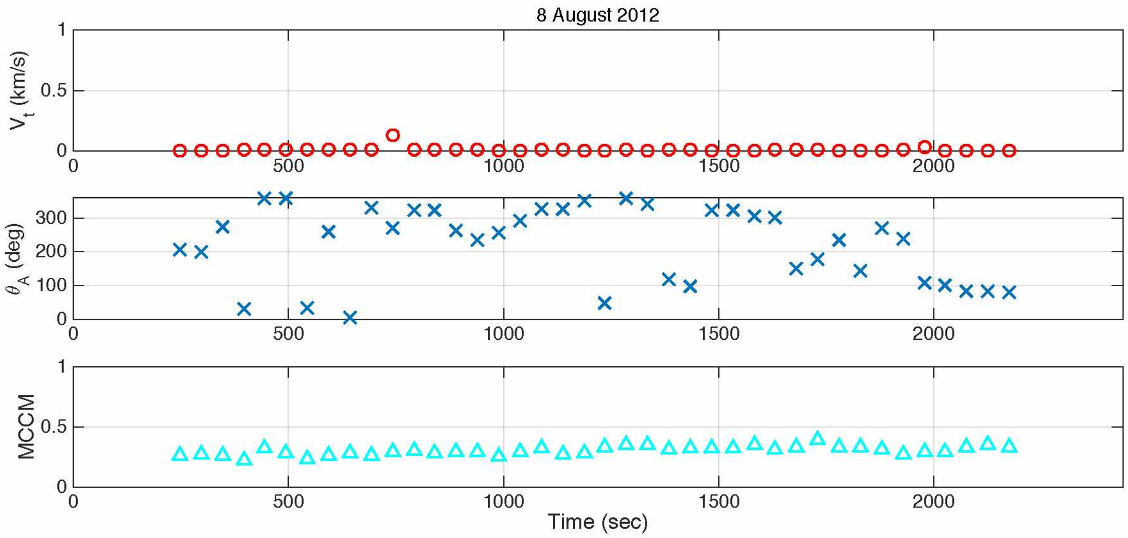

Fig 5.7 Signal detection summary for 8 August, 2012 9 - 10 UT. Throughout this chapter we present trace velocity, back azimuth, and MCCM for each signal summary. The data has been band pass filtered into 0.015 – 0.2 Hz and the window duration is 8.33 minutes. No well correlated infrasonic signals were received in this regime. Note that three of the four array elements reported data.

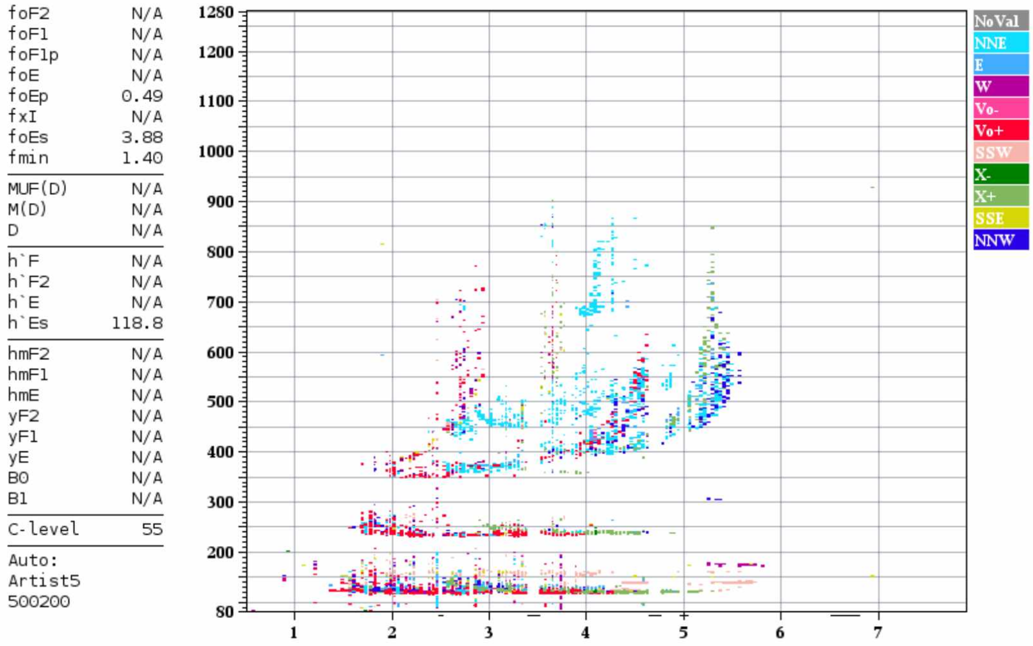

foF2	N/A
foF1	N/A
foF1p	N/A
foE	N/A
foEp	0.49
fxI	N/A
foEs	3.88
fmin	1.40
MUF(D)	N/A
M(D)	N/A
D	N/A
h\`F	N/A
h\`F2	N/A
h\`E	N/A
h\`Es	118.8
hmF2	N/A
hmF1	N/A
hmE	N/A
yF2	N/A
yF1	N/A
yE	N/A
B0	N/A
B1	N/A
C-level	55

Auto:
Artist5
500200

Figure 5.8 Ionogram for 8 August 2012. Dense E_s is evident during our experiment, suggesting good conditions for HTV generation.

Figure 5.7 displays the detection summary for signals in the 0.015 – 0.2 Hz range. Much like the summary for 6 Aug., no well-correlated signals were received in this frequency range. In fact, given the missing array element it is difficult even to resolve the high amplitude noise emitted from the generators at higher frequencies. Furthermore, there was considerable wind on the ground over the course of the evening, greatly increasing the signal to noise ratio. Despite this, it was again clear that adjustments in the IRI transmission strategy were in order.

We decided to try an approach in which the beam of radio transmission was swept across the overhead in the hopes that by moving the beam we would increase our likelihood of heating a particularly narrow plasma dense region. We arranged the angle from overhead to change at a rate such that the beam's intersection with a plane at 100 km would sweep back and forth at 400 km/s – just above the local sound speed. We expected that this dynamic heating approach would allow enough time for the beam to considerably enhance the temperature of a parcel of the *E* region ionosphere while also encouraging some current like behavior, particularly provided that a dense E_s layer appeared again. We sought to heat across a 100 km East – West intersection with a plane at 100 km altitude, so the half period of the beam's angular oscillations is (100 km)/(0.40 km/s) = 250 s. The area of the ionosphere heated by the IRI is on the order of 10 km^2, so we expect an area overhead to be heated for some 25 seconds while the beam passes by.

Figure 5.9 displays the detection summary for 9 August 2012. The parameters for signal detection are the same as the examples above – band pass filtered to 0.015 – 0.2 Hz with an 8.33 minute window. Unlike the above figures, this detection summary is for hours 8 – 10 UT. Figure 5.10 demonstrates an associated ionogram taken at 9:36 UT; E_s is clearly present. We note several periods of active infrasonic signal detection, most notably around 8:40 – 8:55 UT and again from around 9:15 – 10 UT. A particularly interesting period shows consistent HTV's beginning at ~5500 seconds (9:32 UT).

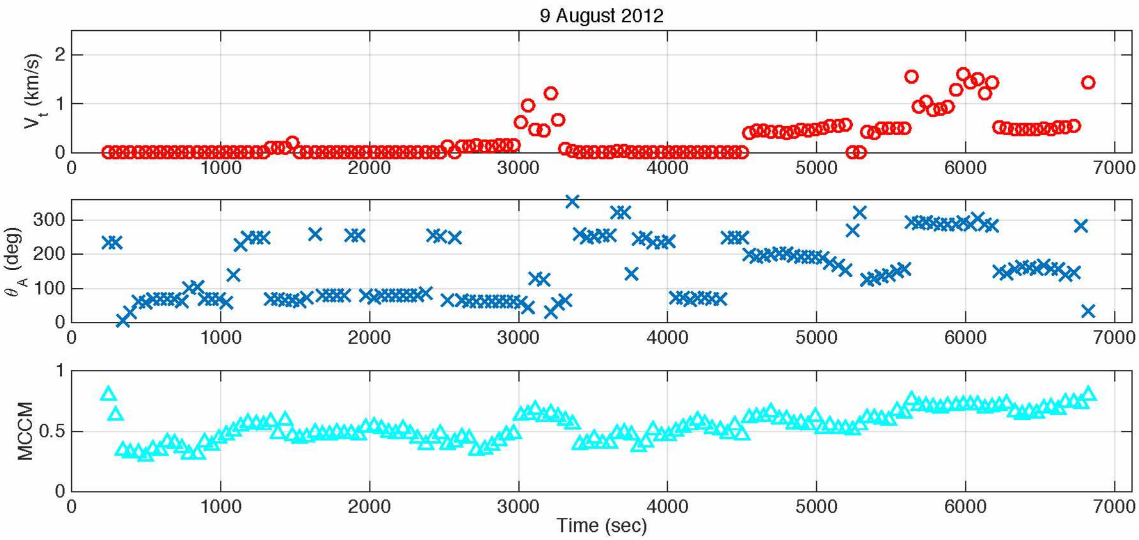

Fig 5.9. Detection summary for 9 August 2012 8 – 10 UT. The data has been band pass filtered into 0.015 – 0.2 Hz and the window taken is 8.33 minutes with a 90% overlap. Both ground based sources and HTV's are present in this regime.

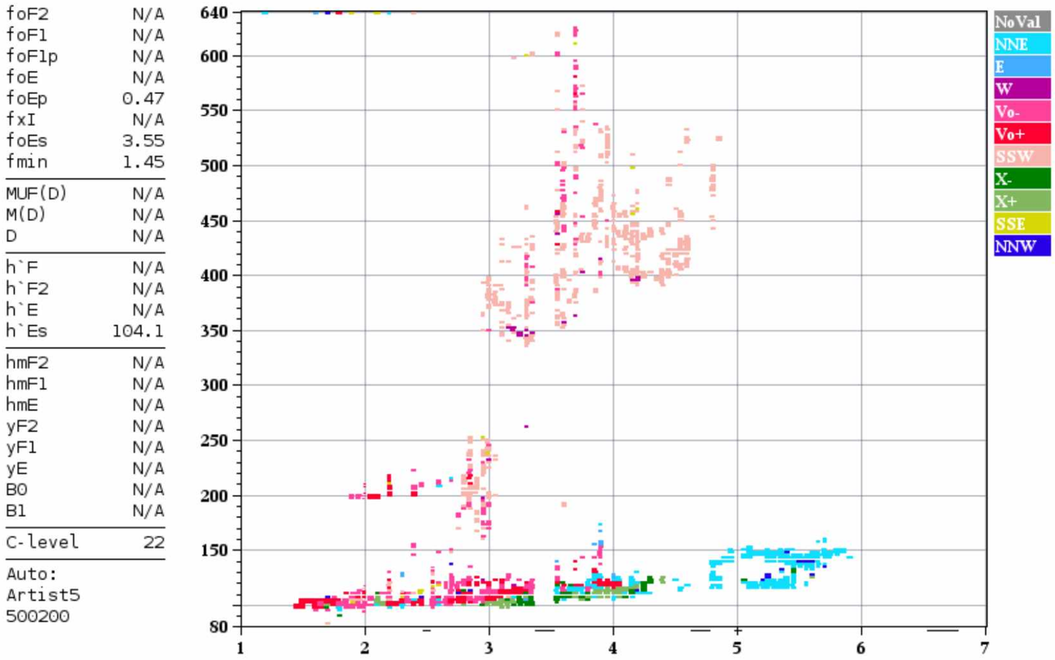

Fig 5.10. Ionogram from the HAARP facility ionosonde 9 August, 2012 9:36 UT. The pink horizontal structure in the lower left indicates strong reflection of radio waves up to ~ 3.5 MHz and suggests the presence of a strong E_s layer in the neighborhood of 100 km altitude.

Our particular IRI transmission time coincides roughly with the period of HTV reception as we were scheduled for 15 minutes of IRI operation late in the 9'th hour UT. This period shows by far the most potential for demonstrating ionospheric sources of infrasound. Unfortunately, much as was the case for 8 Aug 2012, when we collected the data storage devices from the digitizers, one of them reported corrupted and missing data. The number 3 microphone (lower left in Fig 5.1) is therefore excluded from the analysis.

The loss of an array element had a strong impact on the interpretation of the signals received. It immediately explains the preponderance of signals with 2 km/s < V_t < 0.5 km/s. With the missing array element the remaining elements form an obtuse triangle with the obtuse angle over 130^0. Such an array is limited in its ability to resolve the trace velocity and back azimuth of a signal. The signals displaying a trace velocity of up to 0.5 km/s are interpreted as originating on the ground. The back azimuth for these signals generally points to around 150^0, which is near the generator. It is apparent that in this case signals originating from the generator are too close to satisfy the least-squares method's planarity assumption, and the compromised array is consistently over or under estimating the trace velocity of a ground based source.

The signals satisfying $V_t >$ 0.5 km/s appear to be true HTV's that are not easily attributed to a ground based source. Window closing procedures found that some of the ground-based sources could be removed by filtering to the pass band 0.015 – 0.05 Hz and reducing the duration of the windows to 5 minutes. Figure 5.11 displays the resulting detection summary for ~9:30 – 9:53 UT. Under these parameters some interesting trends begin to emerge.

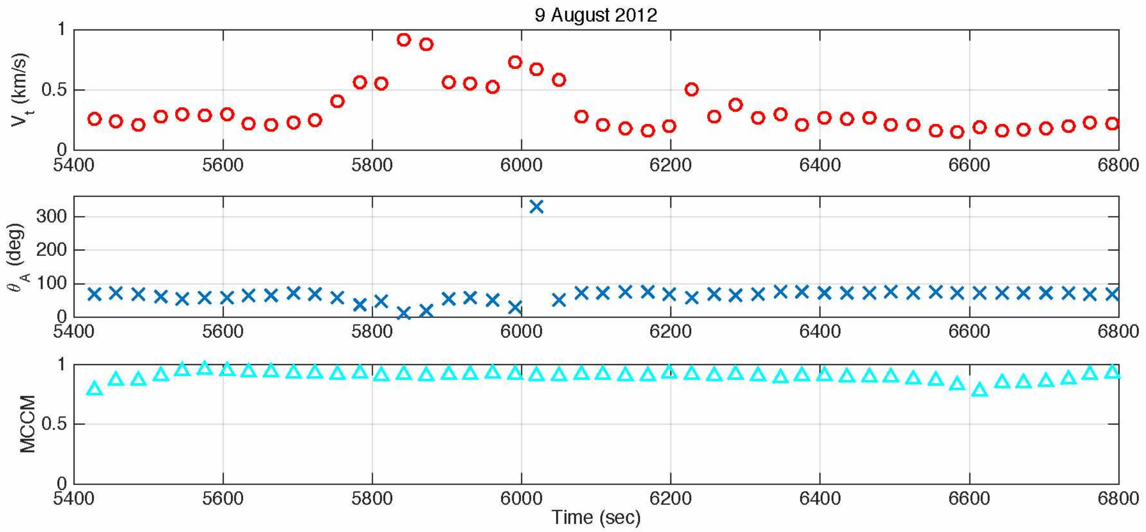

Fig 5.11. Detection summary for the HTV's observed on 9 August, 2012. The HTV's were received between 5400 and 6800 seconds (9:30 – 9:53 UT). Here the data has been band pass filtered to 0.015 – 0.05 Hz and windowed into 5minute segments with a 90 % overlap.

Between 5700 and 6100 seconds there is a particularly well defined increase to high trace velocity in V_t that has a duration of roughly 250 seconds. It is encouraging that this is quite close to the periodicity of the sweeps of the IRI's beam across the sky. Furthermore, a periodicity in trace velocity is in keeping with intuition; when the source is directly overhead the trace velocity is expected to be highest and when the source is at its greatest distance from the zenith a minimum in V_t should appear.

The two peaks in V_t correspond to zenith crossings in θ_A. Generally speaking the HTV's were assessed as being within 60^0 of due North. We had arranged for the radio beam to sweep across the sky directly overhead in an East – West direction. Since the IRI is just South of the array, it is uncertain why the signals should arrive from the North. It should be noted, however, that the IRI was around 1 km from the center of the array, while the heating region was presumed to be at least 100 km distant overhead. There is considerable room for atmospheric dynamics to influence the signal before it reaches the sensors, and the slight distance to the South of the IRI is comparatively negligible.

It is also counterintuitive that the maximum in V_t should consistently coincide with the Westernmost value for θ_A. Initially one would presume that the minima in V_t would occur when the values for θ_A reached either their Eastern or Western most point as should be the case for a source crossing the overhead zenith along the East-West line. Conversely the trajectory for a source that is consistent with the trace velocity and back azimuth we found would need to have a considerable North-South travel component.

Given the obtuse-triangular array we ended up with, there is considerable error expected in V_t and even greater uncertainty in θ_A, particularly when the source is near the overhead zenith. For instance, using the methods of ascertaining uncertainties discussed in Chapter 2, given an impulsive source with a center frequency of 0.03 Hz arriving from the North with trace velocity 0.35 km/s the 90% confidence limits in θ_A are 353^0 – 7^0. For the same signal with V_t = 1.5 km/s the 90% confidence limits in θ_A are 328^0 – 25^0. Given such large uncertainties in the measurements it's remarkable that a systematic pattern emerged at all.

Throughout the campaign at no times outside of 8 – 10 UT on 9 August 2012 did a persistent period of HTV's appear. It should be noted that a systematic approach to window closing was utilized for all of the data collected during the campaign and many ground based sources appeared in various pass bands and window durations, which confirms that the array was properly functioning. However, the only HTV's with high MCCM and reasonable planarity are those that occurred late in the 9 UT hour on August 9.

5.5 Discussion

Throughout the PARS campaign the geophysical conditions presumed to be required for ionospheric based infrasound to be generated were consistently present, both during our time directing the IRI and during the IRI's operating times in general. E_S was present frequently in the neighborhood of local midnight and likely presented thin, dense plasma layers appropriate for heating. The wind was relatively calm, enough so that well correlated signals with amplitudes as low as 0.025 pa could be resolved. Nevertheless, very few HTV's were observed during the campaign.

The most significant HTV's that appeared throughout the campaign were two strongly correlated signals that were received at 9:38 and 9:41 UT on 9 August 2012. Figure 5.12 diplays the pressure time series recorded by the three active microphones over that period. The signals are low amplitude but very well correlated, particularly over the time periods of 5800 – 5900 seconds and 6000 – 6100 seconds. These signals did occur during the period in which we were directing the IRI operation a warrant some analysis. When these signals were received the IRI was sweeping the beam across the sky overhead. The half period of these sweeps was 250 seconds. The pressure time series during this period is displayed in Fig 5.12. Comparing that to the pressure series below, we note that the entire period over which the well-correlated signals were received was approximately 400 seconds. It would not be unreasonable to receive a somewhat longer duration signal for a source moving across the sky at 100 km altitude, as coupling with gravity waves and refraction effects tend to increase the duration of the signal.

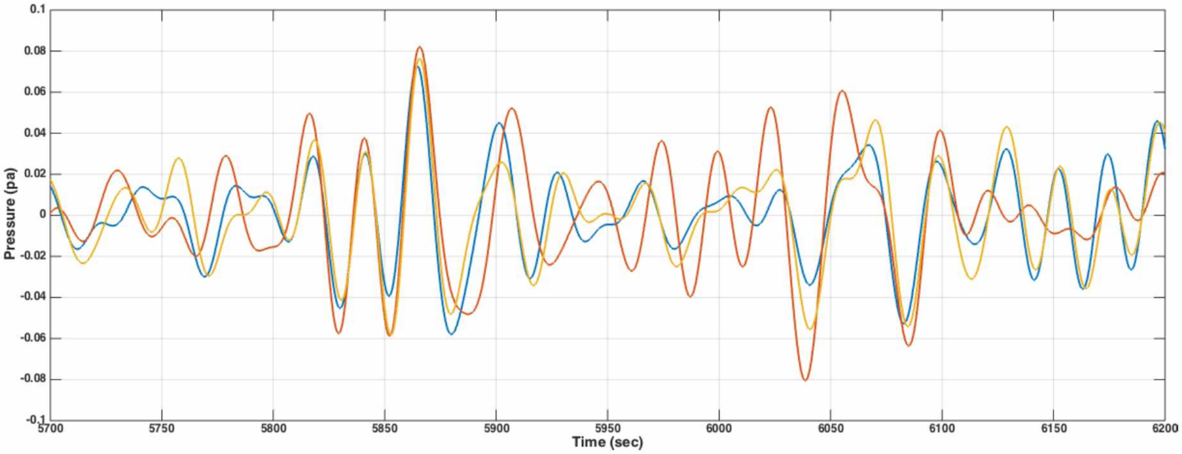

Fig 5.12. High trace velocity signal acoustic waveforms. The pressure series for the three array elements during the HTV period on 9 August 2012 is overlayed. The well-correlated signals are clearly visible with peak amplitudes around 5875 s and 6075 s.

The period of the oscillations in the pressure series increase over the course of the signal received. As was discussed in chapter 2, at such low frequencies some coupling with internal gravity waves must be assumed, which can cause an increase in the period of oscillations in the tail of a signal. However, another possibility might be considered for this particular signal. For a source moving rapidly across the overhead zenith a Doppler shift is to be expected. Unfortunately, an exact time series of the IRI sweeps is not available for comparison.

Throughout the 20 minutes that the IRI was devoted to E region ionospheric heating on August 9, less than 7 minutes showed discernible HTV's. Since a pattern of repeated signals appearing with similar periodicity to the IRI sweeps overhead failed to appear, other possible sources of the HTV's should be considered. Generally speaking, MAW's and other turbulent wind noises exhibit longer signal duration and higher frequency content respectively than what we observed. However, the pressure wave-forms are qualitatively very similar to what is observed following an overhead passage of an auroral electrojet. While geomagnetic conditions were very quiet during most of the PARS campaign, a low amplitude geomagnetic disturbance was recorded by the on-site magnetometer around the time that the HTV in question was received. Figure 5.13 displays the magnetic field components. There is a bay in the Z and H components of the magnetic field beginning shortly before the HTV's were received.

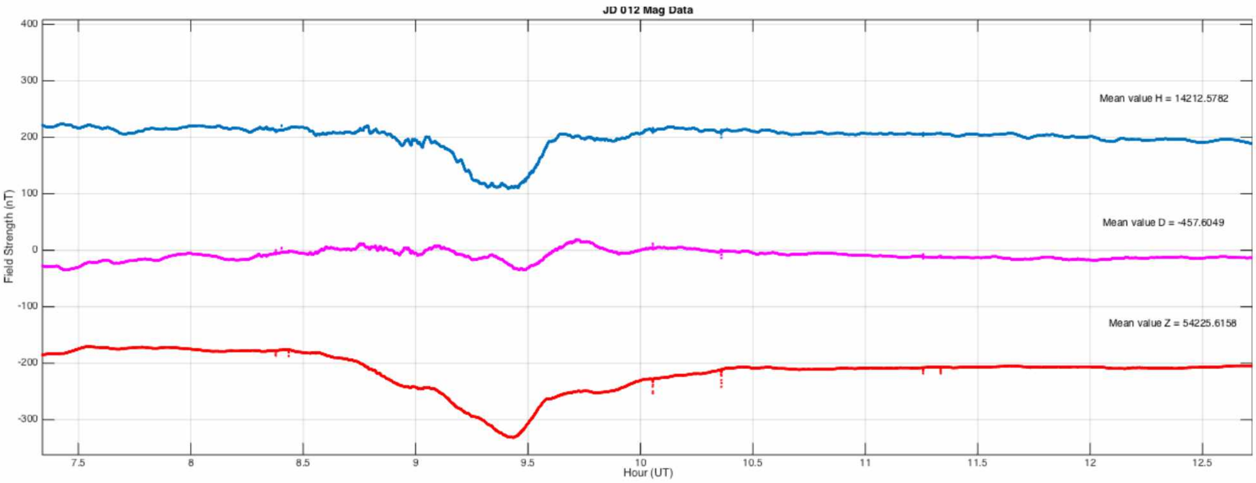

Fig 5.13. Magnetometer conditions for Aug 9 2012 taken at the HAARP facility. Note an approximately 100 nT disturbance between 9:00 and 9:40 UT. The total disturbance peaked at 9:24 UT.

It is unusual for an isolated disturbance of such low amplitude to produce infrasonic signals that are received on the ground, but examples do exist (see section 4.3). However, the magnetometer conditions are consistent with a filament of electrojet current crossing the overhead zenith. The

HTV's were received between 9:38 and 9:41 UT, while the peak in the magnetic disturbance occurred at 9:24 UT. The typical travel time for an E region generated HTV is between 5 and 6 minutes. The magnetic disturbance did not return to quiet day values until after 9:40 UT, so the time frame definitely allows for the HTV's to be associated with this low amplitude geomagnetic bay. In chapter 4 it was noted that the lowest amplitude geomagnetic disturbances to be unambiguously identified as concurrent with auroral infrasound were in the range of 100 nT. If the HTV's observed on Aug 9 are related to such a small perturbation in the magnetic field, then they represent an unusual, but not unheard of, occurrence.

HTV's could also be produced by sources very near or within the array itself. This is particularly the case for an oblique, three-element array. However, the wavelengths of the HTV's in question are kilometers long. The only apparent sources that could generate such large-scale disturbances near the HAARP ground are the generators for the IRI. Throughout the experiment the generators were continually recorded at low frequencies. The array consistently misplaced the back azimuth at around 80^0 as opposed to $\sim 110^0$, but this is easily understood as a result of the source being too near-field to be treated as a plane wave. During the HTV events the back azimuth shifted to roughly due North, or 0^0. It is difficult to understand why the HTV's would show a consistent source to the North if the true source is the generators, particularly since a discrepancy of 80^0 is outside of a very high confidence level for the back azimuth estimate, even for high trace velocity signals and the compromised array.

Given the high trace velocities, very low frequencies and long, well correlated waveforms, and consistent back azimuths of the signals in question, it is the judgment of the author that they most likely represent high altitude generated infrasound. Unfortunately, there is no apparent diagnostic tool available to disambiguate the experimental ionospheric heating and the naturally occurring electrojet filament. The high uncertainties associated with the compromised array further complicate strategies to identify an ionospheric source. The only HTV's generated occurred during a period and in a pass band where considerable contamination from ground-based sources were present. Therefore, no unambiguous IRI generated HTV's are reported from the PARS campaign 2012.

Given what were presumed to be excellent geomagnetic conditions throughout the campaign, the absence of well-defined infrasonic HTV's suggests a few possibilities. One possibility is that the sensor elements and array design were not sufficiently sensitive to resolve any signals that may have been generated. However, ground-based signals with kilometer scale wavelengths and amplitudes of less than 0.1 Pa peak-to-peak were resolved with excellent inter-sensor correlation. This demonstrates array sensitivity and functionality within the parameters we expected to generate. Another possibility is that conditions in the atmosphere between the ground and 100 km included strong winds or other dynamic factors that dispersed or refracted away any infrasound generated. Precise conditions throughout the lower atmosphere to 100 km altitude are unknown.

The most important possibility to consider is that sufficient over-pressure wasn't achieved in the ionosphere to generate propagating acoustic disturbances capable of traversing the distance to the ground. Since the transmitted power delivered by the IRI is known theoretically, failure to produce HTV's suggests that either the altitudinal cross-section of the heating region or the attenuation of the resulting acoustic wave is greater than expected. While some attenuation due to geometric spreading must be taken into account, the horizontal extent of the heating region is cited as being at least some tens of kilometers, so an observer directly underneath would expect to record a plane wave with little spreading. We restricted our experimental parameters to generate signals at very low frequencies in which absorption is minimized. All of these considerations anecdotally suggest that sufficiently narrow heating profiles were not obtained.

5.6 Experimental Conclusions

We have attempted to generate HTV's similar to GAIW by inducing ionospheric heating qualitatively similar to that observed during EPP events. The only such HTV's observed during the experimental campaign came shortly after a low-amplitude geomagnetic disturbance during a period of considerable contamination from a ground-based source and can not be unambiguously attributed to IRI heating. The experiment was conducted during presumably ideal geophysical conditions; the failure to generate and observe HTV's likely suggests that a sufficiently narrow profile for heating was not realized.

The apparent absence of HTV's generated by the IRI during the HAARP experiment does not rule out heating and direct bombardment from EPP as a source of potential infrasonic radiation. However, we have yet to find conclusive evidence that EPP may play a primary role in generating the observed HTV's. By contrast conditions associated with dynamic auroral electrojet arcs were virtually ubiquitous in the GAIW events considered. While counter examples exist in which HTV's with the parameter distinctions of GAIW occurred in the absence of observable electrojet arcs, the PFIR data has shown that arc-like ribbons of heightened conductivity sometimes appear with a minimum of **B** field disturbances, yet GAIW is present. These considerations lead us to propose that most of the observed infrasound that has been classified as GAIW has been excited by **J x B** forces and Joule heating due to current-like behavior in auroral electrojet arcs and dynamic regions of heightened conductivity.

As a final note, the experimental results suggest a potential line of future research. Larquie et al. applied modern computational methods to model infrasound generated by EPP and concluded that the resulting infrasonic perturbations received on the ground are expected to be smaller than the observed infrasound by around a factor of two [12]. They conjectured that in the presence of an electrojet filament EPP could modulate the electrojet and cause enhanced infrasound signals as a result. Since HTV's were observed during the experiment only when both periodic heating from the IRI and an electrojet filament were presumed to coincide, the idea of a pulse modulated electrojet current as a primary source of GAIW production remains encouraging. As such, a comprehensive model of pulse modulated electrojet currents should be goal of continued research. Future experiments at the HAARP facility seeking to isolate these conditions could also be pursued.

Chapter 6

Conclusions and Closing Remarks

6.1 Conclusions

In chapter 1 we motivated the research presented here by the following two questions:

1. *Can we quantify conditions that are necessary and/or sufficient for the classification and generation of GAIW?*

2. *From these conditions, what are the ramifications on the mechanisms of GAIW generation?*

In addressing the first question, a systematic documentation was made regarding the conditions present during 63 exemplary and unambiguous GAIW events, with concurrent HTV's and geomagnetic perturbations as selection criteria. We found that irregular oscillations of the H component of the **B** field were present in all cases and that they followed predictable spectral characteristics. We developed a unique approach to analyzing imaging riometer data and generated cosmic noise absorption keograms for comparison against acoustic and geomagnetic data. Our riometer measurements found high conductivity patches passing supersonically overhead in all instances that riometer data was available. We propose that these $\mathbf{B}_H$ oscillations, alongside dynamic regions of heightened conductivity are necessary for the generation of GAIW. We observed a consistent westward-drifting trend in our estimates of GAIW back azimuth and developed a simple model of a stationary ionospheric source to explain this trend. Fitting our observations to this model suggests that the high trace velocity signals associated with the analyzed GAIW events were grouped about an extended, stationary source region some 60^0 longitude east of the anti-sun-earth line and situated at an average latitude of 77^0. This supports a source region consistent with the auroral post midnight sector. We propose that extended periods of HTV's concurrent with the above diagnostic criterion represent sufficient conditions to classify GAIW events. We therefore conclude that the first research question has been addressed, and conditions that are sufficient and or necessary for GAIW generation have been catalogued.

In addressing the second research question, it was found that supersonic zenith crossings of high conductivity regions occurred regularly in all cases that the Poker Flat Imaging Riometer was online. Furthermore, the direction of the geomagnetic total horizontal disturbance vector tended towards parallel with the acoustic signal back azimuth. We have shown that heightened acoustic pressure signals are frequently observed following the overhead passage of a high conductivity arc. We suggest that such signals may be understood as bow waves generated by supersonic motion of auroral electrojets. We also noted GAIW were frequently observed in the absence of clearly defined auroral arcs, particularly in the post midnight sector where diffuse aurora was present. We undertook an experimental campaign at the HAARP facility in 2012 in an effort to generate ionospheric infrasound waves similar to those that may be generated by diffuse aurora forms during energetic particle precipitation into the lower ionosphere. Despite experimental efforts, no evidence was secured to suggest energetic particle precipitation plays a primary role in GAIW production. We propose that much of the observed high trace velocity infrasound is usually best understood as originating in the lower ionosphere and being generated by dynamic electro-jet currents associated with high conductivity regions. Coupling with acoustic gravity waves, refraction and reflection in the stratified atmosphere, and complex, oscillatory motion of the electrojet may all contribute to broadening individual pressure waves into persistent, irregular wave trains. Modulation of auroral electrojet currents due to periodic heating from energetic precipitating particles also remains a plausible source mechanism during GAIW events.

6.2 Recommendations for Further Research

Despite efforts by researchers spanning decades, many open questions regarding auroral infrasound persist. From a theoretical standpoint, a single, well-formulated model that predicts the infrasonic waveforms observed remains elusive. Based on our findings we recommend pursuing a physical model that encompasses both dynamic auroral electrojet currents as well as thermalization due to energetic particle precipitation. In particular, the pressure perturbations resulting from an electrojet current modulated by periodic heating due to EPP should be explored. Given encouraging predictions from such a model, experiments might then be designed at a facility such as HAARP to generate similar conditions for comparison.

While there has been some progress made in automating the identification of GAIW signals in infrasonic time series there remains ample opportunity for enhancement of such methods. Our results suggest that the parameter space used for current identification algorithms may need to be expanded. An enhanced method for automated disambiguation of isolated AIW signals, MAW, and other clutter from GAIW utilizing the parameter space findings from this research is also recommended as a goal further progress.

Selected abbreviations

AIW	-	Auroral infrasound waves
CTBTO	-	Preparatory commission for the comprehensive test ban treaty organization
CTBT	-	Comprehensive test ban treaty
IMS	-	International monitoring system
HTV	-	High trace velocity signal
GAIW	-	Geomagnetic auroral infrasound waves
MAW	-	Mountain associated waves
EPP	-	Energetic particle precipitation
HAARP	-	High frequency active auroral research program
PARS	-	Polar aeronomy and radio science
IRI	-	Ionosphere research instrument

References

[1] Chrzanowski, Peter, Gary Greene, K. T. Lemmon, and J. M. Young. "Traveling Pressure Waves Associated with Geomagnetic Activity." J. Geophys. Res. **66**, 11, (1961).

[2] Wilson, Charles R. "Infrasonic Pressure Waves from the Aurora: A Shock Wave Model." Nature **216**, 5111, (1967).

[3] Wilson, Charles R., and Sue Nichparenko. "Infrasonic Waves and Auroral Activity." Nature **214**, 5095, (1967).

[4] Swift, Daniel W. "The Generation of Infrasonic Waves by Auroral Electrojets." J. Geophys. Res. **78**, 34, (1973).

[5] Chimonas, G. "Infrasonic Waves from Auroral Arcs." J. Geophys. Res. **82**, 25, (1977).

[6] Wilson, Charles R. "Infrasonic Waves from Moving Auroral Electrojets." Planet. Space Sci. **17**, 6, (1969).

[7] Wilson, Charles R. "Auroral Infrasonic and Ionospheric Absorption Substorms." J. Atmos. Terr. Phys. **32**, 3, (1970).

[8] Wilson, Charles E., and John K. Hargreaves. "The Motions of Peaks in Ionospheric Auroral Absorption and Auroral Infrasonic Waves." J. Atmos. Terr. Phys. **36**, 9, (1974).

[9] Wilson, Charles R. "Auroral Infrasonic Waves." J. Geophys. Res. **74**, 7, (1969).

[10] Wilson, Charles R., John V. Olson, and Hans C. Stenbaek-Nielsen. "High Trace-velocity Infrasound from Pulsating Auroras at Fairbanks, Alaska." Geophys. Res. Lett. **32**, 14, (2005).

[11] Wilson, C. R., J. V. Olson "Frequency domain coherence between high trave-velocity signals at I53US and video data from pulsating aurora." Inframatics **9**, 27-30. (2005).

[12] Larquier, Sebastien De, Victor P. Pasko, Hans C. Stenbaek-Nielsen, Charles R. Wilson, and John V. Olson. "Finite-difference Time-domain Modeling of Infrasound from Pulsating Auroras and Comparison with Recent Observations." Geophys. Res. Lett. **37**, 6, (2010).

[13] Lee, Dong-Chang. *Neural Network Approach to Classification of Infrasound Signals*. Diss. University of Alaska Fairbanks, 2010.

[14] Wilson, C.R., J.J. Oldham, J.V. Olson, C.A. Szuberla, Auroral Infrasound and Associated Cosmic Noise Absorption Events at I53US, Inframatics **27**, 2-10, (2010).

[15] Hedin, A. E. "MSIS-E-90 Atmosphere Model." Goddard Space Flight Center, n.d. Web. 02 Sept. 2014. <http://omniweb.gsfc.nasa.gov/vitmo/msis_vitmo.html>.

[16] Yeh, K. C., and C. H. Liu. *Theory of Ionospheric Waves*. New York: Academic, (1972).

[17] Johnson, C. Y. "Ion and neutral composition of the ionosphere." Ann. IQSY **5**. (1969).

[18] Bilitza, D. "International Reference Ionosphere - IRI-2007." Goddard Space Flight Center, n.d. Web. 10 Oct. 2014. <http://ccmc.gsfc.nasa.gov/modelweb/ionos/iri.htm>

[19] Kelley, Michael C., and Rodney A. Heelis. *The Earth's Ionosphere: Plasma Physics and Electrodynamics*. San Diego: Academic, 1989.

[20] Chimonas, G., and W.r. Peltier. "The Bow Wave Generated by an Auroral Arc in Supersonic Motion." Planetary and Space Science **18**, 4, (1970).

[21] Cushman-Roisin, Benoit. *Introduction to Geophysical Fluid Dynamics*. Englewood Cliffs, NJ: Prentice Hall, 1994.

[22] Butkov, Eugene. *Mathematical Physics*. Reading, MA: Addison-Wesley Pub. 1968.

[23] Sutherland, Louis C., and Henry E. Bass. "Atmospheric Absorption in the Atmosphere up to 160 Km." J. Acoust. Soc. Am. **115**, 3, (2004).

[24] Pierce, Allan D. "Propagation of Acoustic-Gravity Waves from a Small Source above the Ground in an Isothermal Atmosphere." J. Acoust. Soc. Am. **35**, 11, (1963).

[25] Mikhailenko, B. G., A. A. Mikhailov, and G. V. Reshetova. "Numerical Simulation of Acoustic-Gravity Waves Propagation in a Heterogeneous Earth-Atmosphere Model with Wind in the Atmosphere." *JAMP* **01**, 04, (2013).

[26] Bristow, W.A., R.A. Greenwald, and J.P. Villain. "On the Seasonal Dependence of Medium-scale Atmospheric Gravity Waves in the Upper Atmosphere at High Latitudes." J .Geophys. Res: Space Physics (1996).

[27] Lighthill, M. J. *Waves in Fluids*. Cambridge: Cambridge UP, 1978.

[28] Yeh, K. C., and C. H. Liu. "Acoustic-gravity Waves in the Upper Atmosphere." Rev. Geophys. **12**, 2, (1974).

[29] Jensen, Finn Bruun. *Computational Ocean Acoustics*. Woodbury, NY: American Institute of Physics, 1993.

[30] Song, Yang, Chen Zhou, Zhengyu Zhao, and Yuannong Zhang. "Ray Tracing of Acoustic Wave in the Lossy Atmosphere." J. Acoust. Soc. Am. **131**, 4, (2012).

[31] Bass, H. E. "Atmospheric Absorption of Sound: Further Developments." J. Acoust. Soc. Am. **97**, 1, (1995).

[32] Szuberla, Curt A. L., and John V. Olson. "Uncertainties Associated with Parameter Estimation in Atmospheric Infrasound Arrays." J. Acoust. Soc. Am. **115**, 1, (2004).

[33] Dirac, Paul A. M. *The Principles of Quantum Mechanics*, 4th ed. Oxford: Clarendon, 1958.

[34] Rao, C. R. *Linear Statistical Interference and Its Applications*, 2nd ed. Wiley Series in Probability and Mathematical Statistics. New York: Wiley, 1973.

[35] Pichon, Alexis Le, Elisabeth Blanc, and Alain Hauchecorne. *Infrasound Monitoring for Atmospheric Studies*. Dordrecht: Springer, 2010.

[36] Chimonas, G., and C. O. Hines. "Atmospheric Gravity Waves Launched by Auroral Currents." The Upper Atmosphere in Motion, AGU. Washington D.C. 1974.

[37] Lee, Dong-Chang, John V. Olson, and Curt A. L. Szuberla. "Computationally Robust and Noise Resistant Numerical Detector for the Detection of Atmospheric Infrasound." J. Acoust. Soc. Am. **134**, 1, (2013).

[38] Havelock, David Ian, Sonoko Kuwano, and Michael Vorländer. *Handbook of Signal Processing in Acoustics*. New York, NY: Springer, 2008.

[39] *Interview of Harold Leinbach by Brian Shoemaker*. The Ohio State University, n.d. Web. 20 Oct. 2015. < http://kb.osu.edu/dspace/handle/1811/34863>

[40] *The 1978 Nobel Prize in Physics*. The Royal Swedish Academy of Sciences, 2015. Web. 07 Dec. 2015. <http://www.nobelprize.org/nobel_prizes/physics/laureates/1978/press.html>

[41] Huba, J. D. *2013 NRL Plasma Formulary*. Washington, DC: Naval Research Laboratory, 2013.

[42] Murayama, Yasuhiro, Hirotaka Mori, Shoji Kainuma, Mamoru Ishii, Ichizo Nishimuta, Kiyoshi Igarashi, Hisao Yamagishi, and Masonori Nishino. "Development of a High-resolution Imaging Riometer for the Middle and Upper Atmosphere Observation Program at Poker Flat, Alaska." J. Atmos. Sol.-Terr. Phys. **59**, 8, (1997).

[43] *Geophysical Institute Magnetometer Array (GIMA) Instruments*. UAF Alaska Satellite Facility, 2015. Web. 10 Aug. 2014. <https://www.asf.alaska.edu/magnetometer/about-aurora-and-array/instruments>

[44] Akasofu, S. I. and J. R. Kan "Physics of Auroral Arc Formation" Geophys. J. Int. **25,** (1981).

[45] Jacobs, J. A. *Geomagnetic Micropulsations*. Berlin: Springer-Verlag, 1970.

[46] Szuberla, Curt A. L. *An Investigation of Cusp Latitude Magnetosphere-ionosphere Physics: A Time Series Analysis Approach*. Diss. University of Alaska Fairbanks, 1997.

[47] Olson, John V. "Pi2 Pulsations and Substorm Onsets: A Review." J. Geophys. Res. **104**, A8, (1999).

[48] Hampton, Donald. "PFASC Inquiry." Message to the author. Sept.-Oct. 2014. E-mail.

[49] Wilson, Charles R. Personal conversation. March 2011.

[50] Todhunter, I., and J. G. Leathem. *Spherical Trigonometry, for the Use of Colleges and Schools*. London: Macmillan, 1901. Print.

[51] MATLAB Release 2012b, The MathWorks, Inc., Natick, Massachusetts, United States.

[52] Jackson, John David. *Classical Electrodynamics*. New York: Wiley, 1962.

[53] Stenbaek-Nielsen, H.c., and T.j. Hallinan. "Pulsating Auroras: Evidence for Noncollisional Thermalization of Precipitating Electrons." J. Geophys. Res. **84**, A7, (1979).

[54] Maeda, Kaichi, and Tomiya Watanabe. "Pulsating Aurorae and Infrasonic Waves in the Polar Atmosphere." J. Atmos. Sci. **21**, 1, (1964).

[55] Brekke, A. "On the Relative Importance of Joule Heating and the Lorentz Force in Generating Atmospheric Gravity Waves and Infrasound Waves in the Auroral Electrojets." J. Atmos. Terr. Phys. **41**, 5, (1979).

[56] Google earth V 6.2.2.6613. (September 30, 2006). HAARP, Gakona, Alaska.
DigitalGlobe 2012. 10 November 2015. <http://www.earth.google.com>